

UNIVERSITÀ DEGLI STUDI DI PAVIA

FACULTY OF ENGINEERING

DEPARTMENT OF ELECTRICAL, COMPUTER

AND BIOMEDICAL ENGINEERING

MASTER DEGREE IN ELECTRICAL ENGINEERING

Synchronous Reluctance Motor Drive with Advanced Control

Comparative Study of PI, Predictive Model-Based Control, Model-Free Predictive Control and INDI Control

---

AUTHOR

Stefano Di Mattia

SUPERVISOR

Prof. Pericle Zanchetta

CO-SUPERVISOR

Filippo Gemma

Academic Year 2025/2026

Abstract

This thesis compares control strategies for synchronous reluctance motors (SynRMs), a machine technology of growing industrial relevance. Being free of rare-earth materials, SynRMs avoid the supply-chain constraints and the environmental and economic burden associated with rare-earth extraction, which is confined to a limited number of sites worldwide. These advantages, however, come at the cost of a more demanding control problem: the absence of permanent-magnet excitation, together with pronounced magnetic saturation and cross-coupling between the axes, makes the machine model strongly nonlinear and parameter-dependent over the operating range.

Against this background, the thesis examines the proportional-integral (PI) regulator, still the reference solution in industrial drives, alongside two strategies of current research interest: predictive control and incremental nonlinear dynamic inversion (INDI). The latter, originally developed for fixed-wing flight control, constitutes the main contribution of this work. Its incremental formulation relies on measured or estimated derivatives of the state rather than on a complete model of the plant, which limits the sensitivity to parameter mismatch that typically affects model-based schemes applied to SynRM drives. All strategies are formulated in the dq reference frame and first assessed in simulation under comparable operating conditions.

The experimental implementation of the PI and INDI controllers is then described in detail, from the discrete-time formulation to the tuning procedure adopted on the test bench, providing a direct comparison between the state of the art and the proposed approach. The measured responses confirm the advantages of INDI in terms of tuning effort and dynamic performance, consistently with the preliminary simulation study.

Contents

1 Introduction **1**

2 Permanent Magnet Synchronous Motor **4**

2.1 Motor Model 6

2.2 PMSM field weakening theory 11

3 Synchronous Reluctance Motor **13**

3.1 Motor Model SynRM 14

3.1.1 Magnetic Saturation and Cross-Saturation 22

3.2 SynRM field weakening theory 25

4 Control Strategies **28**

4.1 Common features 28

4.1.1 MTPA, FW and MTPV control 28

4.1.2 Speed ramp control 34

4.1.3 Speed PI controller 34

4.1.4 Space Vector modulation 37

4.2 PI Current Control 42

4.3 Model-Based predictive Control 44

4.4 Model-Free Predictive Control 47

4.5 INDI Control 59

5 Simulation **65**

5.1 PI model simulation 66

5.2 Model-Based simulation 76

5.3 Model-Free simulation 90

5.4 INDI simulation 98

6 Experimental **104**

6.1 Test setup 105

6.2 SynRM characteristics 108

6.3 PMSM characteristics 109

6.4 PI control test result 109
6.5 INDI control test result 116

7 Conclusions **121**

1 Introduction

In the current geopolitical context, characterised by growing instability in the supply of strategic raw materials [1] and by an increasingly intense global technological competition, the energy transition and the decarbonisation of industrial systems have placed the efficiency of electrical machines and power electronic converters at the centre of the debate [2]. Among electrical machines, synchronous reluctance motors (SynRM) represent a valid alternative to induction motors and permanent magnet synchronous motors, being able to achieve good performance without the use of rare earth elements in their construction. The European Commission, through the Directorate-General for Internal Market, Industry, Entrepreneurship and SMEs (DG GROW), periodically publishes the Study on the Critical Raw Materials, which lists the raw materials deemed critical for the European market and highlights the need to reduce strategic dependencies. According to this study, China is by far the main supplier of rare earth elements to the European Union. Europe imports 85% of its Neodymium (Nd) from China, one of the key elements used in the production of permanent magnet motors [1]. Referring to the Table 1, the rationale behind European Union Regulation 1252/2024, which aims to promote the development of new technologies that lower the use of the aforementioned critical materials, becomes evident. Annex II of the same regulation lists the materials considered critical by the European Union, including some of the materials used in the construction of permanent magnets. Synchronous reluctance motors meet the need to reduce risks related to the availability of critical materials and certainly offer competitive performance in terms of energy savings. This context stimulate the objective of the thesis: to establish which control strategy for synchronous reluctance motors is the most reliable and robust in industrial operation, and which delivers the best dynamic performance in tracking assigned torque and speed references. To attempt to provide a possible answer to these questions, four control strategies are presented: classic PI control, which represents the state of the art in today's industry; model-based predictive control; model-free predictive control; and INDI control, which represents the novelties in control strategies for electric drives.

Table 1: Major global supplier countries of Critical Raw Materials – EU 2023. Source: European Commission, DG GROW [1].

#	Material	St.	Supplier	Share
1	aluminium	E	Australia	28%
2	antimony	E	China	56%
3	arsenic	P	China	44%
4	baryte	E	China	32%
5	beryllium	E	USA	67%
6	bismuth	P	China	70%
7	boron	E	Turkiye	48%
8	cerium	P	China	85%
9	cobalt	E	DRC	63%
10	coking coal	E	China	53%
11	copper	E	Chile	28%
12	dysprosium	P	China	100%
13	erbium	P	China	100%
14	europium	P	China	100%
15	feldspar	E	Turkiye	32%
16	fluorspar	E	China	56%
17	gadolinium	P	China	100%
18	gallium	P	China	94%
19	germanium	P	China	83%
20	hafnium	P	France	49%
21	helium	P	USA	56%
22	holmium	P	China	100%
23	iridium	P	S. Africa	93%
24	lanthanum	P	China	85%
25	lithium	P	China	56%
26	lutetium	P	China	100%
27	magnesium	P	China	91%
28	manganese	E	S. Africa	29%
29	natural graphite	E	China	67%
30	neodymium	P	China	85%
31	niobium	P	Brazil	92%
32	nickel	P	China	33%
33	palladium	P	Russia	40%
34	phosphate rock	E	China	48%
35	phosphorus	P	China	79%
36	platinum	P	S. Africa	71%
37	praseodymium	P	China	85%
38	rhodium	P	S. Africa	81%
39	ruthenium	P	S. Africa	94%
40	samarium	P	China	85%
41	scandium	P	China	67%
42	silicon metal	P	China	76%
43	strontium	E	Iran	37%
44	tantalum	E	DRC	35%
45	terbium	P	China	100%
46	thulium	P	China	100%
47	titanium metal	P	China	43%
48	tungsten	P	China	86%
49	vanadium	E	China	62%
50	ytterbium	P	China	100%
51	yttrium	P	China	100%
Grouped materials				
	HREEs	P	China	100%
	LREEs	P	China	85%
	PGMs[§]	P	S. Africa	75%
	PGMs (Pd)	P	Russia	40%

Legend: E = Extraction stage; P = Processing stage.

HREEs: Dysprosium, erbium, europium, gadolinium, holmium, lutetium, terbium, thulium, ytterbium, yttrium.

LREEs: Cerium, lanthanum, neodymium, praseodymium, samarium.

PGMs: Iridium, palladium, platinum, rhodium, ruthenium.

Comparing the different strategies required breaking the work down into three successive phases. In the first phase, a study of the proposed control strategies was conducted by reviewing previous publications on electrical drives, power electronics, and advanced electrical drives. This study provided the mathematical foundations, design parameters, and potential critical issues for each of the presented models. In the second phase, the models were implemented and simulated in a Matlab, Simulink environment using a synchronous reluctance motor model with flux mapping and complete inductances experimentally derived from previous studies conducted at the University of Nottingham. The simulations were compared under nominal speed conditions and under field weakening with variable load.

In the experimental phase, a state of art PI control and a INDI techniques will be tested.

The following thesis is organized as follows.

Chapter 2 presents PMSM motors, laying the foundation for understanding synchronous reluctance motors. Furthermore, the choice to present this type of motor is linked to the fact that in the experimental phase, a motor of this type was used to simulate a variable load, imposing a speed reference equal to zero and varying the torque limits.

Chapter 3 instead presents the synchronous reluctance motor under examination.

Chapter 4 presents the control strategies of PI (proportional-integral control), MB-PC (model-based predictive control), MF-PC (model-free predictive control) with ultra-local strategy and RLS (recursive least square) parameter search, and finally INDI (incremental non-linear dynamic inversion) control.

The chapter 5 shows the implementation steps in the Matlab/Simulink environment, and the related simulation results for all four controls. Chapter 6 presents the final experimental section, which shows the setup, implementation, and experimental results.

The final results and conclusions are reported in chapter 7, which attempts to answer the questions posed at the beginning of the thesis.

2 Permanent Magnet Synchronous Motor

The discussion of some concepts related to the SPM (Surface Permanent Magnet) motor is justified for two reasons. First, this type of machine will be recalled in the experimental chapter of the thesis, which is part of the simulation bench, and specifically, it will be used as a prime mover, while the SynRM motor will ack as a brake, Exploring its working area. Second, the development of PI control, the first of the four control strategies implemented and compared in this work, originated precisely from the permanent magnet motor, before being subsequently extended and adapted to the synchronous reluctance motor (SynRM), the main focus of this thesis.

Synchronous motors are able to deliver torque only at the synchronous speed (linked to the supply frequency). Thanks to power electronics and sensors, it is possible to vary the supply frequency and consequently the speed [3, 4]:

$$\omega_m = \frac{\omega_{el}}{pp} \text{ with } \omega_{el} = 2\pi f,$$

Where pp is the pole pairs of the motor. From a construction point of view, sinusoidal-powered synchronous motors can be divided into two families based on the arrangement of the permanent magnets in the rotor [5, 6]. The magnetic behaviour of the rotor is described by the inductances seen along two orthogonal directions of the rotor reference frame: the direct axis d, aligned with the direction of highest permeance, and the quadrature axis q, displaced by ninety electrical degrees from it. The corresponding inductances L_d and L_q relate the flux linkages to the currents flowing along the two axes [4, 7],

$$\psi_d = L_d\, i_d, \qquad \psi_q = L_q\, i_q,$$

and their ratio quantifies the magnetic anisotropy of the rotor. When the two values are the same the rotor is magnetically isotropic, and the reluctance seen by the stator field does not depend on the rotor position; when they differ, the rotor tends to align with the stator field, and this tendency produces a torque contribution of its own.

In surface-mounted permanent magnet motors (SPM), the magnets are glued or wrapped to the external surface of the rotor, with the magnets facing directly into the air gap.

This solution is constructively simple and guarantees a magnetically uniform air gap.
The permeability of the magnets is close to that of air, therefore the machine is substantially isotropic [6, 8]

$$L_d \approx L_q$$

The torque produced is exclusively magnetic and proportional to i_q, with an optimal control strategy at $i_d = 0$ [7, 5].
In internal magnet motors (interior permanent magnet IPM), the magnets are inserted inside the rotor core in seats made in the laminations. This configuration introduces a significant magnetic anisotropy [9]

$$L_d \neq L_q \text{ with } L_d < L_q$$

which adds an additional torque contribution according to the equation shown in the chapter 3.

$$C_m = \frac{3}{2} p_p \left[\psi_{pm} i_q + (L_d - L_q) i_d i_q \right] \tag{1}$$

To exploit both contributions, it is necessary to inject a contribution of $i_d < 0$ by identifying the optimal point on the torque curve while minimizing the absorbed current [9, 10].
Thanks to their construction features, IPM motors offer greater robustness as the magnets are immersed in the core, while SPM motors have the magnets glued or bandaged to the surface [9, 8].
Below, an SPM motor will be used to apply a resistive torque to the SynRM motor under test.
However, typical applications for these motors are in axis motion and robotics, where frequent starts, stops, and reverse motion require a fast response that is sufficiently high-performance even under variable load conditions. These motors are more expensive than traditional induction motors, but they have nevertheless found widespread use in CNC machine tools, industrial automation, robotics, and light traction applications [5, 3].
As mentioned, brushless motors use permanent magnets installed surface-mounted or immersed in the rotor, which inevitably increases costs.

The main advantages of this type of motor include: smaller size for the same torque compared to traditional induction motors high dynamic performance. Losses due to the Joule effect are limited to the stator winding, while hysteresis and eddy current losses can occur both in the stator body and in the rotor, in addition to mechanical losses due to friction and ventilation [8]. The efficiency of this type of machine remains very high. The main disadvantage, however, is the essential use of power electronics and associated sensors [3].

2.1 Motor Model

The stator voltage equations in the three-phase reference system *abc* are [4, 5]:

$$V_a = R_s i_a + \frac{d\psi_a}{dt} \tag{2}$$

$$V_b = R_s i_b + \frac{d\psi_b}{dt} \tag{3}$$

$$V_c = R_s i_c + \frac{d\psi_c}{dt} \tag{4}$$

$$J\frac{d\omega_m}{dt} = C_m - C_r \tag{5}$$

Where J is the moment of inertia, C_m the driving torque and C_r the resisting torque [11]. The linked fluxes of each phase include both the contribution of the stator currents through the self and mutual inductances, and the flux produced by the permanent magnets [7, 4]:

$$\psi_a = L_a(\theta)i_a + M_{ab}(\theta)i_b + M_{ac}(\theta)i_c + \psi_{pm,a}(\theta) \tag{6}$$

$$\psi_b = L_b(\theta)i_b + M_{ba}(\theta)i_a + M_{bc}(\theta)i_c + \psi_{pm,b}(\theta) \tag{7}$$

$$\psi_c = L_c(\theta)i_c + M_{ca}(\theta)i_a + M_{cb}(\theta)i_b + \psi_{pm,c}(\theta) \tag{8}$$

Where $\psi_{pm,a}(\theta)$, $\psi_{pm,b}(\theta)$, $\psi_{pm,c}(\theta)$ are the flux linkages due to the rotor permanent magnets on each stator phase, periodic functions of the rotor position θ. The stator equa-

tions can then be rewritten in compact form:

$$[V_s] = [R_s][I_s] + \frac{d}{dt}[M(\theta)][I_s] + \frac{d}{dt}[\Psi_{pm}(\theta)] \tag{9}$$

Developing the time derivatives and applying the rule $\frac{d}{dt} = \omega\frac{d}{d\theta}$, we obtain for phase a:

$$\begin{aligned} V_a = R_s i_a + \omega\frac{dL_a(\theta)}{d\theta}i_a + \omega\frac{dM_{ab}(\theta)}{d\theta}i_b + \omega\frac{dM_{ac}(\theta)}{d\theta}i_c \\ + L_a(\theta)\frac{di_a}{dt} + M_{ab}(\theta)\frac{di_b}{dt} + M_{ac}(\theta)\frac{di_c}{dt} + \omega\frac{d\psi_{pm,a}(\theta)}{d\theta} \end{aligned} \tag{10}$$

with $\omega_m = \omega/p_p$ mechanical speed of the rotor. The last term $\omega\frac{d\psi_{pm,a}}{d\theta}$ represents the back-EMF induced by the rotating permanent magnet flux on phase a [5]. The stator equations can be written in compact matrix form as:

$$[V_s] = [R_s][I_s] + \omega\frac{d[L(\theta)]}{d\theta}[I_s] + [L(\theta)]\frac{d[I_s]}{dt} + \omega\frac{d[\Psi_{pm}(\theta)]}{d\theta} \tag{11}$$

By multiplying scalarly by $[I_s]^T$ we obtain the power balance:

$$[I_s]^T[V_s] = [I_s]^T[R_s][I_s] + \omega[I_s]^T\frac{d[L(\theta)]}{d\theta}[I_s] + [I_s]^T[L(\theta)]\frac{d[I_s]}{dt} + \omega[I_s]^T\frac{d[\Psi_{pm}(\theta)]}{d\theta} \tag{12}$$

Defining the magnetic energy stored in the system as [12]:

$$E_m = \frac{1}{2}[I_s]^T[L(\theta)][I_s] \tag{13}$$

and computing its time derivative:

$$\frac{d}{dt}E_m = \frac{d}{dt}[I_s]^T[L(\theta)][I_s] + \frac{1}{2}[I_s]^T\frac{d[L(\theta)]}{dt}[I_s] \tag{14}$$

The mechanical power developed by the machine is:

$$P_m = \frac{\omega}{2}[I_s]^T\frac{d[L(\theta)]}{d\theta}[I_s] + \omega[I_s]^T\frac{d[\Psi_{pm}(\theta)]}{d\theta} \tag{15}$$

and the electromagnetic torque in the *abc* system [12, 4]:

$$C_m = \frac{p_p}{2}[I_s]^T \frac{d[L(\theta)]}{d\theta}[I_s] + p_p[I_s]^T \frac{d[\Psi_{pm}(\theta)]}{d\theta} \tag{16}$$

The torque now has two contributions: a *reluctance term* dependent on the inductance variation with rotor position, and a *magnetic term* due to the interaction between stator currents and the permanent magnet flux linkage. In surface-mounted PMSM (SPM), the rotor is magnetically isotropic ($L_d \approx L_q$), so the reluctance term vanishes and only the magnetic term contributes to torque. In interior PMSM (IPM), both terms are present [9]. To simplify the analysis, we apply the Park transformation $[T(\theta)]$ [13, 4] which transfers

the quantities to the rotating reference frame attached to the rotor. The inductance matrix in the *abc* system, periodic in θ, becomes constant in the $dq0$ system, and the permanent magnet flux linkage vector becomes constant:

$$[\Psi_{pm,dq0}] = [T(\theta)][\Psi_{pm,abc}(\theta)] = \begin{bmatrix} \psi_{pm} \\ 0 \\ 0 \end{bmatrix} \tag{17}$$

where ψ_{pm} is the total flux linkage amplitude produced by the permanent magnets, aligned with the d-axis by definition of the Park reference frame [7]. With L_{abc} equal to [4, 14]:

$$\begin{bmatrix} L_0 + L_1 - L_2\cos(2\theta) & -\frac{L_1}{2} - L_2\cos\left(2\theta - \frac{2\pi}{3}\right) & -\frac{L_1}{2} - L_2\cos\left(2\theta - \frac{4\pi}{3}\right) \\ -\frac{L_1}{2} - L_2\cos\left(2\theta - \frac{2\pi}{3}\right) & L_0 + L_1 - L_2\cos\left(2\theta - \frac{4\pi}{3}\right) & -\frac{L_1}{2} - L_2\cos(2\theta) \\ -\frac{L_1}{2} - L_2\cos\left(2\theta - \frac{4\pi}{3}\right) & -\frac{L_1}{2} - L_2\cos(2\theta) & L_0 + L_1 - L_2\cos\left(2\theta + \frac{4\pi}{3}\right) \end{bmatrix} \tag{18}$$

and the Park transformation matrix $[T(\theta)]$:

$$[T(\theta)] = \begin{bmatrix} \cos(\theta) & \cos\left(\theta - \frac{2\pi}{3}\right) & \cos\left(\theta + \frac{2\pi}{3}\right) \\ -\sin(\theta) & -\sin\left(\theta - \frac{2\pi}{3}\right) & -\sin\left(\theta + \frac{2\pi}{3}\right) \\ \frac{1}{2} & \frac{1}{2} & \frac{1}{2} \end{bmatrix} \tag{19}$$

Applying the transformation to the full stator voltage equations and multiplying by $[T(\theta)]$:

$$\begin{aligned} [V_{dq0}] = [R_s][i_{dq0}] + [L_{dq0}]\frac{d}{dt}[i_{dq0}] \\ + \omega \begin{bmatrix} 0 & -1 & 0 \\ 1 & 0 & 0 \\ 0 & 0 & 0 \end{bmatrix} [L_{dq0}][i_{dq0}] + \omega \begin{bmatrix} 0 & -1 & 0 \\ 1 & 0 & 0 \\ 0 & 0 & 0 \end{bmatrix} [\Psi_{pm,dq0}] \end{aligned} \tag{20}$$

The stator voltage equations in the dq system take the form [7, 5]:

$$v_d = R_s i_d + L_d \frac{di_d}{dt} - \omega L_q i_q \tag{21}$$

$$v_q = R_s i_q + L_q \frac{di_q}{dt} + \omega L_d i_d + \omega \psi_{pm} \tag{22}$$

where the terms $\omega L_q i_q$ and $\omega L_d i_d$ represent the inductive decoupling voltages between the d and q axes, and $\omega \psi_{pm}$ is the back-EMF term generated by the permanent magnet flux rotating with the rotor. Multiplying the d-axis voltage equation by i_d and the q-axis equation by i_q:

$$v_d i_d = R_s i_d^2 + L_d i_d \frac{di_d}{dt} - \omega L_q i_q i_d \tag{23}$$

$$v_q i_q = R_s i_q^2 + L_q i_q \frac{di_q}{dt} + \omega L_d i_d i_q + \omega \psi_{pm} i_q \tag{24}$$

Summing the two contributions, the instantaneous power balance in the dq frame is:

$$v_d i_d + v_q i_q = R_s(i_d^2 + i_q^2) + L_d i_d \frac{di_d}{dt} + L_q i_q \frac{di_q}{dt} + \omega(L_d - L_q) i_d i_q + \omega \psi_{pm} i_q \tag{25}$$

where the first term represents Joule losses, the second and third the magnetic energy variation, and the last two terms the mechanical power $P_m = \omega C_m / p_p$. The magnetic energy stored in the dq system is:

$$E_m = \frac{1}{2}(L_d i_d^2 + L_q i_q^2) + \psi_{pm} i_d \tag{26}$$

Computing its time derivative and assuming constant inductances:

$$\frac{d}{dt}E_m = L_d i_d \frac{di_d}{dt} + L_q i_q \frac{di_q}{dt} + \psi_{pm} \frac{di_d}{dt} \tag{27}$$

The term $\psi_{pm} \frac{di_d}{dt}$ belongs to the reactive magnetic energy variation and does not contribute to mechanical power production. Isolating the mechanical power term and dividing by ω, the electromagnetic torque in the dq reference frame is [7, 9]:

$$C_m = \frac{3}{2} p_p \left[\psi_{pm} i_q + (L_d - L_q) i_d i_q \right] \tag{28}$$

The factor $\frac{3}{2}$ arises from the amplitude conservation convention of the Park transformation [4, 14].

The total electromagnetic torque of the PMSM consists of two distinct contributions:

- Magnetic torque: produced by the interaction between the stator q-axis current and the permanent magnet flux linkage. This term is always present and is the dominant contribution in SPM machines.
- Reluctance torque: produced by the magnetic anisotropy of the rotor. This term is significant only in IPM machines where $L_d \neq L_q$.

In the particular case of a Surface-mounted PMSM (SPM), the rotor is magnetically isotropic ($L_d = L_q$), the reluctance term vanishes, and the torque simplifies to:

$$C_m^{SPM} = \frac{3}{2} p_p \psi_{pm} i_q \tag{29}$$

confirming that in SPM machines, torque is controlled exclusively through the q-axis current i_q, and the optimal control strategy sets $i_d = 0$ [7].

2.2 PMSM field weakening theory

An inverter powered permanent magnet motor has two physical limits that must be respected to avoid possible malfunctions. The first is the current constraint imposed by the thermal capacity of the stator windings. The second constraint is the voltage constraint, limited by the inverter power supply and its modulation strategy [10, 5]. Recalling the voltage equations in the dq reference frame:

$$v_d = R_s i_d + L_d \frac{di_d}{dt} - \omega L_q i_q$$
$$v_q = R_s i_q + L_q \frac{di_q}{dt} + \omega L_d i_d + \omega \psi_{pm}$$

and the torque:

$$C_m = \frac{3}{2} p_p \, \psi_{pm} \, i_q$$

The equations can be simplified by considering the machine operating at constant speed.

$$\frac{di_d}{dt} = 0$$
$$\frac{di_q}{dt} = 0$$

At high speeds, the resistive term is negligible, and the voltage equations are further simplified [10].

$$v_d \approx -\omega L_q i_q \tag{30}$$

$$v_q \approx \omega L_d i_d + \omega \psi_{pm} \tag{31}$$

Applying the maximum voltage that the converter can generate:

$$v_d^2 + v_q^2 \approx \omega^2 \left(L_q i_q\right)^2 + \omega^2 \left(L_d i_d + \psi_m\right)^2 \tag{32}$$

We obtain the final circumference and dividing by ω^2

$$(L_s i_q)^2 + (L_s i_d + \psi_m)^2 \leq \frac{V_{max}^2}{\omega^2} \tag{33}$$

with:

$$\psi_m = L_f i_f \tag{34}$$

where L_f is the (fictitious) excitation inductance and i_f is the equivalent characteristic current, constant in an already magnetized PM. These are not real control variables, but equivalent parameters.As mentioned previously we are faced with a limit circumference, precisely because $L_d = L_q = L_f$. The centre of this circle is located at $(-i_f = -\frac{\psi_m}{L_f}, 0)$ and radius $\frac{V_{max}}{L_s}$. The current vector I_s must always lie within the circumference of voltage corresponding to a given required electrical velocity [10, 9]. Unlike the voltage constraint, the current constraint is purely thermal, in fact it is a rating plate limit on the stator windings and independent of the rotation speed [5]:

$$i_d^2 + i_q^2 \leq I_{max}^2 \tag{35}$$



Figure 1: dq plane voltage and current circumferences

3 Synchronous Reluctance Motor

In recent years, research has focused on developing motors that minimize the use of rare earths to reduce environmental impact [1, 2]. Synchronous reluctance motors (SynRM) are an alternative that can meet this requirement. SynRM motors, unlike permanent magnet motors, do not use magnets (rare earths), thus avoiding the issues related to the supply of these materials, such as their availability and the environmental impact of their extraction [1]. The torque these motors can deliver is related to the variation in stored magnetic energy as a function of the relative positions of the rotor and stator [4]. Constructively, the stator resembles that of a common rotating asynchronous machine, while the rotor has an anisotropic structure without permanent magnets. The rotor's saliency is achieved by flux barriers, consisting of holes and shapes in the rotor designed to direct the flux appropriately [2]. For this reason, the machine is also known as a singly salient

reluctance motor.

It is a synchronous machine because the rotor moves in synchronism with the magnetic field generated by the stator windings. As we will see in the demonstrations below, the aim of the design is to maximize the ratio between the fictitious inductance on the direct axis and the quadrature axis.

$$\frac{L_d}{L_q} \simeq 10 \div 20$$
$$\text{with: } L_d >> L_q > 0$$

It is precisely this ratio that determines the torque production of the machine [2]. The main advantages include higher efficiency than induction motors, the absence of permanent magnets, and simple construction [2]. In terms of application, they are used to replace asynchronous motors in the low-to-medium power range with speeds not exceeding 3000 rpm [2].

3.1 Motor Model SynRM

The machine model is first derived in the three-phase *abc* reference frame, fixed to the stator, and then transferred to the dq reference frame, rotating with the rotor. It is assumed that the stator windings are symmetrical and sinusoidally distributed, that the magnetic circuit is linear, and that the star point is isolated, so that the zero-sequence component of the currents is zero [4, 15].

The voltage applied to the terminals of each phase balances the resistive drop and the time variation of the flux linked with that phase [4]:

$$V_a = R_s i_a + \frac{d\psi_a}{dt} \tag{36}$$

$$V_b = R_s i_b + \frac{d\psi_b}{dt} \tag{37}$$

$$V_c = R_s i_c + \frac{d\psi_c}{dt} \tag{38}$$

where V_a, V_b, V_c are the phase voltages, i_a, i_b, i_c the phase currents, ψ_a, ψ_b, ψ_c the flux linkages of the three phases, and R_s is the stator phase resistance, assumed to be equal for the three phases.

The electrical model is completed by the mechanical equation, which relates the rotor acceleration to the imbalance between the torque produced by the machine and the torque opposed by the load [11]:

$$J\frac{d\omega_m}{dt} = C_m - C_r \tag{39}$$

where J is the total moment of inertia of the rotating masses, C_m is the electromagnetic torque, and C_r is the load torque. The mechanical speed ω_m is related to the electrical angular frequency ω by $\omega_m = \omega/p_p$, where p_p is the number of pole pairs. The electrical rotor position is denoted by θ, so that $d\theta/dt = \omega$.

In the absence of permanent magnets and rotor windings, the flux linkage of each phase is produced exclusively by the three stator currents, through the self- and mutual inductances. These inductances depend on the rotor position θ, because the reluctance of the magnetic path seen by each phase changes as the rotor moves [15, 4]:

$$\psi_a = L_a(\theta)\, i_a + M_{ab}(\theta)\, i_b + M_{ac}(\theta)\, i_c \tag{40}$$

$$\psi_b = M_{ba}(\theta)\, i_a + L_b(\theta)\, i_b + M_{bc}(\theta)\, i_c \tag{41}$$

$$\psi_c = M_{ca}(\theta)\, i_a + M_{cb}(\theta)\, i_b + L_c(\theta)\, i_c \tag{42}$$

where L_a, L_b and L_c are the self-inductances of the three phases and M_{jk} is the mutual inductance between phases j and k, with $M_{jk} = M_{kj}$ by the reciprocity principle [12].

By collecting the phase quantities in the column vectors $[V_s]$, $[I_s]$ and $[\Psi]$, and the inductances in the symmetric matrix $[L(\theta)]$, the three stator equations can be written in compact form. Applying the product rule, the contribution due to the variation of the inductances is separated from the one due to the variation of the currents:

$$\begin{aligned}[V_s] &= [R_s][I_s] + \frac{d[\Psi]}{dt} = [R_s][I_s] + \frac{d}{dt}\Big([L(\theta)][I_s]\Big) \\ &= [R_s][I_s] + \frac{d[L(\theta)]}{dt}[I_s] + [L(\theta)]\frac{d[I_s]}{dt}\end{aligned} \tag{43}$$

Writing out phase a explicitly, the two groups of terms are immediately recog-

nisable: the first three terms after the resistive drop derive from the variation of the inductances, the last three from the variation of the currents.

$$\begin{aligned} V_a = R_s i_a + \frac{dL_a(\theta)}{dt} i_a + \frac{dM_{ab}(\theta)}{dt} i_b + \frac{dM_{ac}(\theta)}{dt} i_c \\ + L_a(\theta)\frac{di_a}{dt} + M_{ab}(\theta)\frac{di_b}{dt} + M_{ac}(\theta)\frac{di_c}{dt} \end{aligned} \tag{44}$$

Since the inductances depend on time only through the rotor position, the chain rule $\frac{d}{dt} = \omega\frac{d}{d\theta}$ can be applied, which gives for phase a:

$$\begin{aligned} V_a = R_s i_a + \omega\frac{dL_a(\theta)}{d\theta} i_a + \omega\frac{dM_{ab}(\theta)}{d\theta} i_b + \omega\frac{dM_{ac}(\theta)}{d\theta} i_c \\ + L_a(\theta)\frac{di_a}{dt} + M_{ab}(\theta)\frac{di_b}{dt} + M_{ac}(\theta)\frac{di_c}{dt} \end{aligned} \tag{45}$$

Unlike in a permanent magnet machine, none of the terms is independent of the currents: there is no back-EMF, and the only mechanism available for torque production is the variation of the inductances with the rotor position. The machine is therefore purely anisotropic.

Extending the same considerations to the three phases leads to the compact matrix form

$$[V_s] = [R_s][I_s] + \omega\frac{d[L(\theta)]}{d\theta}[I_s] + [L(\theta)]\frac{d[I_s]}{dt} \tag{46}$$

in which $[L(\theta)]$ is the matrix of self- and mutual inductances introduced above.

The torque is identified through the energy balance [12]. Multiplying the compact stator equation by $[I_s]^T$ gives the instantaneous power absorbed at the stator terminals:

$$[I_s]^T[V_s] = [I_s]^T[R_s][I_s] + \omega[I_s]^T\frac{d[L(\theta)]}{d\theta}[I_s] + [I_s]^T[L(\theta)]\frac{d[I_s]}{dt} \tag{47}$$

The first term represents the Joule losses in the windings, while the remaining two contain both the variation of the energy stored in the magnetic field and the power converted into mechanical form. To separate them, the magnetic energy stored in the

system is defined explicitly,

$$E_m = \frac{1}{2}[I_s]^T [L(\theta)][I_s] \tag{48}$$

and its time derivative is computed, so that the mechanical power P_m can be isolated by difference [12, 4]:

$$\frac{d}{dt}E_m = \frac{1}{2}\left(\frac{d[I_s]^T}{dt}[L(\theta)][I_s] + [I_s]^T\frac{d[L(\theta)]}{dt}[I_s] + [I_s]^T[L(\theta)]\frac{d[I_s]}{dt}\right) \tag{49}$$

$$= [I_s]^T[L(\theta)]\frac{d[I_s]}{dt} + \frac{\omega}{2}[I_s]^T\frac{d[L(\theta)]}{d\theta}[I_s] \tag{50}$$

where the first and third terms have been combined by exploiting the symmetry of $[L(\theta)]$, and the chain rule has been applied to the second.

Subtracting the Joule losses and the variation of magnetic energy from the power balance, the remaining mechanical power developed by the motor is:

$$P_m = \frac{\omega}{2}[I_s]^T\frac{d[L(\theta)]}{d\theta}[I_s] \tag{51}$$

Recalling that $P_m = C_m\omega_m = C_m\omega/p_p$, the electromagnetic torque in the *abc* frame is obtained [12, 15]:

$$C_m = \frac{p_p}{2}[I_s]^T\frac{d[L(\theta)]}{d\theta}[I_s] \tag{52}$$

The torque depends exclusively on the variation of the inductances with the rotor position, which confirms the purely anisotropic nature of the synchronous reluctance machine: if the rotor were isotropic, the matrix $[L]$ would be constant, its derivative would be zero, and no torque could be produced [16].

The resulting model is correct, but unsuitable for control design because its coefficients vary with the rotor position. To remove this dependency, the Park transformation $[T(\theta)]$ [13, 4] is applied, which transfers the stator quantities to a reference frame rotating with the rotor, with the d axis aligned with the direction of maximum permeance and the q axis in quadrature. Under this transformation, the inductance matrix, periodic in θ in

the *abc* frame, becomes constant and diagonal in the $dq0$ frame:

$$[L_{dq0}] = [T(\theta)]\,[L_{abc}]\,[T(\theta)]^{-1} = \begin{bmatrix} L_d & 0 & 0 \\ 0 & L_q & 0 \\ 0 & 0 & L_0 \end{bmatrix} \tag{53}$$

The matrix $[L_{abc}]$ contains a constant part and a part oscillating at twice the electrical position, since the magnetic circuit repeats itself every half electrical revolution [4, 14]:

$$[L_{abc}] = \begin{bmatrix} L_0 + L_1 + L_2\cos(2\theta) & -\frac{L_1}{2} + L_2\cos\left(2\theta - \frac{2}{3}\pi\right) & -\frac{L_1}{2} + L_2\cos\left(2\theta - \frac{4}{3}\pi\right) \\ -\frac{L_1}{2} + L_2\cos\left(2\theta - \frac{2}{3}\pi\right) & L_0 + L_1 + L_2\cos\left(2\theta - \frac{4}{3}\pi\right) & -\frac{L_1}{2} + L_2\cos(2\theta) \\ -\frac{L_1}{2} + L_2\cos\left(2\theta - \frac{4}{3}\pi\right) & -\frac{L_1}{2} + L_2\cos(2\theta) & L_0 + L_1 + L_2\cos\left(2\theta + \frac{4}{3}\pi\right) \end{bmatrix} \tag{54}$$

where L_0 is the leakage inductance of a phase, which does not cross the air gap and is therefore independent of position, L_1 is the average value of the magnetising inductance, and $L_2 > 0$ is the amplitude of its variation with position, a direct measure of the rotor anisotropy. With this sign convention the self-inductance of phase a is maximum when the d axis is aligned with the phase axis ($\theta = 0$), and the transformation yields

$$L_d = L_0 + \frac{3}{2}(L_1 + L_2), \qquad L_q = L_0 + \frac{3}{2}(L_1 - L_2) \tag{55}$$

so that $L_d - L_q = 3L_2$: the anisotropy of the dq model coincides with the position-dependent part of the *abc* inductances. The transformation matrix, in the amplitude-invariant form adopted throughout this work, is

$$[T(\theta)] = \frac{2}{3}\begin{bmatrix} \cos(\theta) & \cos\left(\theta - \frac{2\pi}{3}\right) & \cos\left(\theta + \frac{2\pi}{3}\right) \\ -\sin(\theta) & -\sin\left(\theta - \frac{2\pi}{3}\right) & -\sin\left(\theta + \frac{2\pi}{3}\right) \\ \frac{1}{2} & \frac{1}{2} & \frac{1}{2} \end{bmatrix} \tag{56}$$

whose first two rows project the phase quantities onto the d and q axes, while the

third extracts the zero-sequence component. The factor $2/3$ makes the amplitude of the dq quantities equal to the peak value of the corresponding phase quantities.

The transformation is now applied to the stator equations. Written in terms of flux linkages, they read

$$[V_{abc}] = [R_s][I_{abc}] + \frac{d}{dt}\Big([L_{abc}(\theta)][I_{abc}]\Big) \tag{57}$$

The phase quantities are expressed as functions of the $dq0$ components, $[V_{abc}] = [T(\theta)]^{-1}[V_{dq0}]$ and $[I_{abc}] = [T(\theta)]^{-1}[i_{dq0}]$. From Eq. (53),
$[L_{abc}] = [T(\theta)]^{-1}[L_{dq0}][T(\theta)]$, so the flux linkages become
$[L_{abc}][I_{abc}] = [T(\theta)]^{-1}[L_{dq0}][i_{dq0}]$.
Substituting, and applying the product rule to the derivative of $[T(\theta)]^{-1}$:

$$[T(\theta)]^{-1}[V_{dq0}] = [R_s][T(\theta)]^{-1}[i_{dq0}] + [T(\theta)]^{-1}[L_{dq0}]\frac{d}{dt}[i_{dq0}] + \omega\frac{d[T(\theta)]^{-1}}{d\theta}[L_{dq0}][i_{dq0}] \tag{58}$$

where the inductances in $[L_{dq0}]$ are constant, so that only the currents and the transformation matrix depend on time. Multiplying on the left by $[T(\theta)]$ to bring all quantities into the rotating frame:

$$[V_{dq0}] = [T(\theta)][R_s][T(\theta)]^{-1}[i_{dq0}] + [L_{dq0}]\frac{d}{dt}[i_{dq0}] + \omega\,[T(\theta)]\frac{d[T(\theta)]^{-1}}{d\theta}[L_{dq0}][i_{dq0}] \tag{59}$$

The resistance matrix, being a multiple of the identity, is unchanged by the transformation, and the product $[T(\theta)]\,d[T(\theta)]^{-1}/d\theta$ is a constant rotation matrix. The final form is therefore:

$$[V_{dq0}] = [R_s][i_{dq0}] + [L_{dq0}]\frac{d}{dt}[i_{dq0}] + \omega \begin{bmatrix} 0 & -1 & 0 \\ 1 & 0 & 0 \\ 0 & 0 & 0 \end{bmatrix} [L_{dq0}][i_{dq0}] \tag{60}$$

The last term does not derive from a physical variation of the flux, but from the time derivative of the transformation matrix, that is, from the fact that the reference frame is rotating: it collects the motional terms [14].

Since the star point is isolated, the zero-sequence component is zero, and the previous equation reduces to two scalar equations, which constitute the model actually used for control design [17, 15]:

$$v_d = R_s i_d + L_d \frac{di_d}{dt} - \omega L_q i_q \tag{61}$$

$$v_q = R_s i_q + L_q \frac{di_q}{dt} + \omega L_d i_d \tag{62}$$

where v_d and v_q are the stator voltages in the rotor reference frame, i_d and i_q are the corresponding currents, and L_d and L_q are the synchronous inductances of the direct and quadrature axes. The terms $\omega L_q i_q$ and $\omega L_d i_d$ are the cross-coupling voltages between the two axes: they make the two current loops interact and require the introduction of a decoupling network in the controller [17].

The torque calculation is now repeated in the rotating frame. Multiplying the d-axis equation by i_d and the q-axis equation by i_q:

$$v_d i_d = R_s i_d^2 + L_d i_d \frac{di_d}{dt} - \omega L_q i_q i_d \tag{63}$$

$$v_q i_q = R_s i_q^2 + L_q i_q \frac{di_q}{dt} + \omega L_d i_d i_q \tag{64}$$

With the amplitude-invariant transformation, the power in the dq frame is $\frac{3}{2}$ times the sum of the products $v_d i_d$ and $v_q i_q$, since $[T(\theta)]^{-T}[T(\theta)]^{-1} = \text{diag}\left(\frac{3}{2}, \frac{3}{2}, 3\right)$. Summing

the two equations, the instantaneous power balance in the dq frame is therefore:

$$\frac{3}{2}\left(v_d i_d + v_q i_q\right) = \frac{3}{2}\left[R_s(i_d^2 + i_q^2) + L_d i_d \frac{di_d}{dt} + L_q i_q \frac{di_q}{dt} + \omega(L_d - L_q) i_d i_q\right] \tag{65}$$

where the first term represents the Joule losses, the second and third the variation of magnetic energy, and the last the mechanical power $P_m = \omega C_m / p_p$. That the second and third terms coincide with the variation of stored energy is verified by writing the magnetic energy in the dq frame, which is consistent with Eq. (48),

$$E_m = \frac{3}{2} \cdot \frac{1}{2}\left(L_d i_d^2 + L_q i_q^2\right) \tag{66}$$

and differentiating it with respect to time under the hypothesis of constant inductances:

$$\frac{d}{dt} E_m = \frac{3}{2}\left(L_d i_d \frac{di_d}{dt} + L_q i_q \frac{di_q}{dt}\right) \tag{67}$$

Isolating the mechanical power term, $P_m = \frac{3}{2}\,\omega(L_d - L_q)\, i_d\, i_q$, and dividing by the mechanical speed $\omega_m = \omega / p_p$, the electromagnetic torque in the dq frame is obtained [15, 2]:

$$C_m = \frac{3}{2} p_p (L_d - L_q)\, i_d\, i_q \tag{68}$$

The factor $\frac{3}{2}$ therefore follows from the power relation of the amplitude-invariant Park transformation adopted in this work [4, 14]. The torque depends on the difference $(L_d - L_q)$, which expresses the magnetic anisotropy of the rotor, and requires both current components to be different from zero. Unlike the surface permanent magnet machine, for which the optimal strategy is $i_d = 0$, in the SynRM the current vector must be oriented at an angle that balances the two components [17, 16]. Since there are no permanent magnets, the SynRM produces torque exclusively through reluctance, which confirms its purely anisotropic nature [2].

3.1.1 Magnetic Saturation and Cross-Saturation

The SynRM under test has been characterised in previous work, in which its flux maps were identified experimentally [18]. A distinctive feature of the SynRM is the non-linear relationship between flux linkage and current, due to self-saturation and cross-saturation phenomena [19, 20]. Self-saturation indicates that the d- and q-axis currents saturate the flux linkage of their own axis, respectively. Cross-saturation, on the other hand, describes the effect by which a change of the current on one axis modifies the flux linkage of the other axis [19]. Consequently, the d- and q-axis flux linkages must be treated as non-linear functions of the current vector $[i_d, i_q]$ [20]:

$$\psi_d = \psi_d(i_d, i_q), \qquad \psi_q = \psi_q(i_d, i_q) \tag{69}$$

The flux maps are identified with the following procedure. A PMSM, operated in speed control, is mechanically coupled to the SynRM under test, which is operated in current control. By exploring a grid of operating points in the (i_d, i_q) plane, the d- and q-axis flux maps are reconstructed [20, 18]. The identification of these maps is not part of this thesis; they are used as the starting point for the design of the control system. The identified flux maps are shown in Fig. 2.

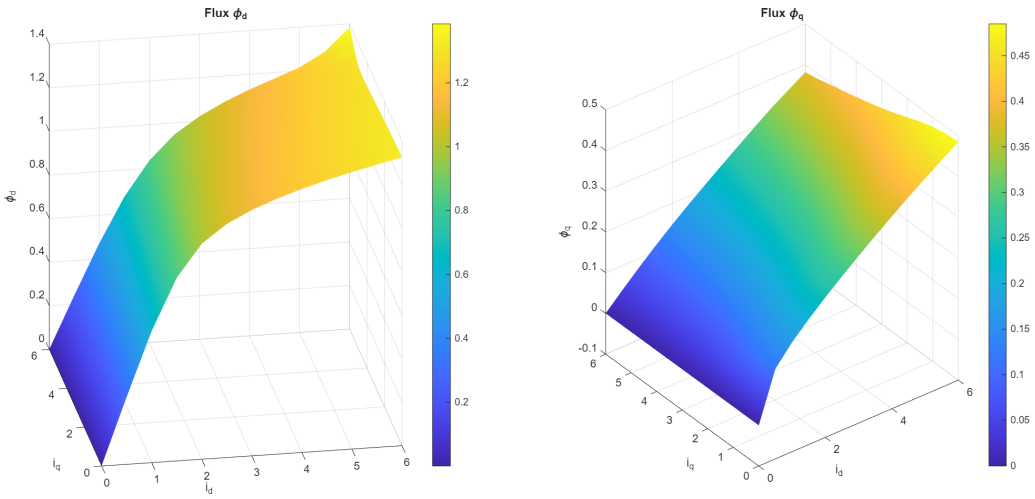


Figure 2: Identified d- and q-axis flux linkage maps.

The apparent inductances are defined as the ratio between the flux linkage and the current of the same axis, and provide an average description of the magnetic behaviour

at a given operating point [21]:

$$L_d(i_d, i_q) = \frac{\psi_d(i_d, i_q)}{i_d} \tag{70}$$

$$L_q(i_d, i_q) = \frac{\psi_q(i_d, i_q)}{i_q} \tag{71}$$

They are shown in Fig. 3.

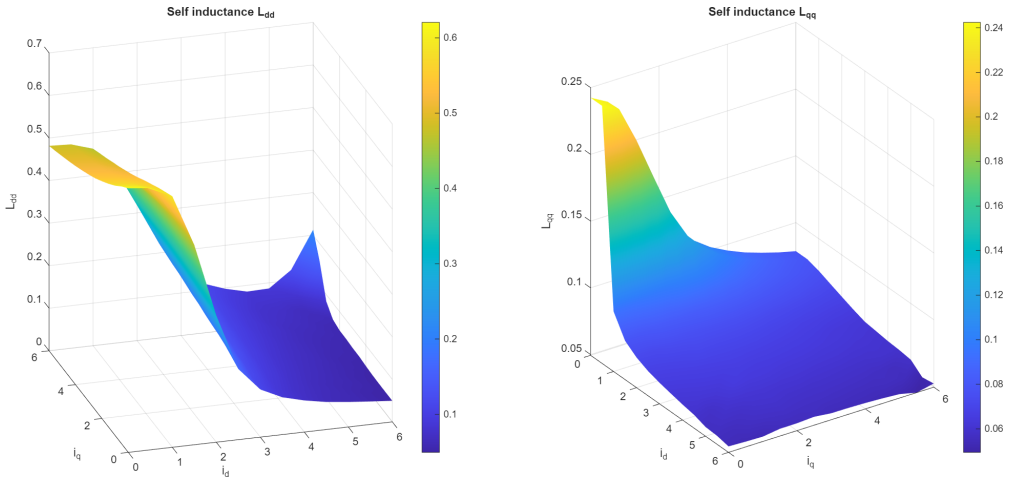


Figure 3: Apparent inductances L_d and L_q.

With saturation, the voltage equations of the SynRM must be written in terms of flux linkages [22]:

$$v_d = R_s i_d + \frac{d\psi_d}{dt} - \omega\psi_q \tag{72}$$

$$v_q = R_s i_q + \frac{d\psi_q}{dt} + \omega\psi_d \tag{73}$$

The motional terms $\omega\psi_q$ and $\omega\psi_d$ are described exactly by the apparent inductances, since $\psi_d = L_d i_d$ and $\psi_q = L_q i_q$ by definition. The flux derivatives, instead, must be expanded with the chain rule, because each flux depends on both currents:

$$\frac{d\psi_d}{dt} = \frac{\partial\psi_d}{\partial i_d}\frac{di_d}{dt} + \frac{\partial\psi_d}{\partial i_q}\frac{di_q}{dt} \tag{74}$$

$$\frac{d\psi_q}{dt} = \frac{\partial\psi_q}{\partial i_d}\frac{di_d}{dt} + \frac{\partial\psi_q}{\partial i_q}\frac{di_q}{dt} \tag{75}$$

For an accurate model, especially under dynamic conditions, it is therefore necessary to use the differential (incremental) inductances, defined as the partial derivatives of the flux linkages with respect to the currents [21, 19]:

$$L_{dd}^{inc} = \frac{\partial \psi_d}{\partial i_d} \qquad L_{dq}^{inc} = \frac{\partial \psi_d}{\partial i_q} \qquad L_{qd}^{inc} = \frac{\partial \psi_q}{\partial i_d} \qquad L_{qq}^{inc} = \frac{\partial \psi_q}{\partial i_q} \tag{76}$$

They form a matrix that describes both self-saturation (diagonal terms) and cross-saturation (off-diagonal terms):

$$\begin{bmatrix} \dot{\psi}_d \\ \dot{\psi}_q \end{bmatrix} = \begin{bmatrix} L_{dd}^{inc} & L_{dq}^{inc} \\ L_{qd}^{inc} & L_{qq}^{inc} \end{bmatrix} \begin{bmatrix} \dot{i}_d \\ \dot{i}_q \end{bmatrix} \tag{77}$$

The differential inductances computed from the identified maps are shown in Fig. 4. For an ideal, lossless magnetic circuit, energy conservation implies $L_{dq}^{inc} = L_{qd}^{inc}$; in maps obtained from measurements the two cross terms may differ, owing to measurement uncertainty and to effects not included in the lossless model, such as iron losses.

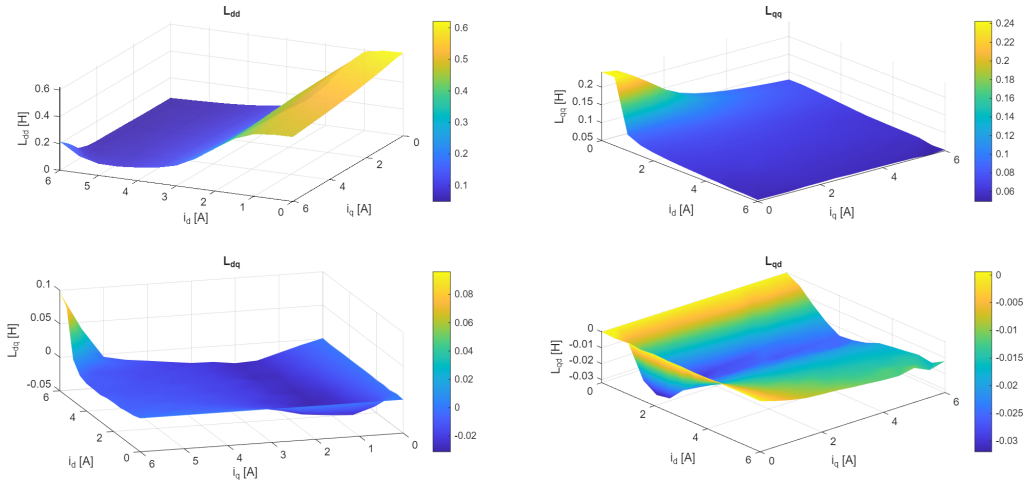


Figure 4: Differential inductances computed from the identified flux maps.

In short, the apparent inductances describe the steady-state relationship between flux and current, and therefore the motional terms and the torque; the differential inductances describe the transient behaviour, i.e. the response of the currents to a voltage variation.

3.2 SynRM field weakening theory

To extend the speed range of the SynRM, suitable control strategies must be adopted. These strategies must respect the voltage and current constraints, so as to ensure an acceptable control response over the entire extended operating range. This section discusses the machine limits and the preferred current trajectories [17, 10]. The numerical method used to compute them is presented in the next chapter, in Subsection 4.1.1, which describes the functions shared by all control strategies. The starting point is the set of electrical equations that govern the operation of the machine. The voltage equations (61) and (62) in the dq reference frame are recalled here for convenience:

$$v_d = R_s i_d + L_d \frac{di_d}{dt} - \omega L_q i_q$$
$$v_q = R_s i_q + L_q \frac{di_q}{dt} + \omega L_d i_d$$

together with the torque equation:

$$C_m = \frac{3}{2} p_p (L_d - L_q)\, i_d\, i_q$$

where i_d and i_q are the stator currents in the dq reference frame, L_d and L_q are the d- and q-axis inductances, R_s is the stator resistance, and ω is the electrical angular speed. When saturation is taken into account, L_d and L_q are the apparent inductances of (70)–(71), evaluated at the operating point: the torque expression remains valid in this form, since $C_m = \frac{3}{2} p_p (\psi_d i_q - \psi_q i_d)$.

The equations can be simplified by considering steady-state operation, in which the dq currents are constant:

$$\frac{di_d}{dt} = 0, \qquad \frac{di_q}{dt} = 0$$

At high speed the resistive drop is negligible compared with the motional terms, and the

voltage equations reduce to [17]:

$$v_d \approx -\omega L_q i_q \tag{78}$$

$$v_q \approx \omega L_d i_d \tag{79}$$

The maximum voltage that the converter can apply is limited by the DC-link voltage and by the adopted modulation strategy [3]. With SVPWM in the linear modulation range and the amplitude-invariant transformation, the maximum amplitude of the voltage vector is $V_{max} = V_{dc}/\sqrt{3}$:

$$v_d^2 + v_q^2 \leq V_{max}^2 \tag{80}$$

By substitution:

$$(\omega L_q i_q)^2 + (\omega L_d i_d)^2 \leq V_{max}^2 \tag{81}$$

and dividing by ω^2:

$$L_d^2 i_d^2 + L_q^2 i_q^2 \leq \left(\frac{V_{max}}{\omega}\right)^2 = R_v^2 \tag{82}$$

which is the equation of an ellipse centred at the origin of the dq plane, with semi-axes along the d and q axes, respectively:

$$a = \frac{R_v}{L_d} = \frac{V_{max}}{\omega L_d} \qquad b = \frac{R_v}{L_q} = \frac{V_{max}}{\omega L_q} \tag{83}$$

Since $L_d > L_q$, the semi-axis along q is the longer one ($b > a$), and the ellipse is elongated in the direction of the q axis. Unlike the SPM case, where the voltage limit is a circle centred at $(-\psi_m/L_s, 0)$, the absence of permanent magnets places the centre at the origin. As the equations show, the ellipses shrink as the electrical speed increases [17]. This constraint must be respected in field-weakening operation, otherwise the machine could be driven towards an operating point that cannot be sustained because of the lack of voltage. When saturation is considered, L_d and L_q vary with the operating point, and

the voltage limit becomes a deformed ellipse: this is why its intersection with the current limit is computed numerically.

The current constraint, on the other hand, represents a thermal limit of the machine. It is a rating-plate limit of the stator windings and, unlike the voltage constraint, it does not depend on the rotational speed [10]:

$$i_d^2 + i_q^2 \leq I_{max}^2 \tag{84}$$

It is represented by a circle of radius I_{max} centred at the origin of the dq plane. The current vector I_s must always lie inside this circle and inside the voltage ellipse corresponding to the required electrical speed. Both constraints are shown in Fig. 7, which gives an overview of the admissible operating points [10, 17].

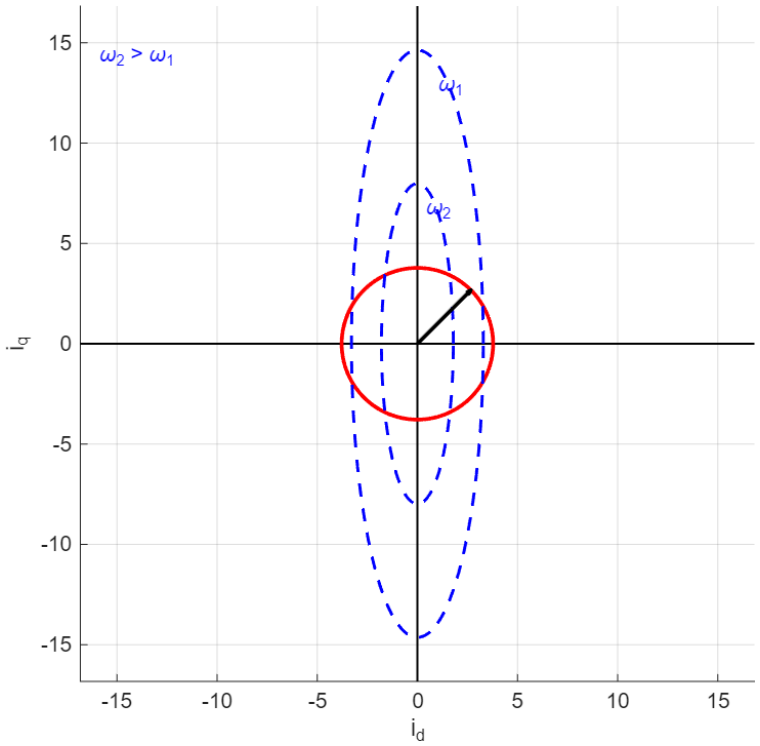


Figure 5: Voltage ellipses and current circle in the dq plane.

4 Control Strategies

4.1 Common features

This chapter will discuss all the common features among the different control strategies, such as the MTPA algorithm, machine management under field-weakening conditions, ramps and speed PI, and the modulation method used in the simulations. The following is a block diagram of the general structure of the four simulations. Some of these blocks will be reused throughout the thesis, and therefore the introductory chapter on control strategies is dedicated to these features. The four models differ only in the strategies used in the inner current loop, each with its own peculiarities.

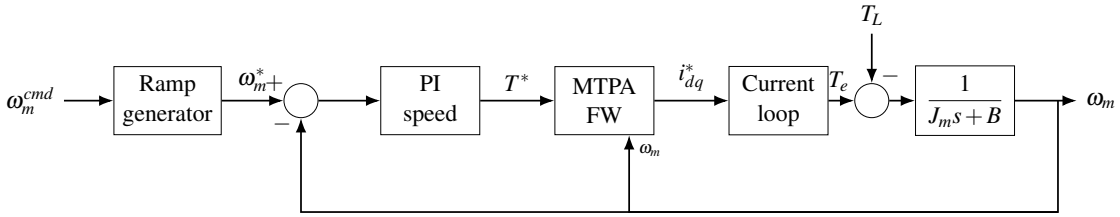


Figure 6: General Block diagram

4.1.1 MTPA, FW and MTPV control

The MTPA (maximum torque per ampere) function aims to identify the values of i_d and i_q that allows the electromagnetic torque value required by the speed loop to be reached. This involves identifying the minimum of the torque function with respect to the angle β between the vector $\vec{I_s}$ and the axis d of the dq plane. Setting:

$$i_d = I_s cos(\beta) \tag{85}$$

$$i_q = I_s sin(\beta) \tag{86}$$

and starting from the torque equation 68, we can obtain:

$$C_m = \frac{3}{2} p_p (L_d - L_q) I_s^2 cos(\beta) sin(\beta) \tag{87}$$

and using the double-angle formula:

$$sin(2\beta) = 2cos(\beta)sin(\beta) \tag{88}$$

we obtain the torque equation shown as a function of the angle β.

$$C_m = \frac{3}{4} p_p (L_d - L_q) I_s^2 sin(2\beta) \tag{89}$$

Deriving with respect to β:

$$\frac{dC_m}{d\beta} = \frac{3}{2} p_p (L_d - L_q) I_s^2 \cos(2\beta) = 0 \tag{90}$$

which is satisfied for $\beta = 45$.

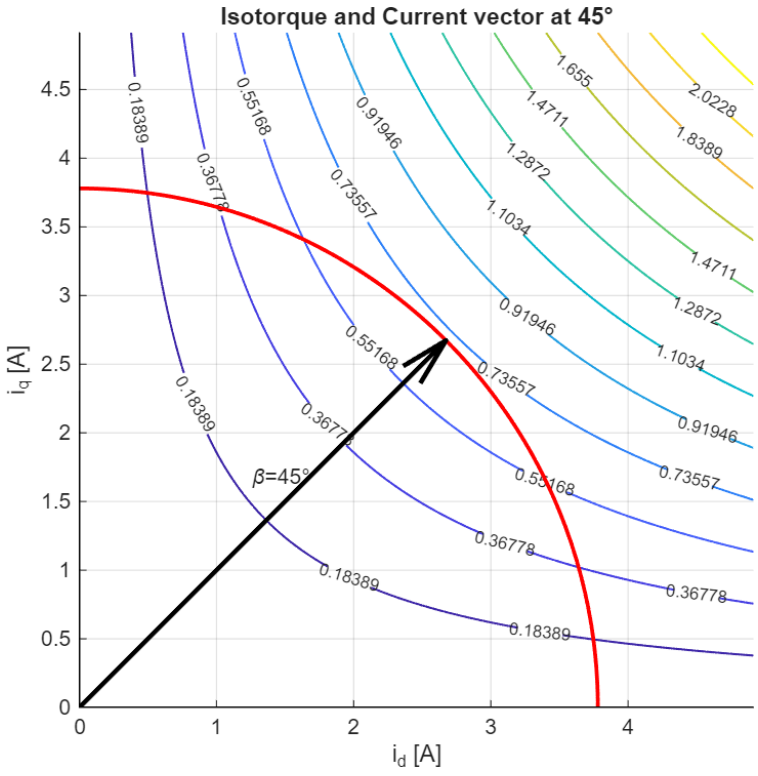


Figure 7: Isotorque in dq plane

To find the maximum torque per ampere, an iterative numerical method, Newton's method, is used. This root finding algorithm produces progressively better approximations of the zeros of a real-valued function. The aim is to find the pair of currents on

the dq plane that allow the required torque to be achieved, formulating the problem in polar form:

$$i_d = I_s cos(\beta)$$
$$i_q = I_s sin(\beta)$$

The problem then is reduced to finding, for each θ of the search grid, the root of the scalar function:

$$f(r) = C_m(r,\theta) - C_{ref} = 0 \tag{91}$$

Newton's method locally approximates $f(r)$ with its tangent and calculates its intersection with the x axis, iteratively updating the estimate:

$$r_{k+1} = r_k - \frac{f(r_k)}{f'(r_k)} \tag{92}$$

The derivative $f'(r)$ is estimated numerically using the forward Euler method:

$$f'(r) \approx \frac{f(r+\varepsilon) - f(r)}{\varepsilon} \tag{93}$$

In the implementation, ε was chosen to be equal to 10 mA. At each iteration, therefore, two evaluations of the torque are required, to estimate the derivative and calculate the next step. The iteration stops when the variation between two successive steps is negligible:

$$r_k \leftarrow \max(r_k,\ 0.01\, I_n) \tag{94}$$

The method is repeated for each angle within a sufficiently large round of the theoretical value of 45°. Of all the angles for which the Newton converges within tolerance, the one with the smallest radius is selected:

$$r^\star = \min_\theta \{ r(\theta)\ :\ |C_{ref} - C_m(r(\theta),\theta)| \leq 0.01\, |C_{ref}| \} \tag{95}$$

In the implementation, I chose to set a rejection condition, meaning I evaluate the torque from each angle, and if it is greater than the threshold value by 1%, I move on to the evaluation of the next angle. If no angle converges within tolerance to C_{ref} with $|i_s| \leq I_n$, a scan is performed using $|i_s| = I_n$ to find the point of maximum achievable torque, the protection ensure a returns with physically valid operating point rather than diverging or failing to converge.

The Newton method, applied here to the search for the MTPA, takes from the classical iterative scheme [23], widely used in the analysis of power systems for the resolution of non linear equations (for example in load flow).

Once ω_b is exceeded, the MTPA is no longer admissible, because the voltage constraint is active, so the point of maximum deliverable torque must be found, respecting the voltage and current constraints, simultaneously. In this case, two conditions are possible. The first occurs when the required torque C_{ref} is greater than or equal to the torque deliverable at a given speed greater than ω_b, while the second condition occurs when the required speed is greater than ω_b but the required torque C_{ref} is within the current circumference. To manage these two conditions, two different strategies have been implemented. When faced with the first condition in Field Weakening, the optimal operating point is at the intersection of the current circumference constraint and the voltage ellipse constraint.

$$i_d^2 + i_q^2 = I_n^2 \qquad L_d^2 i_d^2 + L_q^2 i_q^2 = R_v^2 \tag{96}$$

Solving the system by substitution:

$$i_d = \sqrt{\frac{R_v^2 - I_n^2 L_q^2}{L_d^2 - L_q^2}} \qquad i_q = \sqrt{I_n^2 - i_d^2} \tag{97}$$

Since L_d and L_q depend to i_d and i_q, the closed formula cannot be solved in a single step: therefore, L_d and L_q are recalculated at each new current point, and repeating until convergence. The iteration stops when the variation between two successive iterations, on

both components of the current vector, falls below a predetermined tolerance:

$$\left|i_d^{(k)} - i_d^{circ}\right| < \delta_{tol} \quad \text{AND} \quad \left|i_q^{(k)} - i_q^{circ}\right| < \delta_{tol} \tag{98}$$

When we encounter the second condition, that is, when the required torque is less than the available torque at that given speed, the machine will operate within the current circumference and on the edge of the voltage ellipse. Again, by describing the currents in polar coordinates:

$$i_d = I_s cos(\beta)$$
$$i_q = I_s sin(\beta)$$

we proceed iteratively for each angle θ, identifying the only radius that satisfies the imposed voltage constraint. In this case, too, Newton's method is selected. For a given angle θ, the radius that exactly satisfies the voltage constraint $|\psi| = R_v$ is obtained directly from:

$$|\psi(r,\theta)| = r\sqrt{(L_d \cos\theta)^2 + (L_q \sin\theta)^2} = R_v \tag{99}$$

obtaining:

$$r(\theta) = \frac{R_v}{\sqrt{(L_d \cos\theta)^2 + (L_q \sin\theta)^2}} \tag{100}$$

The radius is therefore limited by the more stringent of the two constraints:

$$r_{max}(\theta) = \min\left(I_n,\ r(\theta)\right) \tag{101}$$

For each θ within the selected set, $f(r) = C_m(r,\theta) - C_{ref} = 0$ is solved exactly as in the MTPA algorithm, with the only difference that at each iteration the radius is also limited above $r_{max}(\theta)$, as well as below $0.01\,I_n$:

$$r_k \leftarrow \min\left(\max(r_k,\ 0.01\,I_n),\ r_{max}(\theta)\right) \tag{102}$$

Among all the angles that converge within 1% tolerance on the torque, the one with the

minimum radius is selected. In summary, the same method used in the MTPA is used [23], but with the maximum current radius no longer fixed at I_n, but varying as a function of the ellipse.

Once a certain ω_c is exceeded, the final control zone is reached, where a strong field weakening occurs. Here, it is decided to intentionally lower i_d and i_q refefences proportionally with the increase in the required speed. This results in a significant reduction of the available torque. The chosen critical speed is derived from the MTPA calculated with the complete inductance matrix. The image below shows the behavior of the MTPA control algorithm in the presence of the apparent inductance matrices, compared to the behavior of the MTPA in the presence of the complete inductance matrix.

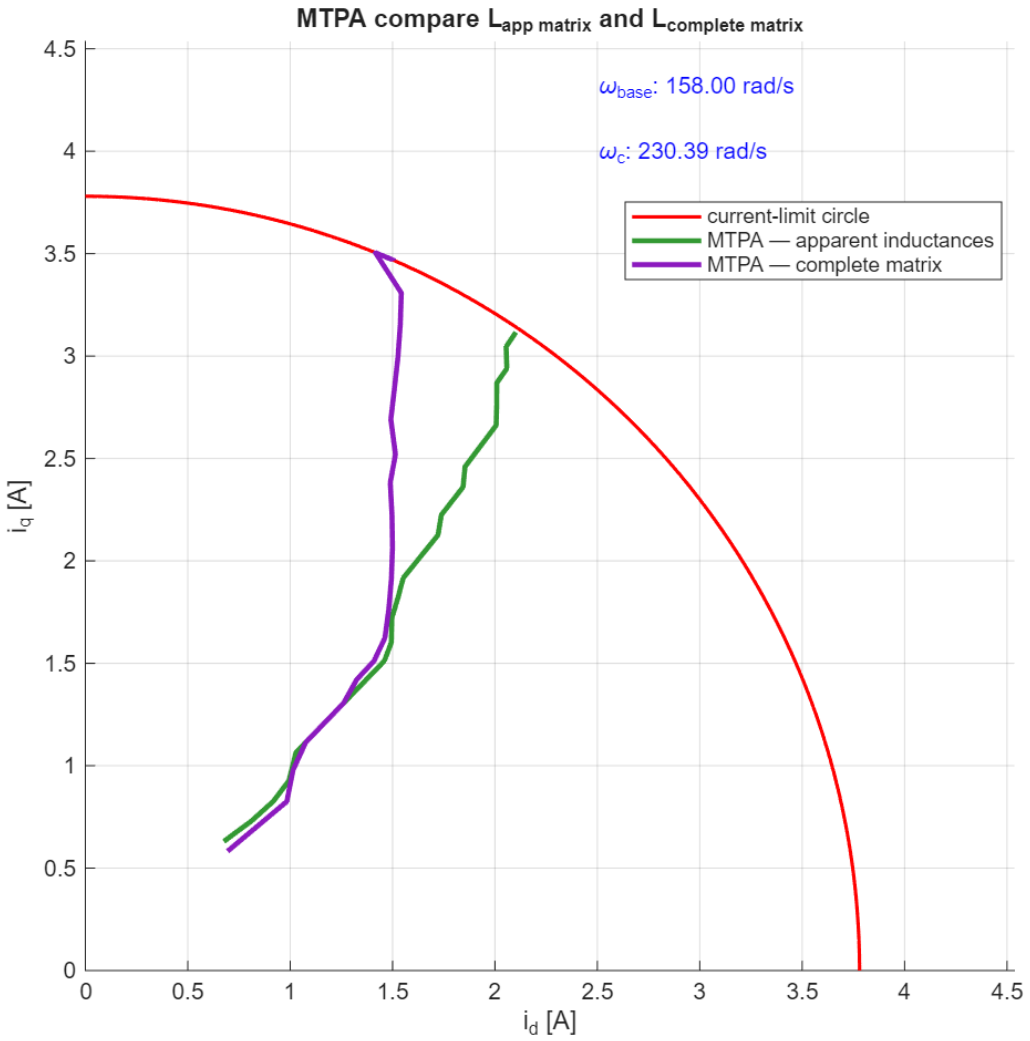


Figure 8: Complete inductances matrix vs Apparent inductances matrix

From the intersection point between the current circumference and the MTPA

calculated with the complete matrices, the critical speed ω_c is derived, beyond which the maximum available torque is reduced. By fixing the radius to ω_c, the radius is scaled according to the required ω, according to:

$$r = \frac{\omega_c}{\omega}\sqrt{i_d^2 + i_q^2} \tag{103}$$

From which the references of i_d and i_q are derived.

$$i_d(\omega) = r * cos(\theta) \tag{104}$$

$$i_q(\omega) = r * sin(\theta) \tag{105}$$

4.1.2 Speed ramp control

The speed ramp allows to limit the speed derivative, thus limiting sudden changes in the speed PI. This, in turn, avoids sudden changes in the generated torque reference, and therefore current, thus avoiding mechanical stress on the motor shaft. The slope is calculated as:

$$y_{k+1} = y_k \pm \frac{|y_{\text{target}}|}{t_{\text{ramp}}} \cdot dt \tag{106}$$

So the step for each period is:

$$\text{step} = \text{slope} \cdot dt \tag{107}$$

With each call, the value go forward one step in the direction of the target with constant acceleration [24] .

4.1.3 Speed PI controller

Starting from the mechanical equation of the SynRM motor, its transfer function is obtained [11]:

$$J_m \frac{d\omega_m}{dt} + B\,\omega_m = T_m - T_L \tag{108}$$

where J_m is the total moment of inertia referred to the motor shaft, B the viscous friction coefficient, ω_m the mechanical angular speed, T_m the electromagnetic torque produced by the machine and T_L the load torque opposing the motion.

and applying the Laplace transform under zero load conditions:

$$J_m s\,\omega_m(s) + B\,\omega_m(s) = T_m(s) - T_L(s) \tag{109}$$

the derivative operator is replaced by the complex variable s, under the assumption of zero initial speed, so that the differential equation becomes algebraic in the Laplace domain.

$$\omega_m(s) = \frac{1}{J_m s + B}\left[T_m(s) - T_L(s)\right] \tag{110}$$

the speed response is therefore governed by a first-order lag with time constant J_m/B and static gain $1/B$, driven by the net torque acting on the shaft.

The transfer function is:

$$G_m(s) = \left.\frac{\omega_m(s)}{T_e(s)}\right|_{T_L=0} = \frac{1}{J_m s + B} \tag{111}$$

$G_m(s)$ is the mechanical plant seen by the speed controller, that transfer from the torque command to the shaft speed, with the load torque treated as an external disturbance and set to zero for design purposes.

Defining the ratio $a = K_{i\omega}/K_{p\omega}$, the controller becomes:

$$G_{PI}(s) = K_{p\omega}\left(1 + \frac{a}{s}\right) = K_{p\omega}\,\frac{s+a}{s} \tag{112}$$

$K_{p\omega}$ and $K_{i\omega}$ are the proportional and integral gains of the speed regulator, while a locates the controller zero and thus fixes the frequency below which the integral action dominates and the open-loop transfer function, neglecting B:

$$L(s) \approx \frac{K_{p\omega}}{J_m} \cdot \frac{s+a}{s^2} \tag{113}$$

the viscous term is dropped because $B \ll J_m \omega_n$ in the frequency range of interest, leaving a double pole at the origin given by the mechanical integration and by the integral action

of the controller.

The closed-loop comparison with the canonical second-order form $s^2 + 2\zeta\omega_n s + \omega_n^2$ yields:

$$K_{p\omega} = 2\zeta\omega_n J_m \qquad a = \frac{\omega_n}{2\zeta} \tag{114}$$

ω_n is the desired natural frequency of the speed loop and ζ its damping factor: the two design specifications map directly onto the proportional gain and onto the position of the controller zero.

From the definition of a, the integral gain follows as:

$$K_{i\omega} = a\,K_{p\omega} = \frac{\omega_n}{2\zeta} \cdot 2\zeta\omega_n J_m = \omega_n^2 J_m \tag{115}$$

the damping factor cancels out, so the integral gain depends only on the target bandwidth and on the inertia, and scales with the square of ω_n.

Furthermore, by separating the bands of the control loops, with the internal current loop having a bandwidth at least an order of magnitude faster [11], its behavior approximates ideal:

$$T_m(s) = T^*(s) \tag{116}$$

T^* is the torque reference issued by the speed controller: since the current loop settles well before the mechanical dynamics react, its own dynamics can be replaced by a unity gain in the speed-loop design.

Multiplying the terms of the direct chain together, we obtain the open-loop transfer function:

$$L(s) = G_{PI}(s)\,G_m(s) = \frac{K_{p\omega}\,s + K_{i\omega}}{s\,(J_m s + B)} \tag{117}$$

this is the exact open-loop gain of the cascade controller-plant, with the viscous term retained: the pole at the origin comes from the integrator and guarantees zero steady-state error against a constant speed reference.

Here below a simplified speed loop used for the PI design, the current loop is assumed ideal ($T_m = T^*$), so the plant reduces to the mechanical transfer function.

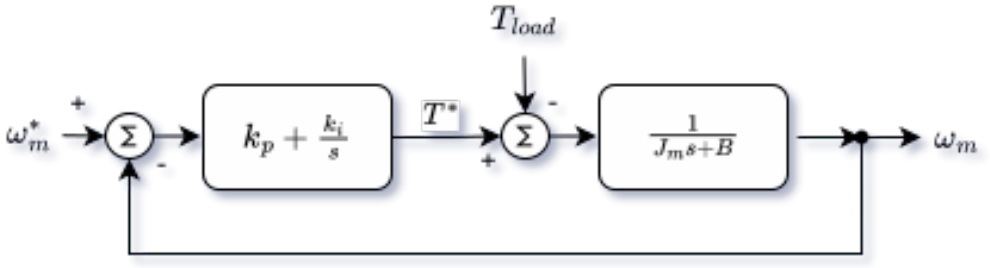


Figure 9: PI loop and plant diagram

4.1.4 Space Vector modulation

Space Vector Modulation was used in the simulations implemented in this thesis. Specifically, in the simulation implementing PI control and the one implementing Non-linear Dynamic Inversion control, a modulator for generating gate signals is essential. For predictive control, however, this functionality is not necessary; the gate pulses are directly generated by the control strategy itself. SVPWM (space vector PWM) modulation was selected because it is the most widely used in electric drives, along with the third harmonic injection method on classic sinusoidal modulation. The modulation method for two-level inverters is presented below, the method presented below was taken from the book High-Power Converters and AC Drives [25]. The operating states can be represented as in the table below, where, for example, state ”110” indicates that switches S1, S3, and S2 are conductive. As underlined by the table the vector components are obtained through

Table 2: Voltage vectors of the two-level three-phase inverter

Configuration	IGBT state	$V_{s\alpha}$	$V_{s\beta}$	$\lvert V_s \rvert$	θ
0 (V_{s0})	000	0	0	0	–
1 (V_{s1})	100	$\frac{2}{3}V_{dc}$	0	$\frac{2}{3}V_{dc}$	0
2 (V_{s2})	110	$\frac{1}{3}V_{dc}$	$\frac{1}{\sqrt{3}}V_{dc}$	$\frac{2}{3}V_{dc}$	$\pi/3$
3 (V_{s3})	010	$-\frac{1}{3}V_{dc}$	$\frac{1}{\sqrt{3}}V_{dc}$	$\frac{2}{3}V_{dc}$	$2\pi/3$
4 (V_{s4})	011	$-\frac{2}{3}V_{dc}$	0	$\frac{2}{3}V_{dc}$	π
5 (V_{s5})	001	$-\frac{1}{3}V_{dc}$	$-\frac{1}{\sqrt{3}}V_{dc}$	$\frac{2}{3}V_{dc}$	$4\pi/3$
6 (V_{s6})	101	$\frac{1}{3}V_{dc}$	$-\frac{1}{\sqrt{3}}V_{dc}$	$\frac{2}{3}V_{dc}$	$5\pi/3$
7 (V_{s7})	111	0	0	0	–

the amplitude-invariant Clarke transformation, with factor $\frac{2}{3}$, consistent with the control side implementation: the amplitude of the active vectors, $\frac{2}{3}V_{dc}$, coincides with the peak

value of the phase voltage. The null vectors V_{s0} and V_{s7} produce the same null voltage and their angle is undefined, they are called zero space vectors. V_{s0} and V_{s7} vectors differ only in the switch states, and choosing between them in the SVPWM sequence minimizes the number of switching operations. Assuming that the three-phase system is perfectly balanced, we have:

$$V_{an} + V_{bn} + V_{cn} = 0 \tag{118}$$

where V_{an}, V_{bn}, and V_{cn} are the phase voltages of the load applied to the two-level inverter. From a mathematical point of view, one of the three phases is redundant, in fact given two voltages, the third is directly calculable. For this reason, it is possible to transform the three-phase system into an equivalent two-phase system.

$$\begin{bmatrix} V_\alpha \\ V_\beta \\ V_0 \end{bmatrix} = \frac{2}{3} \begin{bmatrix} cos(\theta) & cos(\theta - \frac{2\pi}{3}) & cos(\theta + \frac{2\pi}{3}) \\ -sin(\theta) & -sin(\theta - \frac{2\pi}{3}) & -sin(\theta + \frac{2\pi}{3}) \\ \frac{1}{2} & \frac{1}{2} & \frac{1}{2} \end{bmatrix} \begin{bmatrix} V_{a0} \\ V_{b0} \\ V_{c0} \end{bmatrix} \tag{119}$$

with $\theta = 0$

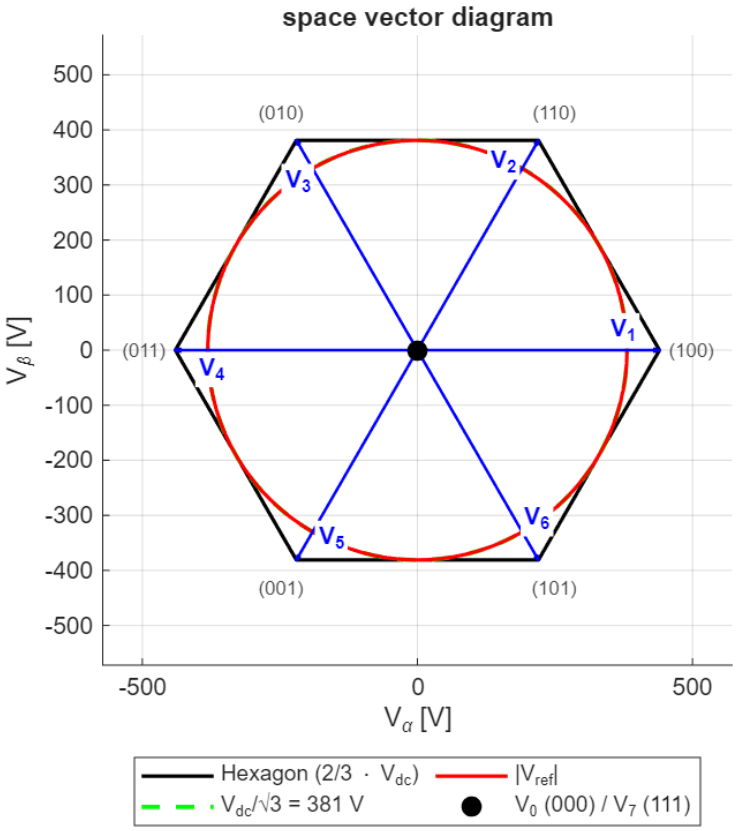


Figure 10: Space vector diagram

The Voltage vector can be expressed as:

$$\vec{V} = V_\alpha + jV_\beta \tag{120}$$

in the $\alpha\beta$ plane, and define the rotation operator:

$$\alpha = e^{j\frac{2\pi}{3}} = -\frac{1}{2} + j\frac{\sqrt{3}}{2} \tag{121}$$

from which:

$$\alpha^2 = e^{j\frac{4\pi}{3}} = -\frac{1}{2} - j\frac{\sqrt{3}}{2} \qquad \alpha^3 = 1 \qquad 1 + \alpha + \alpha^2 = 0 \tag{122}$$

The space vector becomes:

$$\vec{V} = \frac{2}{3}\left(V_{a0} + \alpha V_{b0} + \alpha^2 V_{c0}\right) \tag{123}$$

It is important to emphasize that the space vectors, active and zero, are fixed in space, while the reference voltage vector V_{ref} rotates in the plane at a frequency equal to $2\pi f$, where f is the frequency of the inverter's output voltage. From this consideration, given the amplitude and direction of the reference voltage vector V_{ref}, it is possible to identify the three closest stationary vectors. Based on this, the inverter switches will be activated or deactivated via the gate signals they generate. When the reference voltage vector V_{ref} passes through the sectors, different switches will be selected. Therefore, complete rotation in the space of V_{ref} corresponds to one period of the output fundamental Voltage in time. The voltage vector dwell time represents the duty cycle of the selected switches during a sampling period T_s. The calculation of the dwell time is based on the volt-second balancing principle, which states that the product of the reference voltage value V_{ref} multiplied by the sampling period T_s, is equal to the sum of the voltage value of the selected space vectors by the time used for each of them.

$$\begin{cases} \vec{V}_{\text{ref}}\, T_s = \vec{V}_k\, T_k + \vec{V}_{k+1}\, T_{k+1} \\ T_s = T_k + T_{k+1} + T_0 \end{cases} \tag{124}$$

Where T_k, T_{k+1}, and T_0 are the dwell times of the space vectors V_k, V_{k+1}, and V_0.
Projecting the volt-second balance onto the $\alpha\beta$ axes and solving for the two unknowns, the dwell times of the active vectors are obtained in closed form, where $\theta \in [0,\ \pi/3)$ is the angle of V_{ref} measured from the leading vector V_k of the sector:

$$\begin{aligned} T_k &= \frac{\sqrt{3}\, T_s\, |\vec{V}_{ref}|}{V_{dc}} \sin\Big(\frac{\pi}{3} - \theta\Big) \\ T_{k+1} &= \frac{\sqrt{3}\, T_s\, |\vec{V}_{ref}|}{V_{dc}} \sin(\theta) \\ T_0 &= T_s - T_k - T_{k+1} \end{aligned} \tag{125}$$

The residual time T_0 is split between the two zero vectors V_{s0} and V_{s7}, so that the pulses are centred within the sampling period and only one leg switches at each transition. The maximum amplitude of the reference voltage vector is equal to the radius of the maximum circle inscribed in the hexagon of the space vectors. The intersection point between a side of the hexagon and the inscribed circle is located halfway along the side of the hexagon,

that is, at 30° with respect to the direct axis. Therefore, multiplying the space vector by the cosine of thirty degree yields the maximum voltage that can be expressed by the reference voltage vector.

$$V_{ref,max} = \frac{2}{3} V_{dc} \frac{\sqrt{3}}{2} = \frac{V_{dc}}{\sqrt{3}} \tag{126}$$

The maximum rms phase-to-phase voltage will be equal to:

$$V_{ref,SVPWM} = \sqrt{3}\left(\frac{V_{ref,max}}{\sqrt{2}}\right) = 0.707 V_{dc} \tag{127}$$

The maximum voltage that can be expressed by the classic sinusoidal PWM is equal to:

$$V_{ref,SPWM} = 0.612 V_{dc} \tag{128}$$

We can therefore state that the ratio between the two maximum voltages is equal to 1.155, indicating that SVPWM modulation is capable of generating 15.5% more voltage than the classic modulation scheme. Immediately below, you can see the duty signal behavior of phases A, B, and C for SVPWM modulation.

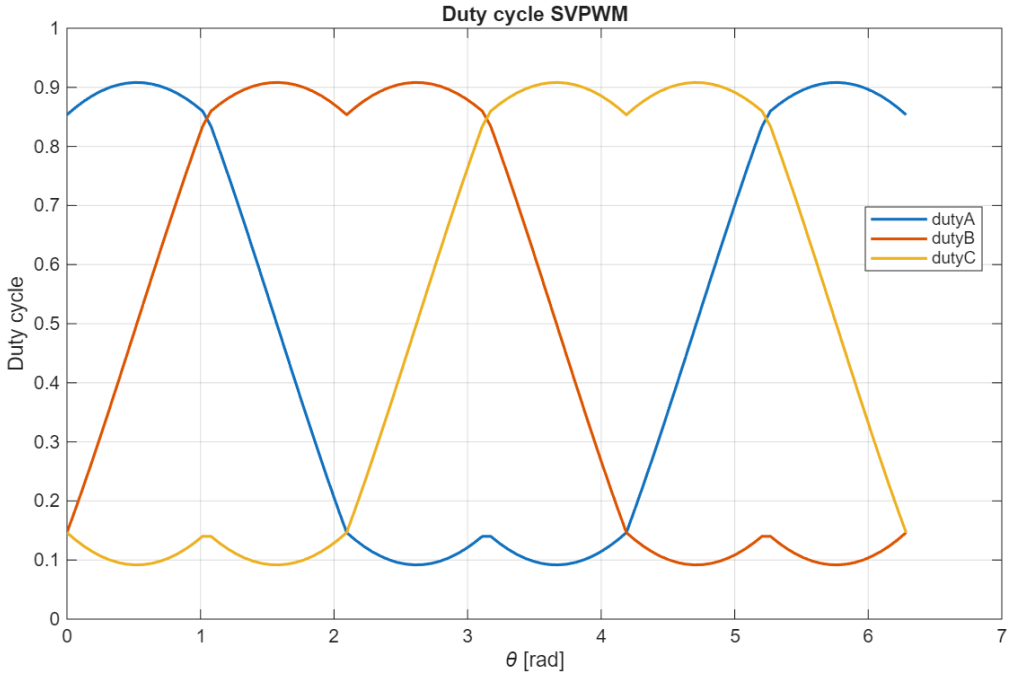


Figure 11: A, B and C phases duty

It should be noted that by injecting the third harmonic into classic PWM modulation, it is possible to achieve the same increase in generated voltage, obtaining the same DC voltage utilization.

4.2 PI Current Control

Starting from the mathematical model of the system seen previously 3.1, and represented in the image below [11]:

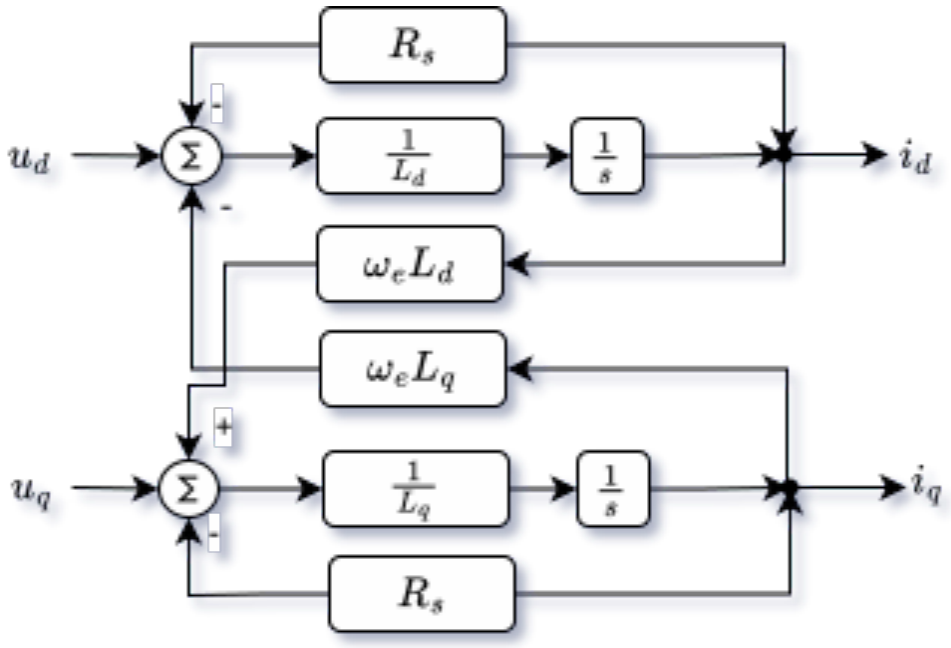


Figure 12: Mathematical model of SynRM motor

where the terms $\omega L_d i_d$ and $\omega L_q i_q$ are the axis coupling terms, by implementing the decoupling network, the system can be treated as an independent first-order system [11], whose voltage-current transfer function is:

$$Plant(s) = \frac{i(s)}{v(s)} = \frac{1}{Ls + R_s} = \frac{b}{s+d}, \qquad b = \frac{1}{L}, \quad d = \frac{R_s}{L}, \tag{129}$$

where L takes the value L_d or L_q depending on the axis considered. The apparent inductances of Eqs. (70)–(71) are used, consistently with the decoupling network; a rigorous description of the current dynamics would require the differential inductances, which in the saturated region are smaller and therefore make the actual loop faster and less damped

than the nominal design. The cross terms L_{dq}^{inc} and L_{qd}^{inc} are neglected, leaving the residual coupling to the integral action.

The regulator is a PI in the form: $C(s) = K_p\,(s+a)/s$, with $a = K_i/K_p$ The closed loop transfer function is

$$G_{cl}(s) = \frac{K_p b\,(s+a)}{s^2 + (d + K_p b)\,s + K_p b\,a}. \tag{130}$$

By identifying the denominator of the closed-loop transfer function just found, with the canonical form of a second-order system $s^2 + 2\zeta\omega_0 s + \omega_0^2$ we obtain the gain expressions

$$K_p = \frac{2\zeta\omega_0 - d}{b} = 2\zeta\omega_0 L - R_s, \qquad K_i = aK_p = \omega_0^2 L, \tag{131}$$

where the resistive contribution cancels out in the integral gain expression, which therefore depends only on the axis inductance and the desired natural pulsation. The regulators are calibrated by imposing the damping factor ζ and the natural frequency $f_i = \omega_0/2\pi$ on both axes [11]; the values adopted in simulation and on the test bench are reported in Sections **??** and 6.4 respectively. It should be noted that f_i is the natural frequency and not the closed-loop bandwidth, which is higher because of the zero at $-a$; the same zero also increases the overshoot with respect to the value expected from ζ alone. In choosing f_i, the current loop must remain well above the speed loop and well below the sampling frequency.

Since the regulator output is bounded by the available inverter voltage, the integral state is protected by back-calculation: whenever the unsaturated output u_k differs from the saturated one $u_{sat,k}$, the state is recomputed as $x_{k+1} = x_k + (u_{sat,k} - u_k)/K_i$, so that the regulator output lies on the saturation boundary and the state stays consistent with the voltage actually applied. This is relevant in field weakening, where the voltage limit is active by design.

It should be noted that the design of the PIs is closely linked to the values of the system parameters, since the inductances L_d and L_q are a function of the operating point due to magnetic saturation. The defined gains will therefore be optimal for a specific operating point and not for the entire operating range of the SynRM motor.

4.3 Model-Based predictive Control

The MPC (model predictive control) control technique has been adopted in power electronics since the 1980s, although the application of optimal control concepts dates back two decades. The first applications in the 1980s were limited to low-switching frequency converters due to computer limitations and the increased computation times required by this control strategy [26].

The application of this strategy has increased considerably with the development of faster and more powerful microprocessors [27]. The general behaviour of the predictive controller family, of which the MPC strategy is only one example, is the use of a system model, which must be as faithful to reality as possible, to predict future behaviour up to a given time horizon and then select optimal actions to minimize a cost function representing the desired system behaviour. The framework offers several advantages, including great versatility in application across different types of systems, easy understanding of the applied concepts, and simple constraint management.

On the other hand, there are also disadvantages, including higher computational costs. The fidelity of the model used must be as accurate as possible, otherwise, may encounter situations where minimizing a cost function does not lead to the desired results. As previously mentioned, the basic structure of the predictive model is made up of three key elements: using a model to predict future behaviour, a cost function that represents the desired result and then implementing the actions necessary to minimize the cost function. The MPC method is applied to the current control problem, with the same two level and three phase power converter. The converter used therefore has a defined set of switching states, which can be used to predict the behaviour of the variables in each state. To select the appropriate switching state, a selection criterion must be defined. The selection criterion for the switching state to be implemented consists of evaluating the cost function for each of the predicted states and then choosing the one that minimizes the function [28]. The method therefore requires the knowledge of the model already seen in section 3.1 .

The stator voltage equations of the SynRM in the rotor reference frame, already derived as (61) and (62), are for prediction purposes written with the currents as state variables, so the equations must be solved with respect to their derivatives.

$$\frac{\mathrm{d}i_d}{\mathrm{d}t} = \frac{1}{L_d}\Big(v_d - R_s i_d + \omega L_q i_q\Big), \tag{132}$$

$$\frac{\mathrm{d}i_q}{\mathrm{d}t} = \frac{1}{L_q}\Big(v_q - R_s i_q - \omega L_d i_d\Big). \tag{133}$$

Each derivative is driven by three contributions: the applied voltage, the resistive drop, and the cross-coupling term produced by the rotation of the reference frame. Unlike the PI scheme of Chapter section 4.2 , which requires an explicit decoupling network, the predictive controller embeds the coupling in the model and therefore accounts for it intrinsically.

Collecting the states in $\mathbf{x} = [i_d \;\; i_q]^T$ and the inputs in $\mathbf{u} = [v_d \;\; v_q]^T$, (132) and (133) take the compact state-space form

$$\frac{\mathrm{d}\mathbf{x}}{\mathrm{d}t} = \mathbf{A}\,\mathbf{x} + \mathbf{B}\,\mathbf{u}, \qquad \mathbf{A} = \begin{bmatrix} -\dfrac{R_s}{L_d} & \dfrac{\omega L_q}{L_d} \\ -\dfrac{\omega L_d}{L_q} & -\dfrac{R_s}{L_q} \end{bmatrix}, \qquad \mathbf{B} = \begin{bmatrix} \dfrac{1}{L_d} & 0 \\ 0 & \dfrac{1}{L_q} \end{bmatrix}. \tag{134}$$

The state matrix $\mathbf{A}$ depends on the electrical speed ω, so the system is linear but time-varying; since ω changes slowly with respect to the sampling period, it is treated as a constant parameter updated at every sampling instant.

The controller operates at a fixed sampling period T_s, and the voltage vector applied by the inverter is held constant throughout each interval. The derivatives in (132) and (133) can therefore be approximated by forward Euler differences,

$$\frac{\mathrm{d}i}{\mathrm{d}t} \approx \frac{i(k+1) - i(k)}{T_s}, \tag{135}$$

where k denotes the current sampling instant and $k+1$ the next one. The approximation is acceptable provided T_s is small compared with the electrical time constants L_d/R_s and L_q/R_s of the machine.

Substituting (135) into (132)–(133) and solving for the future currents gives the second form, that is the prediction model actually evaluated by the controller:

$$i_d^p(k+1) = i_d(k) + \frac{T_s}{L_d}\Big[v_d(k) - R_s\, i_d(k) + \omega(k)\, L_q\, i_q(k)\Big], \tag{136}$$

$$i_q^p(k+1) = i_q(k) + \frac{T_s}{L_q}\Big[v_q(k) - R_s\, i_q(k) - \omega(k)\, L_d\, i_d(k)\Big], \tag{137}$$

where the superscript p marks a predicted quantity. Grouping the terms in $i_d(k)$ and $i_q(k)$ makes the structure of the recursion more explicit:

$$i_d^p(k+1) = \left(1 - \frac{R_s T_s}{L_d}\right) i_d(k) + \frac{\omega(k)\, L_q\, T_s}{L_d}\, i_q(k) + \frac{T_s}{L_d}\, v_d(k), \tag{138}$$

$$i_q^p(k+1) = \left(1 - \frac{R_s T_s}{L_q}\right) i_q(k) - \frac{\omega(k)\, L_d\, T_s}{L_q}\, i_d(k) + \frac{T_s}{L_q}\, v_q(k). \tag{139}$$

Equations (138)–(139) are evaluated once for each of the voltage vectors available from the two-level inverter. The measured currents $i_d(k)$, $i_q(k)$ and the measured speed $\omega(k)$ are common to all evaluations, so only the input term changes from one candidate to the next: $v_d(k)$ and $v_q(k)$ are the Park projections of the vector under test. Each prediction is scored by a cost function that measures how far the predicted currents lie from their references, generated by the MTPA and field weakening strategy of section 4.1.1:

$$g_j = \left|i_d^* - i_{d,j}^p(k+1)\right| + \left|i_q^* - i_{q,j}^p(k+1)\right|, \qquad j = 0, \ldots, 7, \tag{140}$$

where j indexes the eight switching states of the two-level inverter and i_d^*, i_q^* are the current references. The vector minimising g_j is applied during the following sampling interval. The absolute value weights both axes equally; alternative formulations use the squared error, or add terms penalising the switching frequency or enforcing constraints [28].

It is important to note that for simplicity, the model assumes that the reference current does not change significantly over the sampling interval, so we will consider $i^*(k+1) = i^*(k)$. This assumption may introduce a delay of one sample in tracking the reference, which is not a problem if a high sampling rate is considered. A second delay arises from

the computation itself: the vector selected at the instant k is actually applied during the following interval, when the currents have already evolved. The formulation adopted here keeps a one step horizon and does not compensate this actuation delay, so the decision is optimal with respect to the state measured at k rather than to the state at which the vector is applied. The known effect is an increased current ripple and a tendency to alternate between adjacent vectors. The standard remedy [28] is a two step prediction, in which the state at $k+1$ is first estimated using the vector already applied and the candidates are then evaluated at $k+2$; its implementation is left as a possible extension.

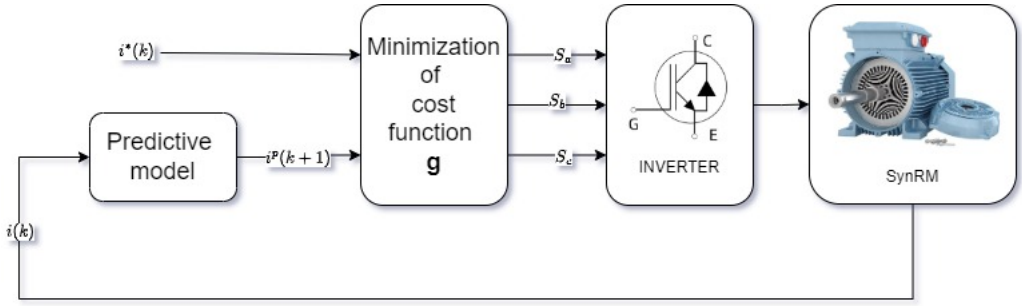


Figure 13: Predictive current control block diagram

The image 13 highlights the central role of the cost function which actually determines the distance between the given references and those predicted by the model.

4.4 Model-Free Predictive Control

From the previous chapters on PI-based models section 4.2 and predictive models with MPC algorithms section 4.3, a series of limitations are evident. The first major limitation is the need to know the system model, for example, eq. (138) and eq. (139) of the model based strategy. However, the system's characteristic parameters vary over time and vary as a function of operating conditions, so a model to follow should be variable. This implies a computational cost that is too high to sustain, which is generally not a desirable condition in industrial applications. Furthermore, the initial parameter identification process is not simply solvable, and therefore is another aspect to consider and deserves more careful consideration. As the system evolves over time, it could diverge from the model used, thus leading to a marked degradation in performance [29]. The idea to address these issues is to observe the control system's input and output values in the narrow

neighbourhood of the current operating point, rather than estimating the global behavior of the system being governed. This idea has given rise to a new category of controllers based on online variable verification, called MFPC (model-free predictive control).
In some of these MFPC controls, the data-driven model is replaced by a lock-up table containing the control system's input and output data, which is updated at each sampling cycle. The model is then linearized, attempting to predict the system's behavior. There are different types of MFPC controls; in this case, the ultra-local strategy is used. This method is very similar to the original approach of model-free strategies, which uses a model with one or more uncertain terms, estimated online by analysing the system's inputs and outputs. The general block diagram of the MFPC strategy.

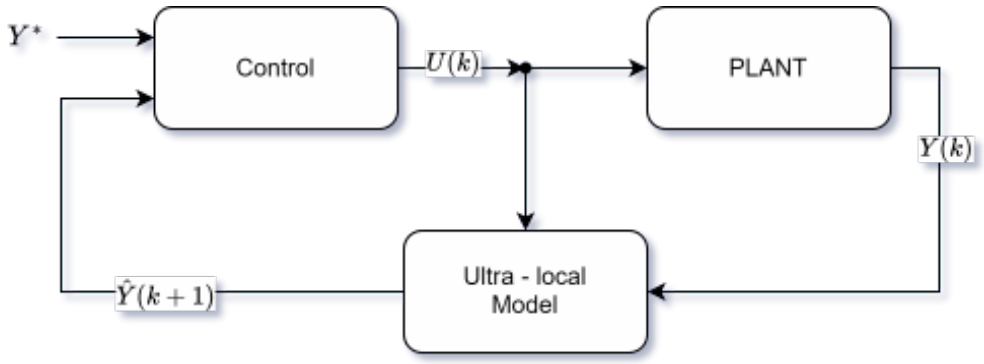


Figure 14: Model-Free Predictive control block diagram

The signal flow requires that the controller receiving the reference Y^* and, at each sampling instant, selecting the actuation $U(k)$ to apply. This is imposed on the system, whose measured output $Y(k)$ is not returned to the controller, but rather to the ultra-local model block, which in turn receives the applied actuation. Starting from these two quantities, the block produces the one-step prediction $\hat{Y}(k+1)$, which closes the loop on the controller and constitutes the quantity actually compared with the reference in the cost function [29].

The ultra-local model ignores the physics of the system being controlled and

describes only the relationship between inputs and outputs, according to the relationship:

$$\begin{cases} i_d(k+1) = i_d(k) + T_s(\alpha_d\, u_d(k) + F_d(k)) \\ i_q(k+1) = i_q(k) + T_s\big(\alpha_q\, u_q(k) + F_q(k)\big) \end{cases} \tag{141}$$

α is defined as a scale factor typically inizialized as $\frac{1}{L}$ [30], while $\hat{F}$ is a term that captures all the uncertainties of the system, such as resistance, which varies with temperature, magnetic coupling, or parametric errors.

The system has four unknowns, as highlighted by eq. (141), but there are only two equations. The numerical solution is to exploit the nature of the FCS (finite control set) structure already seen in MPC control section 4.3, and by exploiting the null vectors V_0 and V_7, eq. (141) are simplified to the form:

$$i_{dq}(k+1) = i_{dq}(k) + T_s F_{dq}(k) \quad \Longrightarrow \quad F_{dq}(k) = \frac{i_{dq}(k+1) - i_{dq}(k)}{T_s} \tag{142}$$

This allows us to derive the unknown $\hat{F}$ on the d-axis and q-axis. Assuming that $\hat{F}$ remains stable for several control cycles, and therefore assuming this term is known, using the non null vectors $V_{1\ldots6}$, the equation can be inverted to estimate the value of α.

$$\alpha_{dq} = \frac{\dfrac{\Delta i_{dq}}{T_s} - \hat{F}_{dq}(k)}{u_{dq}(k)}, \qquad \Delta i_{dq} = i_{dq}(k+1) - i_{dq}(k) \tag{143}$$

This method is affected by noise, amplifying the current measurement error [29]. For that reason the RLS (recursive least square) method is introduced.
The RLS method starts from the linear formulation of the parameter model, that is, an equation where the measured output of the system can be expressed as a scalar product between a data vector and a vector of unknown coefficients.

$$y(k) = \varphi^T(k)\theta + e(k) \tag{144}$$

Where $y(k)$ is the output measurement, that is, the current, $\varphi(k)$ is the regressor that collects past current and voltage samples, and θ is the vector of unknown parameters to be estimated. The error $e(k)$ is the residual due to measurement errors and additional unmodeled dynamics. It is linearity with respect to the θ parameters that makes the method applicable. The optimum parameter to be identified is the estimate that minimizes the weighted sum of the squares of the errors committed on the data collected up to the current time.

$$J(\theta,k) = \sum_{j=1}^{k} \lambda^{k-j} \left[y(j) - \varphi^{\mathsf{T}}(j)\theta \right]^2, \qquad 0 < \lambda \leq 1 \tag{145}$$

Differentiating the estimate with respect to the parameters θ and setting it equal to zero:

$$\frac{\partial J}{\partial \theta} = -2 \sum_{j=1}^{k} \lambda^{k-j} \varphi(j) \left[y(j) - \varphi^{\mathsf{T}}(j)\theta \right] = 0, \tag{146}$$

And by separating the terms containing the unknown from the terms containing the data, we obtain:

$$\underbrace{\left[\sum_{j=1}^{k} \lambda^{k-j} \varphi(j)\varphi^{\mathsf{T}}(j) \right]}_{R(k)} \hat{\theta}(k) = \underbrace{\sum_{j=1}^{k} \lambda^{k-j} \varphi(j)\, y(j)}_{f(k)}. \tag{147}$$

Therefore, the system can be viewed as a linear system of the form,

$$R(k)\hat{\theta}(k) = f(k) \tag{148}$$

with a solution equal to:

$$\hat{\theta}(k) = R^{-1}(k) f(k) \tag{149}$$

which formally solves the parameter identification problem.

The issue with the method is that the terms $R(k)$ and $f(k)$ are sums that encompass all the past terms of the system, which should be preserved, and in a system to be used in real time, this is not practical. To resolve this issue in the formulation, it is sufficient to

operate algebraically, isolating the term with $j = k$ of the equation eq. (147).

$$R(k) = \sum_{j=1}^{k-1} \lambda^{k-j} \varphi(j) \varphi^{\mathsf{T}}(j) \; + \; \varphi(k) \varphi^{\mathsf{T}}(k) \tag{150}$$

Decomposing the exponent:

$$\lambda^{k-j} = \lambda^{1+[(k-1)-j]} = \lambda \cdot \lambda^{(k-1)-j} \tag{151}$$

Collecting the λ factor:

$$\sum_{j=1}^{k-1} \lambda^{k-j} \varphi(j) \varphi^{\mathsf{T}}(j) = \lambda \sum_{j=1}^{k-1} \lambda^{(k-1)-j} \varphi(j) \varphi^{\mathsf{T}}(j) \tag{152}$$

which is by definition the information relating only to the inputs of the previous step

$$R(k-1) = \sum_{j=1}^{k-1} \lambda^{(k-1)-j} \varphi(j) \varphi^{\mathsf{T}}(j) \tag{153}$$

obtaining by substitution the recursive laws, both for the inputs $R(k)$ and for the outputs $f(k)$:

$$R(k) = \lambda R(k-1) + \varphi(k) \varphi^{\mathsf{T}}(k) \tag{154}$$

$$f(k) = \lambda f(k-1) + \varphi(k)\, y(k) \tag{155}$$

The solution requires R^{-1} and not $R(k)$, so we need to find a recurrence that avoids matrix inversion. Then, at the operational level, we introduce the covariance matrix $P(k)$, defined as:

$$P(k) = R(k)^{-1} \tag{156}$$

Which represents the uncertainty in the parameter estimate.
The key to understanding the meaning of $P(k)$ lies in the form of the added term $\varphi\varphi^{\mathsf{T}}$, which is the exterior product of a vector by itself, which in physics terms means that the new data provides information along only one direction of the parameter space, namely

the direction indicated by the current regressor. If a vector moves along only one direction, it is reasonable to think that its inverse behaves in the same way, and this is precisely what the Sherman and Morrison lemma expresses. [31]

$$\left(A+uv^{\mathsf{T}}\right)^{-1} = A^{-1} - \frac{A^{-1}uv^{\mathsf{T}}A^{-1}}{1+v^{\mathsf{T}}A^{-1}u}. \tag{157}$$

applying the lemma 157 with $A = \lambda R(k-1)$ and $u = v = \varphi(k)$, and recalling that $A^{-1} = \lambda^{-1}P(k-1)$, we obtain

$$P(k) = \frac{1}{\lambda}P(k-1) - \frac{\frac{1}{\lambda}P(k-1)\varphi(k)\,\varphi^{\mathsf{T}}(k)\frac{1}{\lambda}P(k-1)}{1+\frac{1}{\lambda}\varphi^{\mathsf{T}}(k)P(k-1)\varphi(k)}, \tag{158}$$

Simplifying the λ terms:

$$P(k) = \frac{1}{\lambda}\left[P(k-1) - \frac{P(k-1)\varphi(k)\,\varphi^{\mathsf{T}}(k)P(k-1)}{\lambda+\varphi^{\mathsf{T}}(k)P(k-1)\varphi(k)}\right]. \tag{159}$$

and introducing the adaptive gain which by definition is:

$$G(k) = \frac{P(k-1)\,\varphi(k)}{\lambda+\varphi^{\mathsf{T}}(k)\,P(k-1)\,\varphi(k)} \tag{160}$$

Substituting it, the covariance expression $P(k)$ becomes

$$P(k) = \frac{1}{\lambda}\left[P(k-1) - G(k)\,\varphi^{\mathsf{T}}(k)\,P(k-1)\right] \tag{161}$$

rewriting the normal equations eq. (147), with the covariance $P(k)$, and replacing $f(k)$ with the recursive form:

$$\hat{\theta}(k) = P(k)\left[\lambda f(k-1) + \varphi(k)\,y(k)\right] \tag{162}$$

From previous consideration can be obtained that $f(k-1) = R(k-1)\theta(k-1)$, $\lambda R(k-1) = R(k) - \varphi\varphi^{T}$, and by definition $P(k)R(k) = I$ with $P(k)\varphi$ equal to $G(k)$, can be ob-

tained the final parametric update formula:

$$\hat{\theta}(k) = \hat{\theta}(k-1) + G(k)\, e(k) \tag{163}$$

In addition to the final equation that represents the estimation of the parameters, it is necessary to give a small, non-trivial example, which includes two parameters $\theta = [2,3]^T$, which the algorithm does not know and must identify by observing the output of the linear equation:

$$y(k) = \varphi^{\mathsf{T}}(k)\, \theta. \tag{164}$$

The starting situation, shown in Fig. 15, is fixed by the initialization:

$$\hat{\theta}(0) = \begin{bmatrix} 0 \\ \\ 0 \end{bmatrix}, \qquad P(0) = 100 I_2. \tag{165}$$

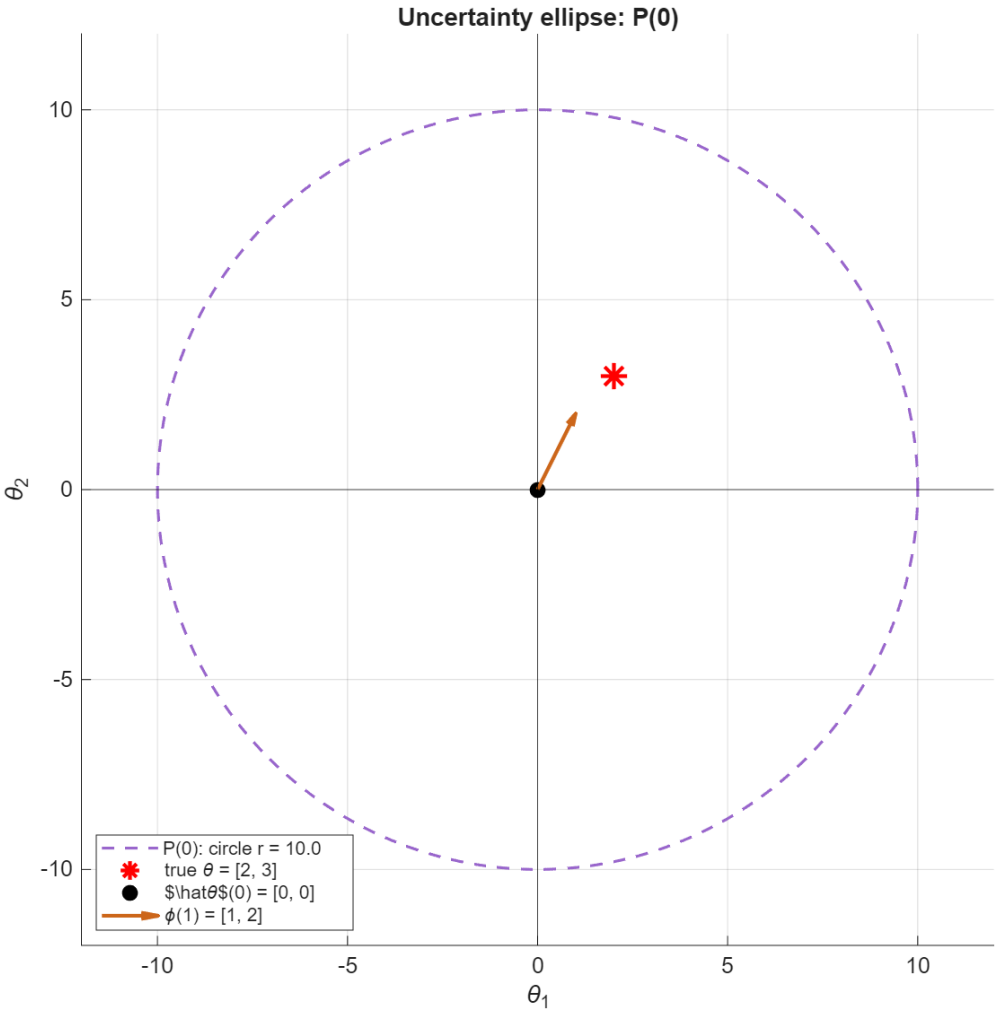


Figure 15: RLS - Step 0

the eigenvalues of $P(0)$ coincide, so the ellipse degenerates into a circle of radius $\sqrt{100}$ centred at the origin.

With $\varphi(1) = [1,\ 2]^{\mathsf{T}}$, which corresponds to $y(1) = 8$, the a priori error holds

$$e(1) = y(1) - \varphi^{\mathsf{T}}(1)\hat{\theta}(0) = 8 - 0 = 8, \tag{166}$$

the adaptive gain (160) results

$$G(1) = \frac{P(0)\varphi(1)}{\lambda + \varphi^{\mathsf{T}}(1)P(0)\varphi(1)} = \frac{1}{1+500}\begin{bmatrix}100\\200\end{bmatrix} = \begin{bmatrix}0{,}1996\\0{,}3992\end{bmatrix}, \tag{167}$$

and the update (163) leads to

$$\hat{\theta}(1) = \hat{\theta}(0) + G(1)e(1) = \begin{bmatrix} 1{,}5968 \\ 3{,}1936 \end{bmatrix}. \tag{168}$$

The estimation moves exactly along $\varphi(1)$, since the direction of the normalized correction coincides digit by digit with $\varphi(1)/\|\varphi(1)\|$: with P isotropic the gain is in fact reduced to $G \propto \varphi$. The covariance update (161) yields

$$P(1) = \frac{1}{\lambda}\left[I - G(1)\varphi^{\mathsf{T}}(1)\right]P(0) = \begin{bmatrix} 80{,}04 & -39{,}92 \\ -39{,}92 & 20{,}16 \end{bmatrix}, \tag{169}$$

whose eigenvalues are 0,1996 and 100, with eigenvectors aligned and orthogonal to the regressor, respectively.

The circumference has therefore flattened into a very elongated ellipse, with semi-axis 0,447 along $\varphi(1)$ and semi-axis still equal to 10 in the orthogonal direction, as shown in Fig. 16.

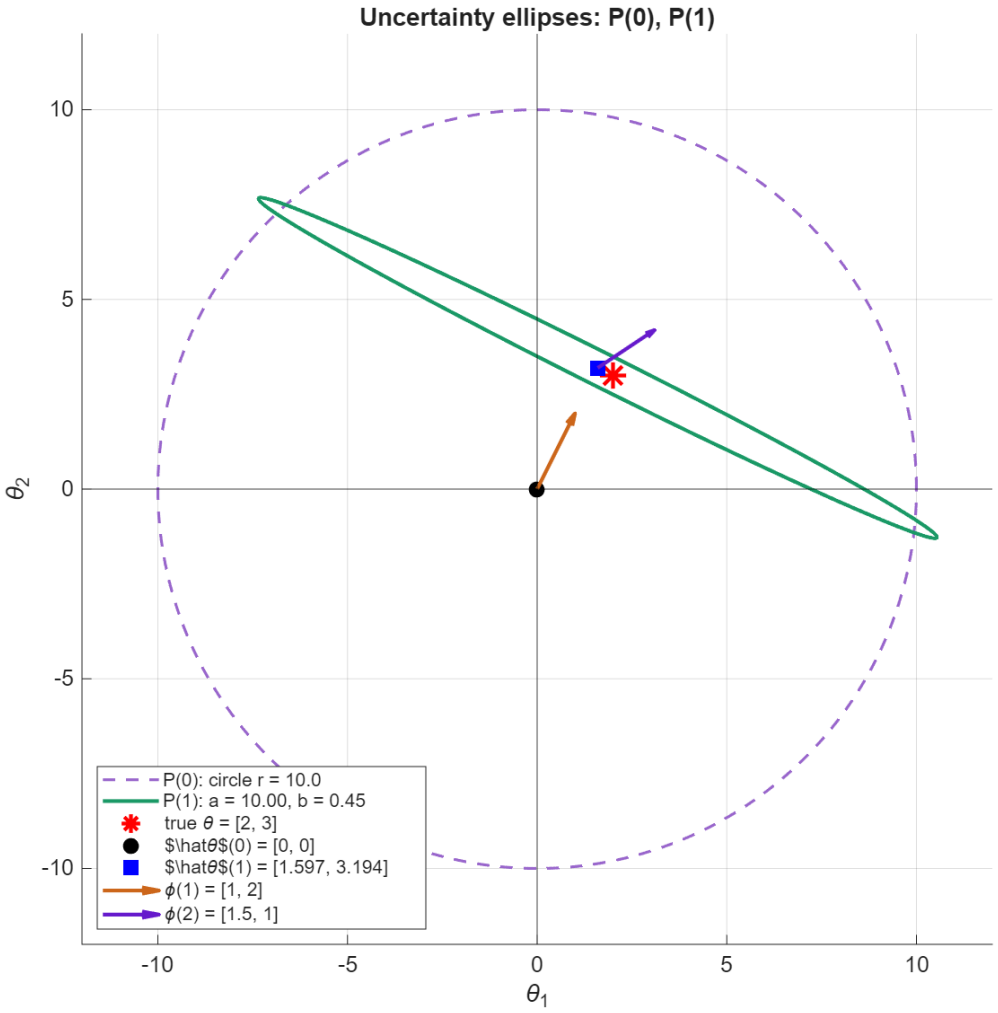


Figure 16: RLS - Step 1

With $\varphi(2) = [1{,}5,\ 1]^{\mathsf{T}}$ and $y(2) = 6$ the error drops to

$$e(2) = y(2) - \varphi^{\mathsf{T}}(2)\hat{\theta}(1) = 6 - 5{,}5888 = 0{,}4112, \tag{170}$$

a value much lower than the initial one since much of the information is already acquired. The gain becomes

$$G(2) = \frac{P(1)\varphi(2)}{\lambda + \varphi^{\mathsf{T}}(2)P(1)\varphi(2)} = \frac{1}{1+80{,}49}\begin{bmatrix} 80{,}14 \\ -39{,}72 \end{bmatrix} = \begin{bmatrix} 0{,}9834 \\ -0{,}4874 \end{bmatrix}, \tag{171}$$

and the direction of the correction is $[0{,}896, -0{,}444]$, which does not coincide with $\varphi(2)/\|\varphi(2)\| = [0{,}832, 0{,}555]$ but rather with the major axis of $P(1)$. The algorithm

therefore moves almost entirely along the still uncertain direction, leaving what has already been learned almost intact: this confirms that in the product $P(k-1)\varphi(k)$ the gain represents the direction of the regressor distorted by the covariance and not the regressor itself. The estimate reaches

$$\hat{\theta}(2) = \hat{\theta}(1) + G(2)e(2) = \begin{bmatrix} 2{,}0012 \\ 2{,}9932 \end{bmatrix}, \tag{172}$$

with final semi-axes reduced to 1,377 and 0,359, as illustrated in Fig. 17: two linearly independent regressors have saturated both directions of a two-dimensional space, satisfying the persistent excitation condition.

The residual error, on the order of a few thousandths, constitutes the last trace of the initial condition $\hat{\theta}(0) = \mathbf{0}$, which acts like fictitious a priori information and is forgotten only asymptotically.

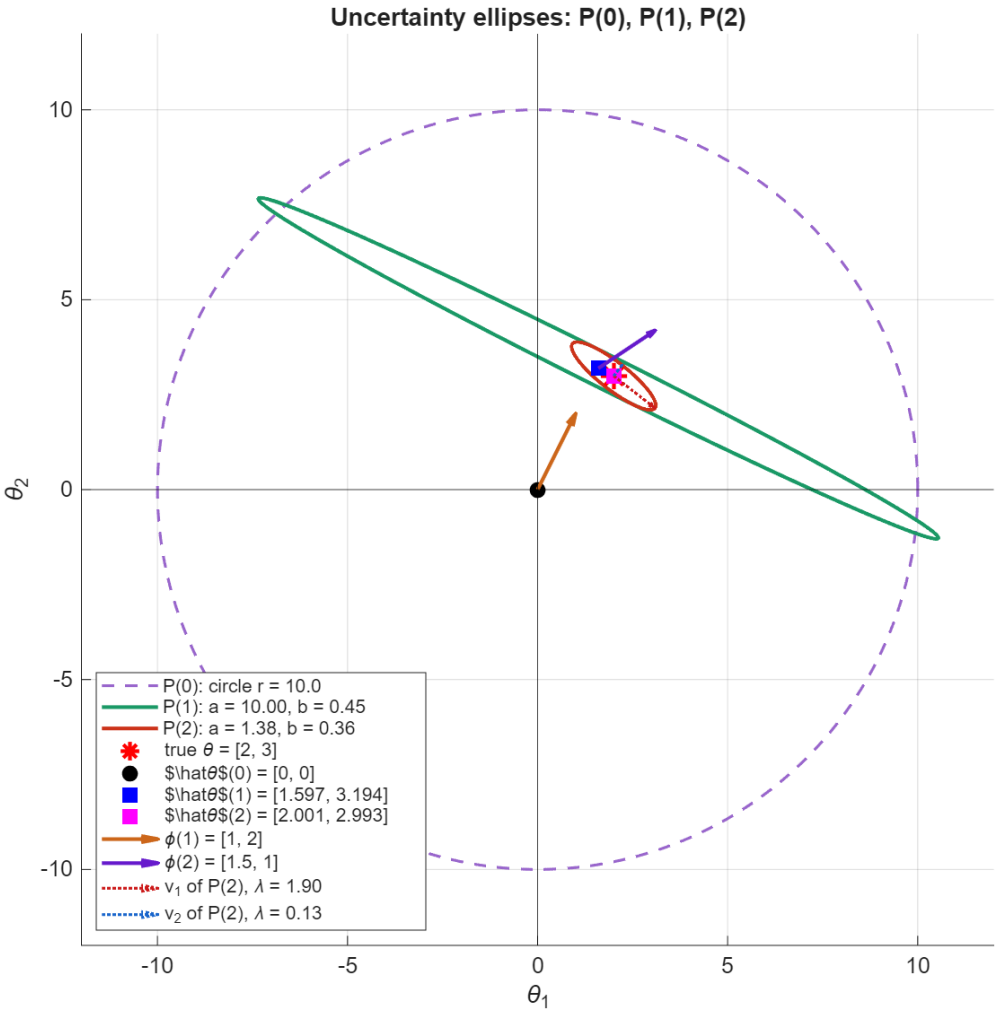


Figure 17: RLS - Step 2

Once the recursive algorithm RLS has returned the parameter vector $\hat{\theta}_{dq}(k)$, these are used within the ultra-local model, which requires the scale factor and the uncertain term separately. Since the estimate provides the input-output relationship coefficients as a whole, the uncertain term is extracted by difference, subtracting the contribution of the voltage applied in the previous step.

$$\hat{F}_d(k) = \varphi_d^{\mathsf{T}}(k)\,\hat{\theta}_d(k) - \alpha_d\, v_d(k-1), \qquad \hat{F}_q(k) = \varphi_q^{\mathsf{T}}(k)\,\hat{\theta}_q(k) - \alpha_q\, v_q(k-1), \tag{173}$$

in which α_d and α_q are assumed to be equal to the inverses of the nominal direct and quadrature -axis inductances and are not updated, while $v_d(k-1)$ and $v_q(k-1)$ were the optimum in the previous sampling period.

With these components, we evaluate, for each candidate, the current that would be ob-

tained by applying the corresponding vector, according to the prediction law of the ultra-local model.

$$i_d^p(k+1,n) = i_d(k) + T_s\left[\alpha_d\, v_d(n) + \hat{F}_d(k)\right], \tag{174}$$

$$i_q^p(k+1,n) = i_q(k) + T_s\left[\alpha_q\, v_q(n) + \hat{F}_q(k)\right]. \tag{175}$$

The predictions thus obtained are compared with the current references using the cost function, assumed equal to the Euclidean norm of the error,

$$g(n) = \sqrt{\left(i_d^* - i_d^p(k+1,n)\right)^2 + \left(i_q^* - i_q^p(k+1,n)\right)^2}, \tag{176}$$

and the optimal vector is identified as the one that minimizes it,

$$n_{\text{opt}} = \arg \min_{n\in\{0,\ldots,7\}} g(n), \tag{177}$$

which is then applied to the inverter in the next period. The voltage v_d^{opt} and v_q^{opt} are stored together with the measured currents, since they constitute elements of the regressor that the estimation algorithm will use in the next step. This is the point where the loop is closed, the controller's output becoming the estimator's input.

4.5 INDI Control

The idea of introducing this latter control strategy arose from the investigation of methods used in other fields of engineering. Non-linear dynamic inversion and its incremental variants have been very successful in flight control: the F-35 is the first production fighter to incorporate a dynamic inversion control law over the whole flight envelope [32].

The system's non-linearities are cancelled using a feedback control law for a non-linear plant, an idea developed for multivariable systems in the late 1960s and early 1970s [33]. Its control-oriented formulation, now known as feedback linearization or non-linear dynamic inversion (NDI), has become established in the non-linear control literature [34].

A system is said to be affine in control when the input u appears linearly, while

the dependence on the state x remains non-linear. Consider therefore a plant written in input-affine form

$$\dot{x} = f(x) + G(x)\,u, \qquad y = h(x), \tag{178}$$

with $x \in \mathbb{R}^n$ the state vector, $u \in \mathbb{R}^m$ the vector of control inputs, and $y \in \mathbb{R}^p$ the vector of measured outputs. Observing the structure of (178), we note that the right-hand side is a first-degree polynomial in u: it contains a term independent of the input, $f(x)$, and a multiplicative term, $G(x)\,u$. Terms of the type u^2, $\sin(u)$, or cross products $u_i u_j$ are not allowed. Hence the affine name, analogous to the straight line $z = m\xi + q$, where, however, the coefficients q and m vary with the operating point.

$f(x)$ **drift field.** Describes the autonomous evolution of the system, that is, the dynamics observed in the absence of any control action ($u = 0$). It includes the internal couplings, the dissipative terms, and, in general, all the non-linearities of the state. The point x_e such that $f(x_e) = 0$ constitutes an unforced equilibrium of the system.

$G(x)$ **matrix of input fields.** Its columns $g_1(x), \ldots, g_m(x)$ represent the directions in the state space along which each input is able to act:

$$G(x)\,u = \sum_{i=1}^{m} g_i(x)\,u_i. \tag{179}$$

The essential aspect is that these directions depend on the state: the same command produces different effects at different operating points.

$h(x)$ **output map.** It defines the quantities actually available for measurement, generally non-linear functions of the state. In (178) the output does not explicitly depend on u, a hypothesis that excludes the direct transmission term and guarantees non-zero relative degree with respect to each input.

When f, G, and h do not explicitly depend on time, the system is said to be time-invariant; the case $f(x) = Ax$, $G(x) = B$, and $h(x) = Cx$ brings (178) back to the classical linear model, which therefore represents a special case of it.

This structure has a direct consequence for control design. Since u enters linearly, its effect on the state is described by a coefficient depending on x alone, and this

property is preserved when the equations are manipulated. The output, on the other hand, does not depend on the input directly: $y = h(x)$ is a function of the state only. To make the input appear, the output must be differentiated along the dynamics, once or more; when the input finally shows up, it still does so linearly, so the resulting expression can be solved for u by algebraic inversion. This is the idea behind non-linear dynamic inversion: rather than approximating the plant around an operating point, the input is chosen so as to cancel the non-linear terms exactly, leaving a linear relation between the output and a new, artificial input.

Let r be the relative degree of the output, that is, the number of times y must be differentiated before the input appears explicitly.
That derivative can then be expressed as

$$y^{(r)} = a_\nu(x) + B_\nu(x)\, u \triangleq \nu, \tag{180}$$

where ν is called the pseudo control and B_ν the control effectiveness. In the multivariable case each output has its own relative degree r_i, the set $\{r_1, \ldots, r_m\}$ being the vector relative degree, and $B_\nu(x)$ becomes the decoupling matrix of the plant. Provided B_ν is invertible, solving (180) for the input gives the inversion law

$$u_{\text{cmd}} = B_\nu^{-1}(x)\left[\nu_{\text{des}} - a_\nu(x)\right], \tag{181}$$

which cancels every non-linearity and leaves the linear relation $y^{(r)} = \nu_{\text{des}}$.

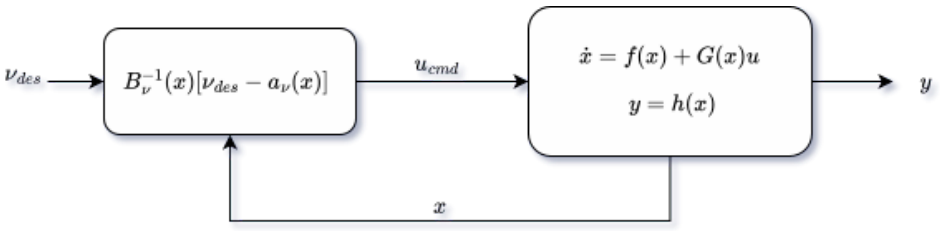


Figure 18: Non-linear dynamic inversion as a static state feedback, adapted from [34]

In the rotor reference frame the stator voltage balance of the synchronous reluc-

tance machine derived in Chapter 3.1 reads

$$\begin{bmatrix} v_d \\ v_q \end{bmatrix} = R_s \begin{bmatrix} i_d \\ i_q \end{bmatrix} + \frac{\mathrm{d}}{\mathrm{d}t} \begin{bmatrix} \psi_d \\ \psi_q \end{bmatrix} + \omega_e \begin{bmatrix} -\psi_q \\ \psi_d \end{bmatrix}, \tag{182}$$

and, introducing the incremental inductance matrix

$$L(i) = \frac{\partial \psi}{\partial i} = \begin{bmatrix} L_{dd} & L_{dq} \\ L_{qd} & L_{qq} \end{bmatrix}, \qquad \frac{\mathrm{d}\psi}{\mathrm{d}t} = L(i)\,\dot{i}, \tag{183}$$

the current dynamics take the form (178) with state and input $x = [\,i_d \;\; i_q\,]^\top$, $u = [\,v_d \;\; v_q\,]^\top$:

$$\dot{i} = \underbrace{-L^{-1}\left(R_s i + \omega_e \begin{bmatrix} -\psi_q \\ \psi_d \end{bmatrix} \right)}_{a_\nu(x)} + \underbrace{L^{-1}}_{B_\nu(x)} \nu. \tag{184}$$

The controlled output is the current vector itself, so that $r = 1$ on both axes and the pseudo control is the current derivative, $\nu = \dot{i}$. The control effectiveness is the inverse of the incremental inductance matrix, and its invertibility requires $\det L(i) \neq 0$. Substituting (184) into (181) gives

$$v_{\mathrm{cmd}} = R_s i + \omega_e \begin{bmatrix} -\psi_q \\ \psi_d \end{bmatrix} + L(i)\,\nu_{\mathrm{des}}, \tag{185}$$

which is exactly the voltage decoupling network of the field-oriented scheme of Chapter 3.1. Its weakness is equally apparent: every term of a_ν must be known accurately, while R_s drifts with winding temperature and the flux linkages are saturated and cross-saturated functions affected by the uncertainty of the identification.

The incremental formulation removes that dependence. Let u_0 be the input applied at the previous sampling instant and ν_0 the corresponding pseudo control, so that $\nu_0 = a_\nu(x_0) + B_\nu(x_0)u_0$. Writing the same balance for the desired pseudo control and sub-

tracting the two expressions, the state-dependent term $a_\nu(x_0)$ cancels and there remains

$$\nu_{\text{des}} - \nu_0 = B_\nu(x_0)\,(u_{\text{cmd}} - u_0)\,, \tag{186}$$

whence the incremental inversion law

$$u_{\text{cmd}} = u_0 + B_\nu^{-1}(x_0)\,(\nu_{\text{des}} - \nu_0)\,. \tag{187}$$

Both terms of the subtraction are evaluated at x_0, so the cancellation is exact only to the extent that $a_\nu(x) \simeq a_\nu(x_0)$ and $B_\nu(x) \simeq B_\nu(x_0)$ over one sampling period. This time scale separation between the state evolution and the control update is the assumption on which the whole incremental formulation rests, and it ties the validity of the method directly to the sampling frequency. Only the control effectiveness survives: the resistive drop and the speed-dependent terms no longer appear, and are instead accounted for implicitly by the applied input u_0 and by the measured plant response ν_0. Equation (187) requires the current derivative, which no transducer of the drive provides and which cannot be obtained by numerical differentiation of the sampled currents without amplifying the switching ripple. It is therefore estimated by blending an on-board model of the machine with the measurement,

$$\hat{\dot{i}} = \dot{i}_{\text{OBM}} + K_{\text{aug}}\left(\dot{i}_0 - \dot{i}_{\text{OBM}}\right) = \left(1 - K_{\text{aug}}\right)\dot{i}_{\text{OBM}} + K_{\text{aug}}\,\dot{i}_0, \tag{188}$$

where $\dot{i}_{\text{OBM}}$ is evaluated from (184) at the measured operating point and the correction term is low-pass filtered with cut-off frequency f_{cut}. The augmentation gain K_{aug} is a linear weight between the two sources: the model estimate is smooth but biased by parameter error, the measured one is unbiased but noisy, and the blend trades one against the other. It should be noted that the on-board model reintroduces the very quantities the incremental formulation had removed, since $\dot{i}_{\text{OBM}}$ is computed from R_s and from the flux linkages: the parameter error re-enters the loop weighted by $\left(1 - K_{\text{aug}}\right)$, and full independence from the machine parameters is recovered only in the limit $K_{\text{aug}} \to 1$, at the cost of the measurement noise. The choice of K_{aug} is therefore a compromise between parameter sensitivity and noise rejection.

Substituting $B_v^{-1} = L(i)$ and $\Delta\dot{i} = \dot{i}_{\text{des}} - \hat{\dot{i}}$ into (187), the law implemented on the two axes reads

$$v_{d,\text{cmd}} = v_{d,0} + L_{dd}\,\Delta\dot{i}_d + L_{dq}\,\Delta\dot{i}_q, \tag{189}$$

$$v_{q,\text{cmd}} = v_{q,0} + L_{qd}\,\Delta\dot{i}_d + L_{qq}\,\Delta\dot{i}_q, \tag{190}$$

where $v_{d,0}$ and $v_{q,0}$ are retained by a unit delay of period T_s in the feedback branch. The off-diagonal terms couple the two channels: omitting them would leave the cross-saturation contribution uncompensated. The desired pseudo control is produced by a first-order reference model,

$$\dot{i}_{\text{des}} = \omega_c\,(i_{\text{ref}} - i)\,, \tag{191}$$

the forward derivative of the reference being zero, since the current references generated by the MTPA and field-weakening strategy are piecewise constant. Combining (191) with the linearized closed loop $\dot{i} = \dot{i}_{\text{des}}$ yields

$$\frac{i(s)}{i_{\text{ref}}(s)} = \frac{\omega_c}{s + \omega_c}, \tag{192}$$

a first-order response whose bandwidth is set directly by ω_c and does not depend on L_{dd}, L_{qq} or R_s. This is the practical advantage of the method: the same bandwidth can be assigned to both axes despite the anisotropy of the machine, without computing gains from the machine parameters.

5 Simulation

For each of the four control strategies analyzed, the block diagram representing the implementation and the results obtained from the simulations conducted according to the reference scenario will be presented. In particular, for each model the following will be reported:

- the currents i_d and i_q, compared between the reference value and the measured value;
- the mechanical speed ω_m, compared between the reference value and the measured value;
- the plane i_d–i_q, with the operating point trajectory superimposed on the characteristic curves (MTPA, voltage ellipse, limit current circle);
- the phase currents i_{abc};
- the phase voltages v_{abc}.

This set of graphs, common to all four strategies, allows a direct and systematic comparison of performance. For each model, additional graphs are added to analyze parameters specific to the specific control strategy. To ensure a valid comparison between the four simulations analyzed in this thesis: PI, INDI, FCS-MPC, and MFPC, a single reference scenario is used. The velocity profile ω_{ref} imposes four successive steps (158, 220, 240, and 260 rad/s) at $t = 0, 1, 2, 3$ s, while the load torque profile T_{load} follows a more complex pattern, with transitions at $t = 0.25, 0.5, 0.75, 1, 2, 2.5, 3$ and 4 s, up to a maximum of 5 Nm. Using a single reference pair for all four simulations eliminates any confounding variables related to the operating scenario, thus isolating performance differences (following error, ripple, robustness) to the intrinsic characteristics of each control algorithm.

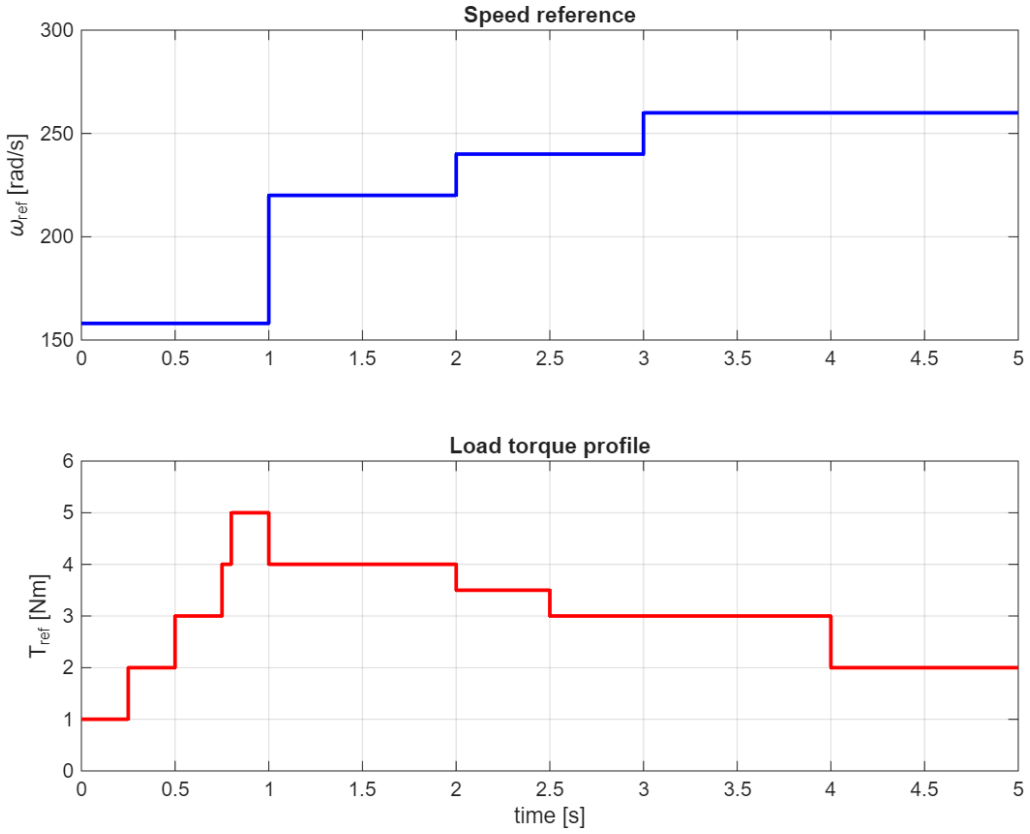


Figure 19: Speed reference and Load torque profile

5.1 PI model simulation

The first proposed model implements the field-oriented control (FOC) scheme with PI regulators to control the motion of the SynRM motor through a three-phase inverter with two voltage levels.

The generic scheme can be considered as a set of three interconnected macrogroups: the external speed loop, the internal current loop, and the system to be controlled.

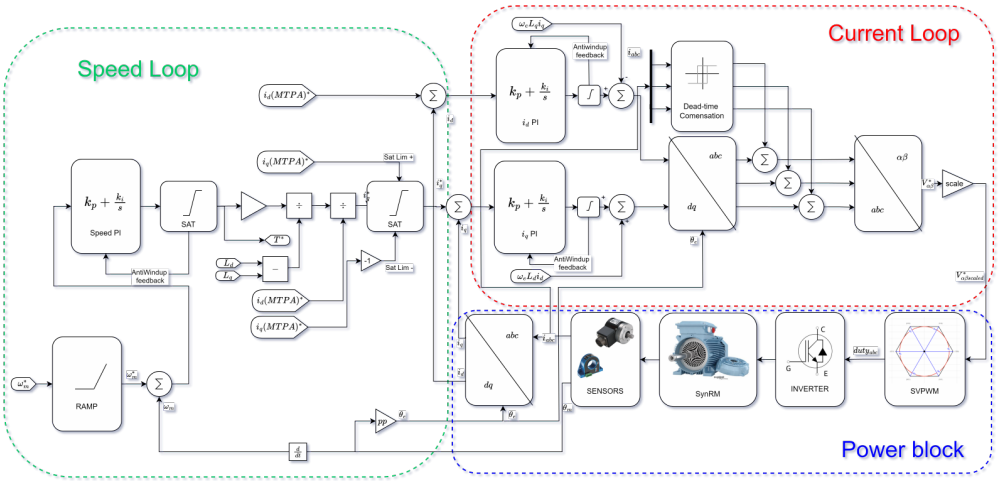


Figure 20: Block diagram of the PI model proposed for SynRM drives

The external speed loop takes the speed reference provided by the profile generator. The ramp block processes the requested speed reference signal to provide at the downstream PI controller a smoother reference, avoiding sudden changes that could cause system oscillations. The ramp generates a reference that takes one second to reach the nominal speed of the SynRM motor. The generated reference is compared by the summing block to the speed feedback read by a dedicated sensor keyed on the motor shaft. The error between the two signals is sent to the input of the speed controller. The PI controller, according to the structure, section 4.1.3, generates the torque reference required to accelerate the motor to the required speed and balance the load torque required by the profile generator. The torque reference, once processed with appropriate scaling, generates the required current reference i_q^*:

$$T_m^* = \frac{3}{2} pp(L_d - L_q) i_d^* i_q^* \tag{193}$$

obtaining:

$$i_q^* = \frac{T_m^*}{\frac{3}{2} pp(L_d - L_q) i_d^*} \tag{194}$$

The generated torque current reference i_q^* is limited upper and lower by the value generated by the reference generator function i_d^* and i_q^*, called in the simulation "MTPA FW MTPV SOLVER". The saturated torque current reference is compared via a summing

node to the appropriately transformed current feedback in the dq frame. The error between the reference and the measured current value on the quadrature axis is sent to the input of the PI regulator. In parallel with this regulator, there is a second PI regulator for the direct axis. The regulators discussed so far feature a saturator structure and anti-windup mechanism [35]; the diagram below shows the implementation.

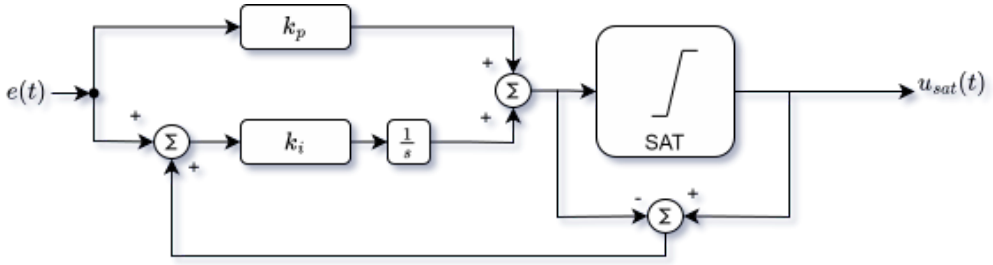


Figure 21: PI control detail

More sophisticated and high-performance anti-windup schemes exist, but I chose to keep the implementation simple for the first model. Although simple to implement, the saturator and anti-windup scheme allows for output limitation and prevents control instability. In the event of a saturated loop, the integrator would continue to operate, so the anti-windup mechanism corrects the regulator's behavior.

The regulator gains are computed from (131) by imposing a damping factor $\zeta = 0.707$ and a natural frequency $f_i = 1$ kHz on both axes [11]. With a sampling and modulation frequency of 20 kHz, the current loop remains one decade above the speed loop and well below the sampling frequency. The voltage references in the dq plane are then added to the decoupling network, recalling the motor equations:

$$e_d = -\omega_e L_q i_q \tag{195}$$

$$e_q = +\omega_e L_d i_d \tag{196}$$

They must be added to the voltage references crosswise with respect to the axis voltage. The result of this step generates the voltage references u_d^* and u_q^*.

These are transformed into the natural frame abc to allow for dead-time corrections. The function of dead-time compensation calculates the three correction voltages in the natural frame to be added to the three references V_a^*, V_b^*, and V_c^*, to compensate for the voltage

error introduced by the dead time inserted between the switching of the two switches on each leg of the inverter. During the dead time interval T_d, both IGBTs on one leg are off, and the phase current closes through the freewheeling diodes. The phase potential in this interval is not determined by the gate signals, but exclusively by the direction of the phase current. If $i_{phase} > 0$ the outgoing current conducts, and the node remains locked to the negative potential; consequently, the actual voltage is lower than the commanded voltage; If $i_{phase} < 0$ the incoming current conducts, and the upper diode remains locked to the positive potential; consequently, the actual voltage is higher than the commanded voltage. The voltage error is equal to:

$$\Delta V = \frac{T_d}{T_s} * V_{dc} * sign(i) \tag{197}$$

The references thus corrected are transformed back into the $\alpha\beta$. The dead-time compensation implemented in this work follows the average-value feedforward approach, in which the compensation voltage is computed from the switching period, the dead time and the polarity of the phase currents [36].
The duties generated by the SVPWM method section 4.1.4, are then compared with a triangular reference signal to activate the appropriate switches via the appropriate gate signals. The feedback from the speed and current loops, after processing, is sent to the comparison summing nodes.
For the PI strategy discussed, the results are shown through a series of indicative graphs. The results obtained listed below refer to the scenario shown at the beginning of this chapter.

- the currents i_d and i_q, compare between the reference value generated by the MTPA algorithm and the value measured in the feedback;
- the mechanical speed ω_m, compare between the non ramped reference and the measured value;
- the plane i_d–i_q, with the operating point trajectory superimposed on the characteristic curves (MTPA locus, voltage ellipse and limit current circle);

- L_d and L_q computed by interpolation of the apparent inductances map;
- the phase currents i_{abc};
- the phase voltages v_{abc};
- I_s vector angle θ_{MTPA};
- Torque comparison.

The graph shows, for each axis of the dq reference, the comparison between the reference current generated by the MTPA algorithm and the measured value.
Tracking on both axes is accurate throughout the entire test profile. The measured value reaches the reference at each step with limited overshoot, and the steady-state error is reduced to only the switching ripple, without deviation.
During implementation, several issues related to reference tracking on the q axis were encountered. The tracking anomaly was caused by an error in the planning of the decoupling network; in fact, fixed inductance values were originally used throughout the test. The anomaly is visible in the graph below.

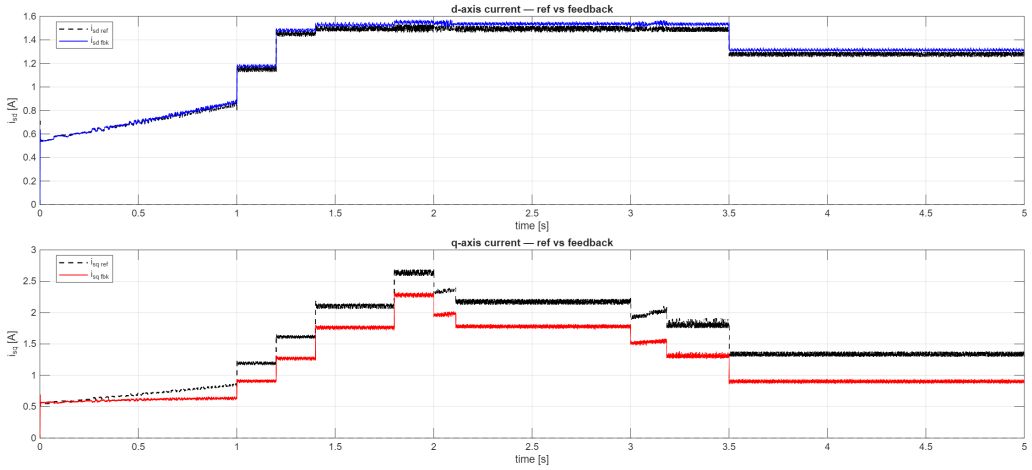


Figure 22: current in dq frame decoupling networ issue

To ensure effective operation of the network, it was necessary to use inductances obtained by interpolating the inductance maps. This behaviour further highlights the strong dependence on parameters in this control strategy.

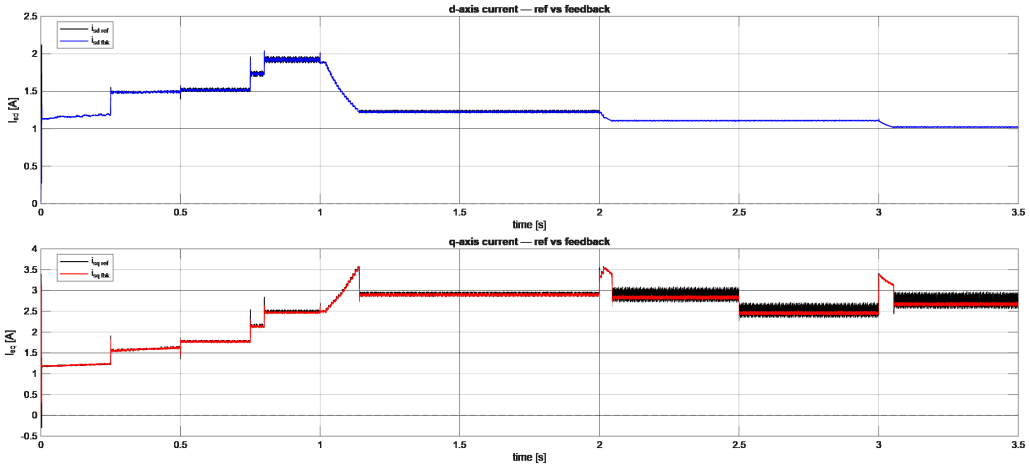


Figure 23: current in dq frame

The analysis of the results proceed by comparing the speed reference, taken before the ramp generator, with the value measured on the shaft. The deviation between the two traces during transients does not represent a tracking error, but the desired effect of the ramp block, which converts each step into a limited slope profile to avoid impulsive torque demands. At steady state, the measured speed coincides with the required value on all steps, with no residual error and no overshoot, confirming the correct dynamic separation between the outer and inner loop.

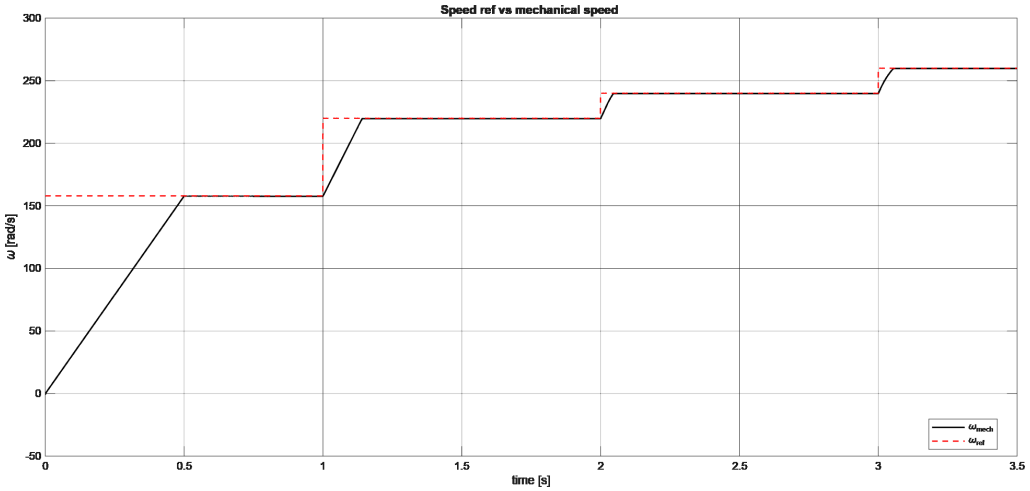


Figure 24: mechanical speed

The graph below, is the most representative of those shown, represents the trajectory of the operating point in the current plane dq, superimposed on the characteristic

curves of the machine, the theoretical trajectory of the MTPA, the current limit circumference and the voltage ellipses related to different speeds. The simulated trajectory is arranged along the minimum current points in the constant torque region and, when the base speed is exceeded, moves along the boundary imposed by the current and voltage constraints. The overlap between the operating point and the theoretical point confirms the consistency between the inductance maps used in the control and those used to plot the characteristic curves.

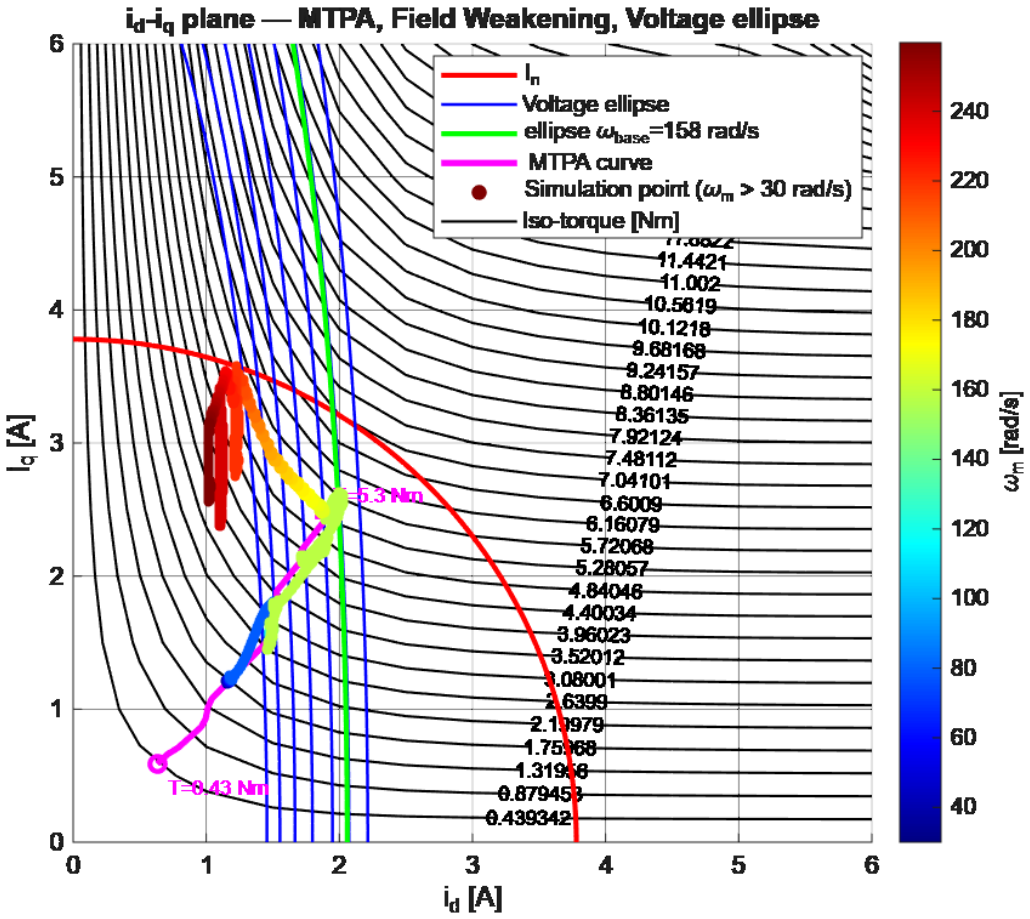


Figure 25: dq plane

The graph shows the values obtained by interpolating the apparent inductance maps at the operating point reached at each instant. Both quantities vary significantly along the test profile, as a direct consequence of magnetic saturation. This behaviour justifies the precise evaluation of the inductances adopted in the decoupling network and in the scaling network of the torque reference signal to the current reference on the q-axis.

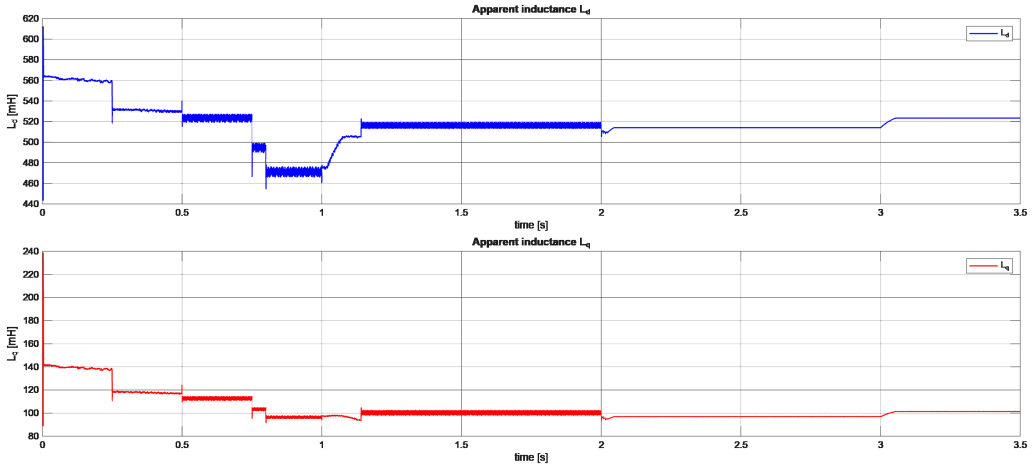


Figure 26: Interpolated L_d and L_q

The analysis proceed by checking the three-phase currents and voltages. The current graph allows us to evaluate the symmetry of the three-phase system, the harmonic content of the waveforms, and the amplitude of the switching ripple. Particular attention is paid to the zero-crossing regions, where the residual effects of the inverter's nonlinearity are evident, and to the transitions between the different operating points, where the variation in amplitude and frequency reflects the evolution of the torque and speed reference. The voltage graph, on the other hand, allows us to verify the correct exploitation of the available bus voltage and to identify the moment at which the voltage vector magnitude reaches the limit imposed by the DC bus, a condition that marks the entry into the field weakening region.

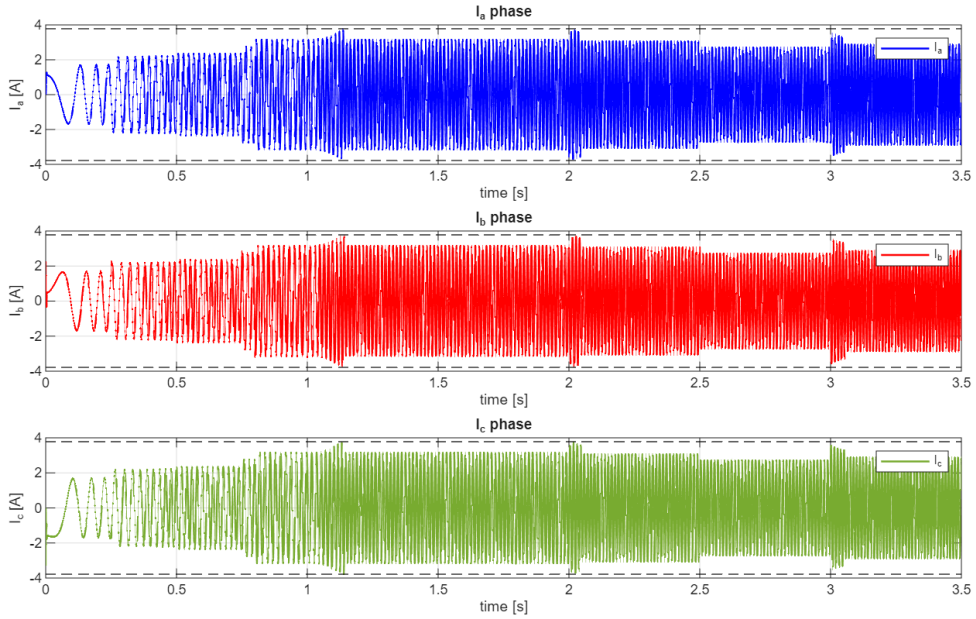


Figure 27: three phase current in natural frame abc

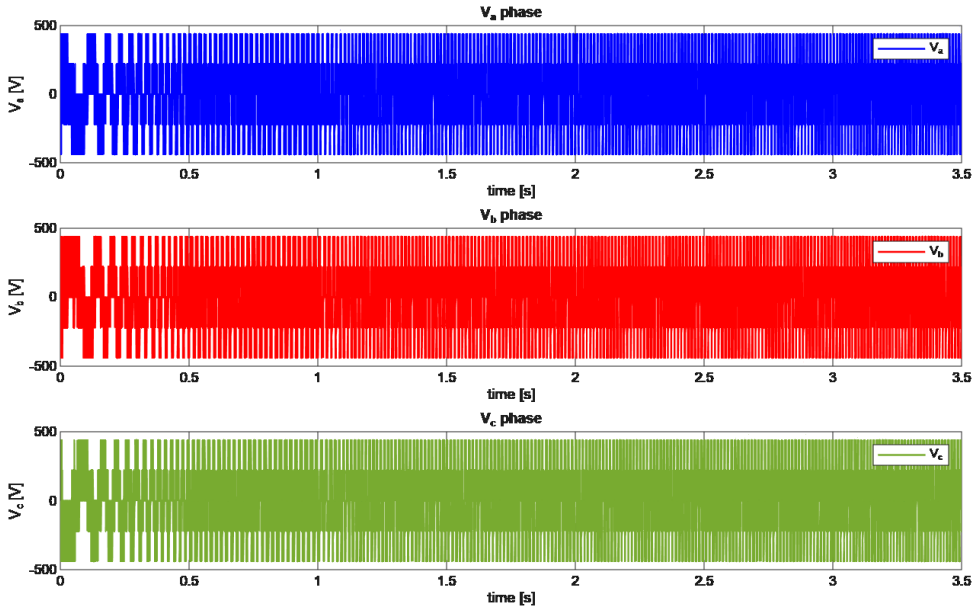


Figure 28: three phase voltege in natural frame abc

The graph shows the angle of the stator current vector in the dq frame, the angular position of the operating point along the trajectory shown in the $i_d i_q$ plane. In the constant-torque region, the angle takes the value that minimizes the current amplitude for

the required torque. Above the base speed, the angle increases, as the operating point leaves the MTPA locus and moves along the iso-torque curve, or along the limit current circumference if the required current vector exceeds this. Once a certain critical speed is exceeded, the angle remains fixed and the machine descends linearly toward the axes' origin.

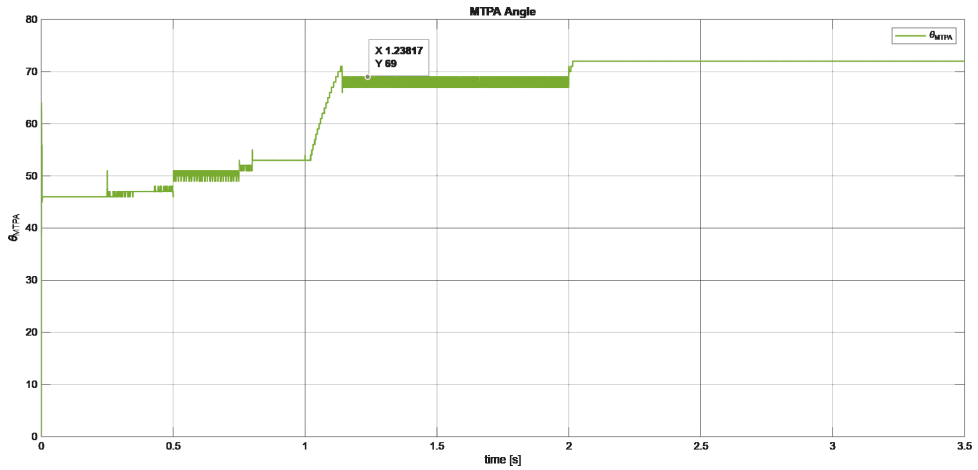


Figure 29: Current vector I_s angle

To complete the analysis of the result graphs, we present a graph comparing the reference torque generated by the speed loop with the electromagnetic torque produced by the machine and with the value estimated from the currents measured through the apparent inductance maps. The three traces overlap along the entire profile: the correspondence between the reference and the produced torque confirms the correct functioning of the control chain, while the correspondence between the produced torque and the estimated torque validates the maps and the torque expression adopted, as the estimate is obtained from an independent calculation based on the measured currents. The reference torque deviates from the estimate under motor acceleration conditions, but the current remains constrained by the current on the q-axis, as this represents the positive and negative limits of the required reference on q-axis loop.

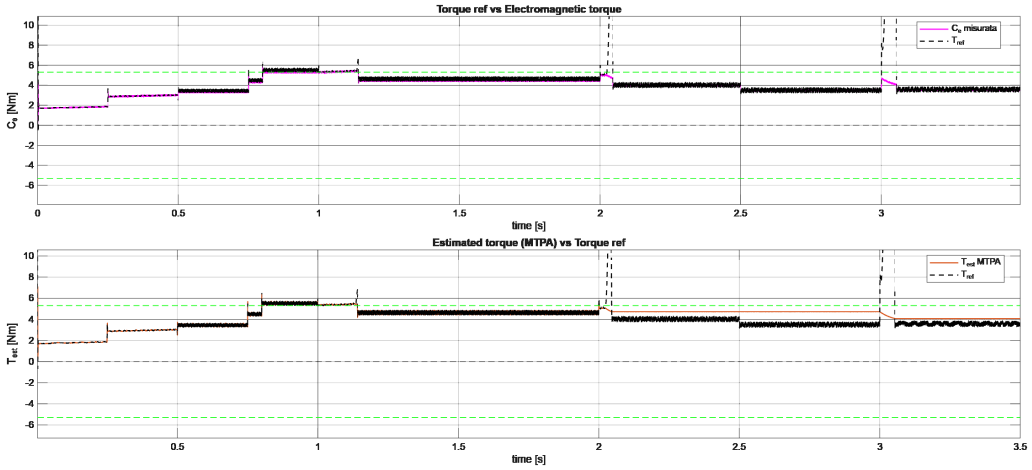


Figure 30: Torque reference vs Estimated Torque and measured Torque

5.2 Model-Based simulation

The second proposed model is a predictive model based on SynRM characteristics.

Again, the generic scheme can be considered as a set of three interconnected macrogroups: the external speed loop, the internal MPC-based current loop, and the system to be controlled.

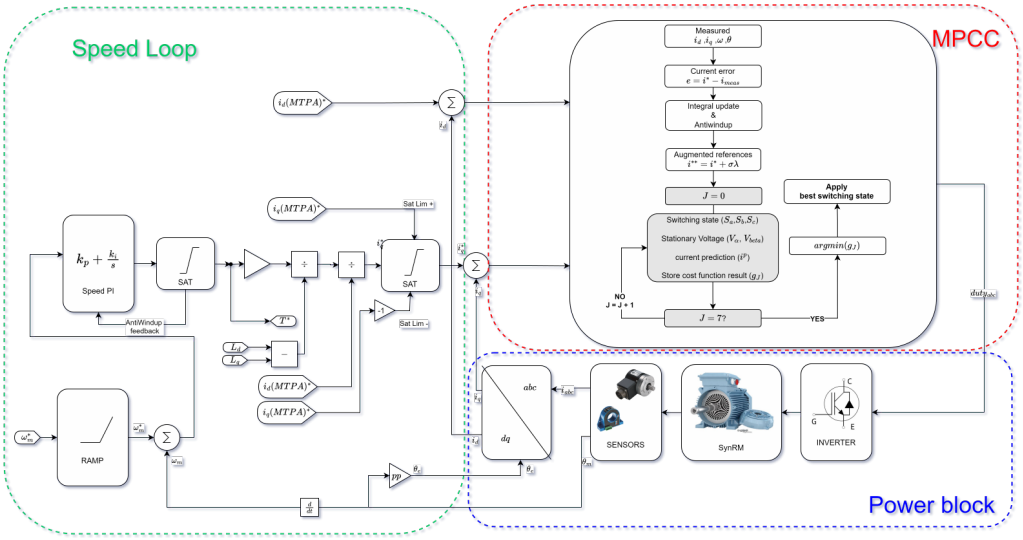


Figure 31: Block diagram of MPCC model for SynRM

The current loop uses the MPC algorithm to define the switch states. The steps of the MPC algorithm implemented in the simulation phase and described in detail in this chapter take shape in the diagram in fig.32.

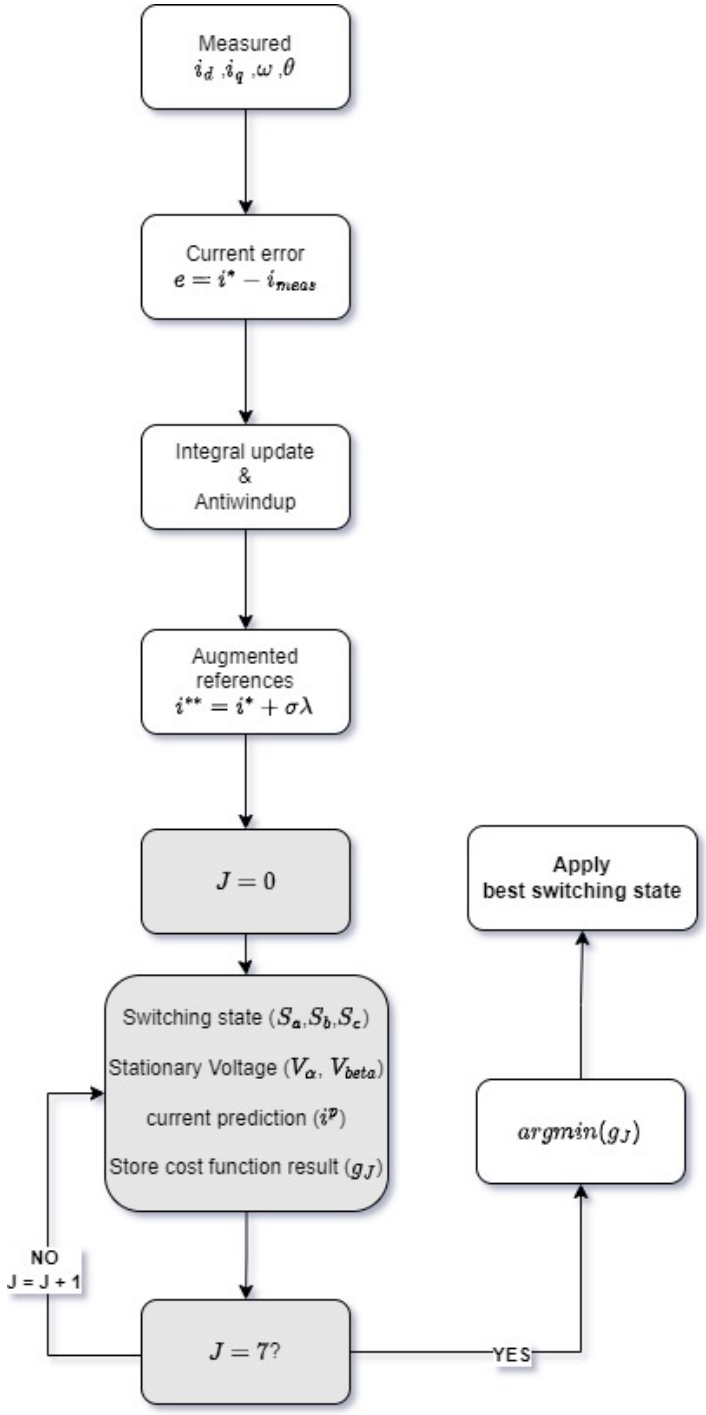


Figure 32: Flowchart of FCS-MPCC for a two-level inverter

The algorithm is composed of three main phases: error evaluation and integral calculation with Antiwindup, evaluation of each individual admissible state, and output generation of commands that minimize the cost function g.

The cycle begins with the measurement of the stator currents $i_d(k)$, $i_q(k)$ and the rotor position and speed $\theta(k)$,$\omega(k)$, the latter being necessary for both the Park projection of the candidate vectors and the motion terms of the prediction model.
The second phase updates the integral action. The current errors are accumulated, constrained to I_{max}, and the augmented references i_d^*, i_q^* are formed. This phase has no counterpart in the classical formulation [28], where the absence of an integral action leaves a steady-state current error whenever the prediction model does not exactly match the machine [37]. Two routes are available to recover zero steady-state error. In [38] an integral contribution is embedded in the cost function itself, so that it is evaluated for every candidate switching state and its weight has to be traded off against the tracking term. The scheme adopted here follows instead the cascaded approach of [37]: the integral state acts on the current references through (202), it is updated once per sampling period outside the evaluation loop, and the cost function (145) remains a plain Euclidean norm of the tracking error. The integrator is protected against windup by the back-calculation scheme of (200), following [39].

$$e_d(k) = i_d^*(k) - i_d(k), \qquad e_q(k) = i_q^*(k) - i_q(k), \tag{198}$$

The integral state is inherently unbounded: whenever the available inverter voltage is insufficient to track the reference, the accumulated error keeps growing and the controller winds up. To prevent this, the unconstrained integral state σ^u is limited to the rated current of the machine, I_{max}, according to (199), and the difference between the saturated and unconstrained values is feedback to the integrator input as in (200)–(201).

This value is not saturated, so to prevent the term from growing above the limits, it is saturated at the motor's nominal current.

$$\sigma^s = \mathrm{sat}\left(\sigma^u\right) = \begin{cases} I_{max} & \text{if } \sigma^u > I_{max}, \\ -I_{max} & \text{if } \sigma^u < -I_{max}, \\ \sigma^u & \text{otherwise,} \end{cases} \tag{199}$$

the result is feedback into the integrator according to the feedback scheme 31.

$$\sigma_d(k) = \sigma_d(k-1) + \Big[\big(\sigma_d^s(k) - \sigma_d^u(k)\big) + e_d(k)\Big] T_s, \tag{200}$$

$$\sigma_q(k) = \sigma_q(k-1) + \Big[\big(\sigma_q^s(k) - \sigma_q^u(k)\big) + e_q(k)\Big] T_s. \tag{201}$$

The references to be passed to the cost function are obtained by adding the reference required by the MTPA function to the weighted integral state [38].

$$i_d^{**}(k) = i_d^*(k) + \lambda_i \sigma_d(k), \qquad i_q^{**}(k) = i_q^*(k) + \lambda_i \sigma_q(k) \tag{202}$$

where λ_i is the integral gain, dimensionally the inverse of a time, since σ has the dimensions of a current multiplied by a time.
The cost function also has a slightly different form than the one usually expressed (140), among the reference formulations discussed in [28, Chap. 10], the Euclidean norm of the error vector in the dq plane was adopted:

$$g_j = \sqrt{\Big(i_d^{**}(k) - i_{d,j}^p(k+1)\Big)^2 + \Big(i_q^{**}(k) - i_{q,j}^p(k+1)\Big)^2}, \qquad j = 0, \ldots, 7, \tag{203}$$

where j indicates the switching states of the two-level inverter and the superscript p denotes a predicted quantity.

The third phase is the prediction loop, repeated for $j = 0, \ldots, 7$. For each index, the corresponding switching triplet (S_a, S_b, S_c) is retrieved; The inverter model produces the following stationary components:

$$v_\alpha = \frac{2}{3} V_{dc} \left(S_a - \frac{S_b}{2} - \frac{S_c}{2}\right), \qquad v_\beta = \frac{V_{dc}}{\sqrt{3}} (S_b - S_c), \tag{204}$$

that the Park transformation projects onto the rotor reference system:

$$v_{d,j} = v_\alpha \cos\theta + v_\beta \sin\theta \qquad v_{q,j} = -v_\alpha \sin\theta + v_\beta \cos\theta \tag{205}$$

The predicted currents are derived from (136)–(137), and the cost (203) is stored in position j of an array. Only $v_{d,j}$ and $v_{q,j}$ change over the eight evaluations: the mea-

sured quantities, the interpolated inductances at the operating point, and the integral terms are common to all and are calculated only once, which reduces the body of the loop to a few arithmetic operations. Once the matrix is completed, the index that minimizes the cost is selected:

$$J = \arg \min_{j \in \{0,\dots,7\}} g_j, \tag{206}$$

the corresponding switching state is applied to the inverter gates for the entire subsequent sampling interval. No modulator is involved: the controller output is a switching pattern, not a voltage reference, which is the distinguishing feature of the Finite Control Set approach.

Also on this model simulation are verified several functional aspects, such as the correct tracking of the references and the shape of the inverter's output currents and voltages.

Furthermore, the graphs related to the distribution of the vectors used and the result of the cost function are analysed. The predictive controller was tested on the same speed and load profile presented in the graph 19.

Figure Figure 33 shows that the controller follows both current references throughout the profile, without any steady-state offset on either axes: the algorithm shows in the diagram Figure 32 is able to remove the residual error between references and measured current.

The oscillation, which can be clearly seen in the graph, is greater than the one obtained with the PI controller in Chapter 4.2. A notable feature is the asymmetry between the axes: the amplitude of the oscillation on the quadrature current is greater than the direct axis, which is the consequence of saliency, since a given voltage error produces a current variation inversely proportional to the inductance. Since L_q is much smaller than L_d, the current error is more evident on the quadrature axis.

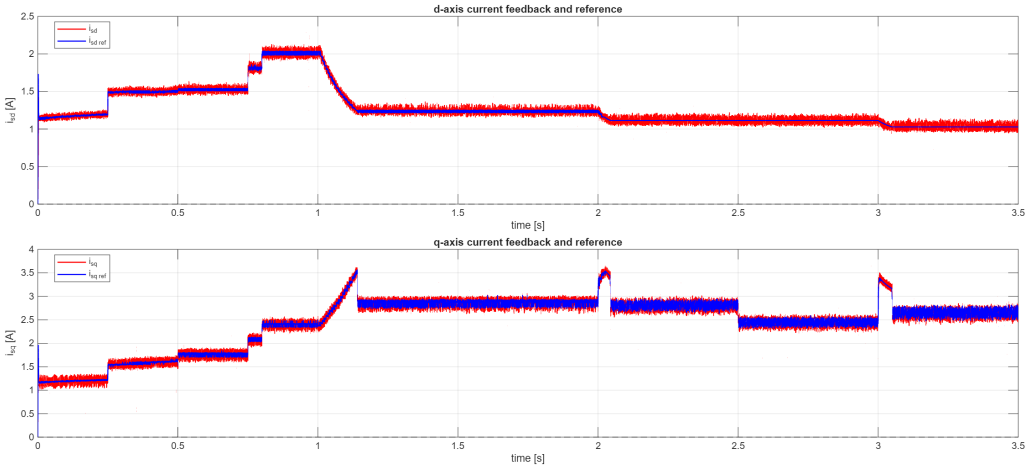


Figure 33: Current in dq frame MPC control

Figure 34 shows the imposed speed profile. After an initial ramp that brings the machine to the base speed $\omega_{base} = 158 rad/s$ in 0.5 seconds, three subsequent phases bring the motor to 220,240 and $260 rad/s$ all above the base speed and therefore in the field weakening region.

The measured speed follows the reference without overshoot.

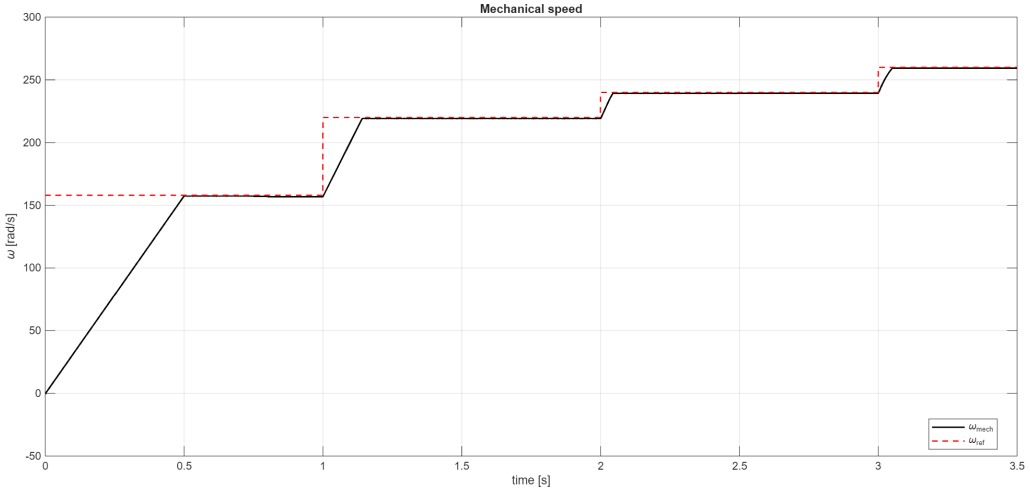


Figure 34: Mechanical speed MPC control

Figure Figure 35 summarizes the entire test in the dq current plane.

At low speed, the operating points, shown in blue, lie on the MTPA locus; as the required torque increases, the points follow the trajectory generated by the MTPA algorithm. In the field-weakening region, the d and q current references progressively deviate from the MTPA trajectory, while still remaining within the current circle and the voltage ellipse.

The trajectory therefore confirms that the reference generation stage correctly transitions from the MTPA strategy to field-weakening. The visible thickness of the point cloud is the current oscillation observed in fig. 33, represented here as a dispersion around the nominal operating point and not a temporal trend.

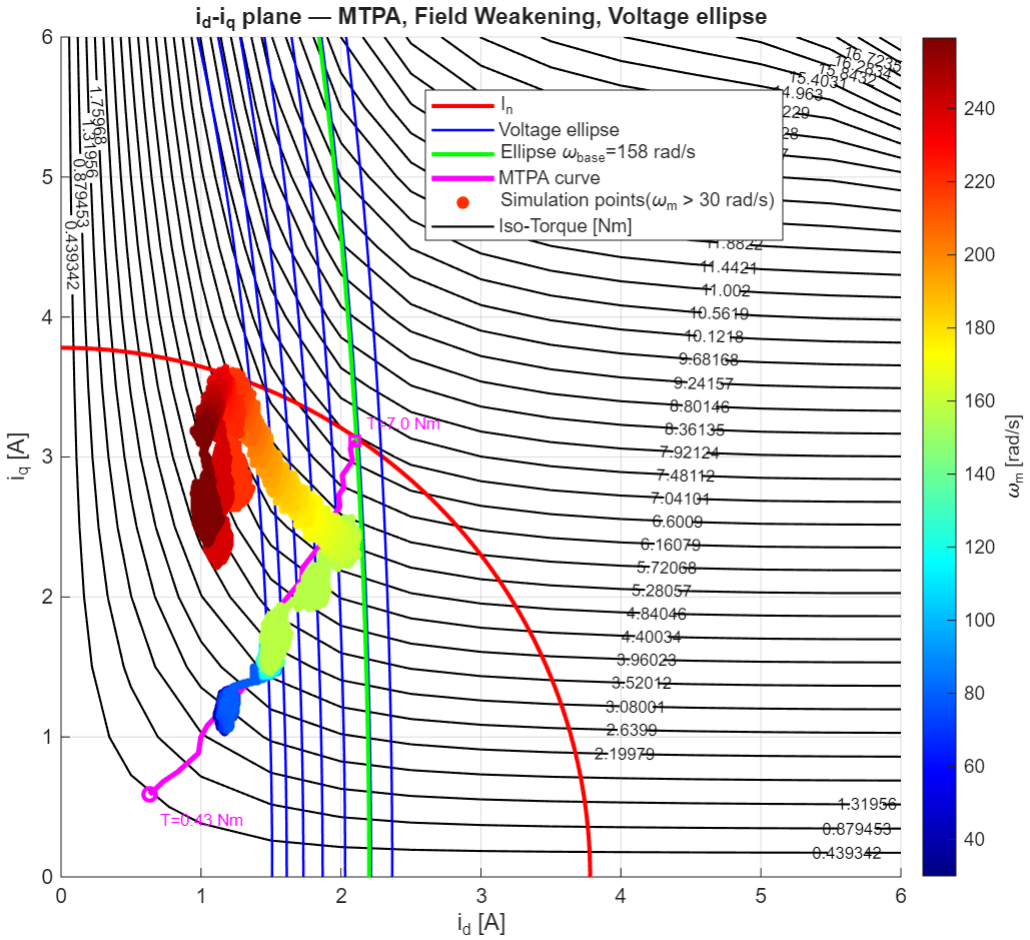


Figure 35: dq plane MPC control

Figure 36 shows the interpolated apparent inductances at each sampling time. Both L_d and L_q decrease as the load increases, which quantifies the saturation of the machine in the tested range. The variation is far from negligible, and justifies the interpolation of the maps at each step rather than the use of constant parameters. Essentially, the calculated inductances are equal to the inductances calculated in the PI strategy simulation fig. 26.

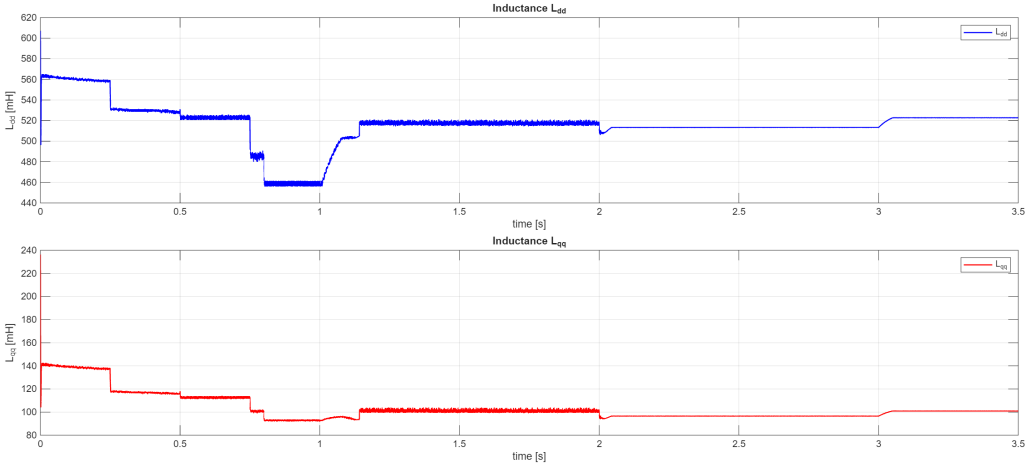


Figure 36: Interpolated L_d and L_q

Also in this simulation, the phase current trends are observed fig. 37. The waveforms remain sinusoidal and balanced, with an amplitude that increases with the load up to the nominal value, and a frequency that increases with speed. The current limit is respected throughout the path; the peaks approach but never exceed the dotted lines, only in the sections of the profile where the contribution from the speed increase request is added to the required load, bringing the motor to the new required reference speed. The thickness of the trace is the same as the one observed in the dq frame.

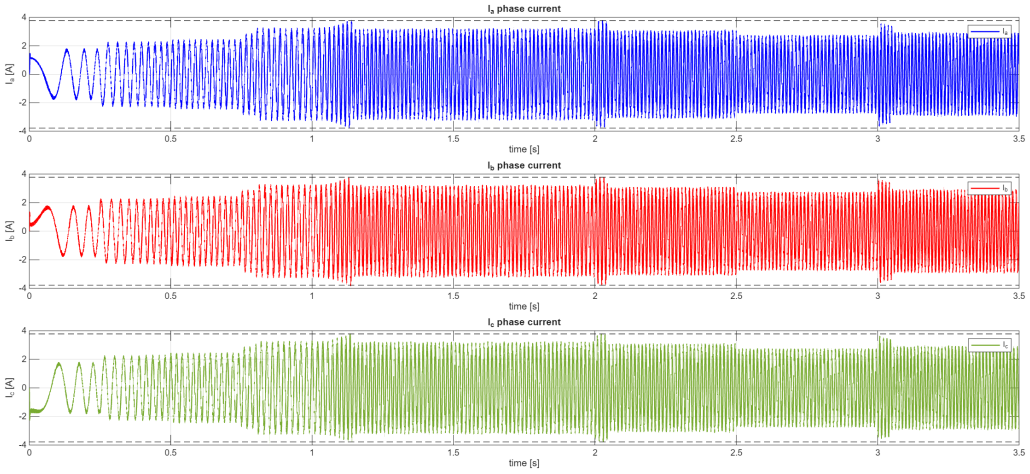


Figure 37: Three phase current in abc frame

Figure Figure 38 shows the voltages applied to the machine. Unlike the modulated case, a regular pulse pattern cannot be recognized: the width and position of the pulses vary continuously, because the controller decides at each sampling instant which state to apply without any carrier to synchronize with. The drive, therefore, does not have

a switching frequency in the usual sense, but only an average switching frequency, and the harmonic content is distributed over a wide band rather than concentrated around a single carrier and its multiples.

The average switching frequency and its ratio to the switching frequency are extracted from the simulation.

Let $j(k) \in \{0,\dots,7\}$ be the index of the voltage vector selected at the k-th sampling instant: a commutation event is counted whenever the index changes between two consecutive instants,

$$N_{\text{sw}} = \sum_{k=1}^{N-1} \{|j(k+1) - j(k)| > 0\}, \tag{207}$$

where N is the number of samples contained in the observation window $T_{\text{sim}} = t(N) - t(1)$. Since every change of the applied vector is shared among the three legs of the inverter, the mean switching frequency per phase is estimated as

$$\bar{f}_{\text{sw}} = \frac{N_{\text{sw}}}{3\,T_{\text{sim}}}, \tag{208}$$

which is conveniently normalised to the sampling frequency $f_s = 1/T_s = 20kHz$. The ratio

$$\bar{f}_{\text{sw}}/f_s \tag{209}$$

represents the average fraction of sampling periods that actually produce a commutation. A transition in (208) between two non adjacent vectors involves more than one phase, but is counted only one time, so the function return an an underestimate value. In the specific case of the simulation, the following results can be observed:

The results are indeed consistent with the behaviour observed in [28].

The switching frequency remains below the structural limit of $f_s/2$, which arises from the fact that at most one switch per leg can occur at any sampling time, and lies close to the $f_s/5$–$f_s/4$ band typically observed in finite control set schemes [28].

Table 3: Estimated switching activity of the FCS–MPCC controller.

Quantity	Symbol	Value	Unit
Sampling period	T_s	50	μs
Sampling frequency	f_s	20000	Hz
Observation window	T_{sim}	3.50	s
Number of samples	N	70000	–
Vector changes	N_{sw}	56572	–
Commutation density	N_{sw}/N	0.808	–
Mean switching frequency	$\bar{f}_{\text{sw}}$	5387.9	Hz
Normalised rate	$\bar{f}_{\text{sw}}/f_s$	0.269	–

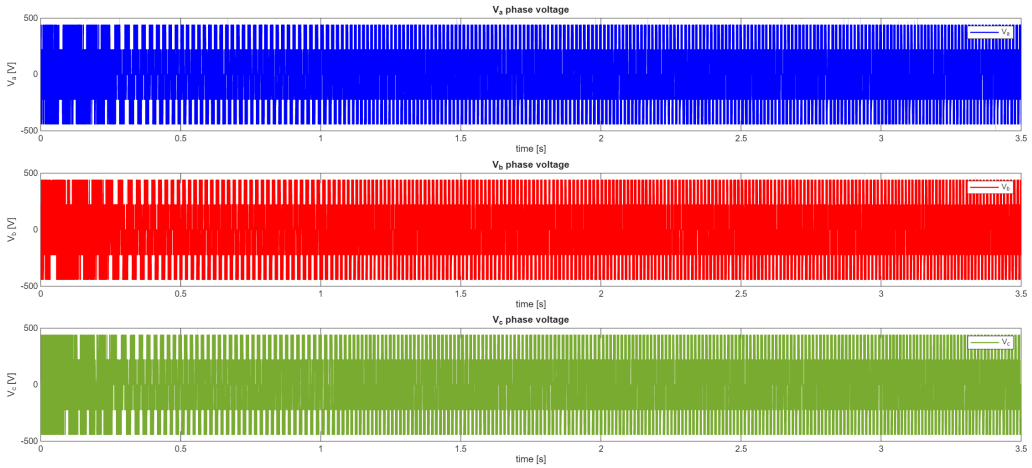


Figure 38: Three phase voltage in abc frame

The current vector angle, fig. 39, increases from 46 deg up tp 72 deg as the operating point moves along the MTPA locus and then in the field weakening phase, where it stabilizes at a constant value. The angle behaviour closely follows that seen in the chapter on the PI model simulation fig. 29.

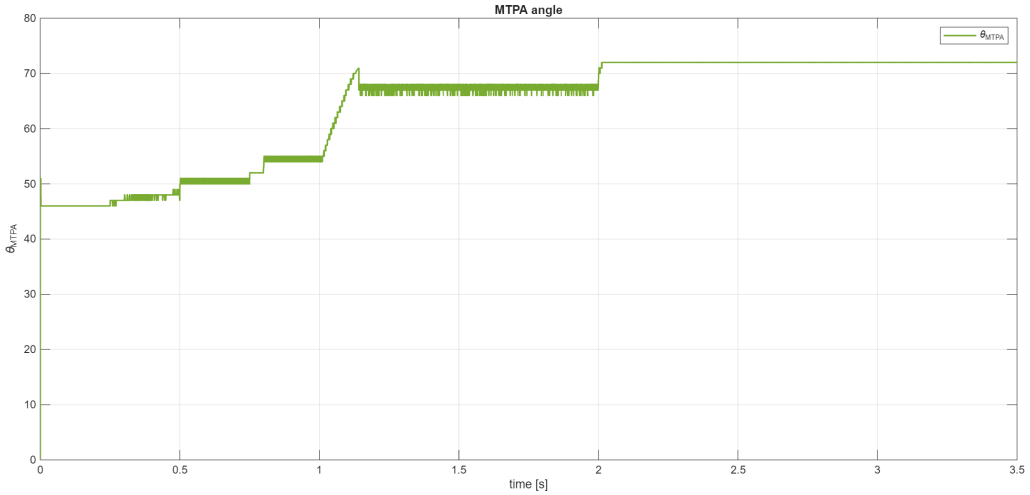


Figure 39: Current vector I_s angle

The fig. 40 figure shows torque results. The top graph compares the torque reference generated by the speed controller with the measured torque. The reference generated by the speed control circuit exhibits pronounced peaks at each speed increase, but is still limited to the current value, so that the torque delivered never exceeds the nominal value indicated by the horizontal dashed lines. The measured torque closely follows the reference value in the lower part of the graph, with an oscillation consistent with what is seen in the current graphs. The bottom graph compares the torque estimated by the MTPA algorithm with the torque reference generated by the speed controller.Up to two seconds, the torque estimated from the MTPA reference values coincides with the reference value. As the timeline progresses, these two values diverge. This is not a malfunction, but rather the phase in which the estimate binds the current references to the circumference.

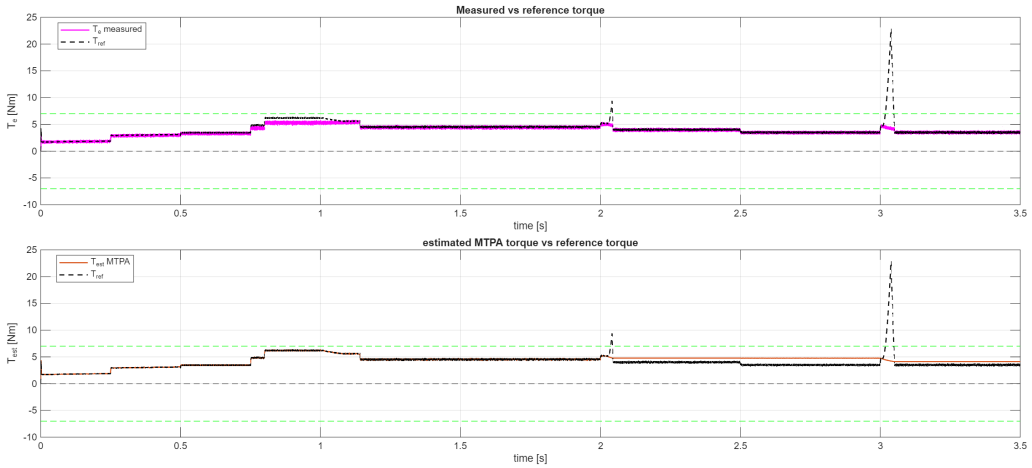


Figure 40: Torque reference vs Estimated Torque and measured Torque

The top graph of fig. 41 shows the value of the cost function after minimization, the residual distance between the predicted current and its reference among the eight candidates. It is therefore the most direct measure of the intrinsic limitation of the Finite Control Set approach: it quantifies how far the controller necessarily remains from the target because no available voltage vector can bring the current exactly to the reference value within a sampling period.

The residual follows the growth of the speed rather than the load. The reason lies in the prediction model (136)–(137): the motion terms are proportional to ω, so as the speed increases, a progressively larger fraction of the available voltage is absorbed to balance them, and the remaining margin to correct the current error decreases. Isolated

peaks, on the other hand, coincide with the reference steps.

The lower graph shows the applied switching state index. The selection continuously alternates between the active vectors and the null vector at a non-constant rate, which is the visible signature of the method's variable switching frequency.

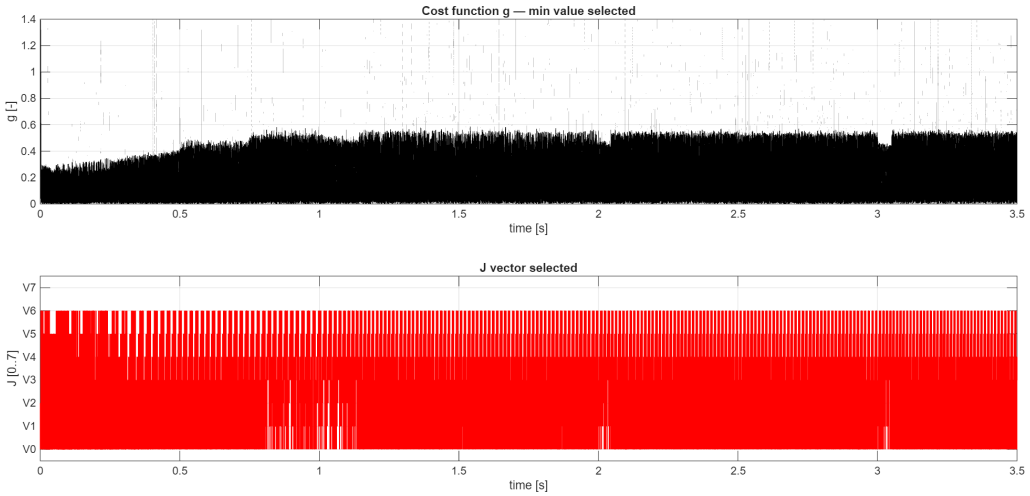


Figure 41: Cost function g and selected vector J

Figure Figure 42 aggregates the same information across the entire simulation. The six active vectors are used uniformly; the absence of asymmetry between the six active vectors confirms that Park's projection of the candidate vectors and the flow maps are consistent across all sectors.

The distribution of the null vectors, however, is strongly skewed: V_0 represents 12.3% of the sampling periods, while V_7 is never selected. This is not a numerical artifact of the simulation, but a structural consequence of the implementation. The two states $(0,0,0)$ and $(1,1,1)$ produce the same zero voltage vector via (204), thus identical forecasts and identical costs; The minimization (206) is solved by the `min` operator, which returns the first occurrence of the minimum, and the loop analyses the states in increasing order. Each parity is then assigned to V_0, and V_7 becomes unreachable by construction.

A future improvement of the algorithm is to analyse the current state of the switch and the selected switch state to minimize the number of physical commutations. In fact, applying V_0 instead of V_7 or vice versa would allow the null vector to be reached by switching a single leg of the inverter instead of three, with a direct reduction in switching losses. This solution is also suggested in the literature. [28, Chap. 10].

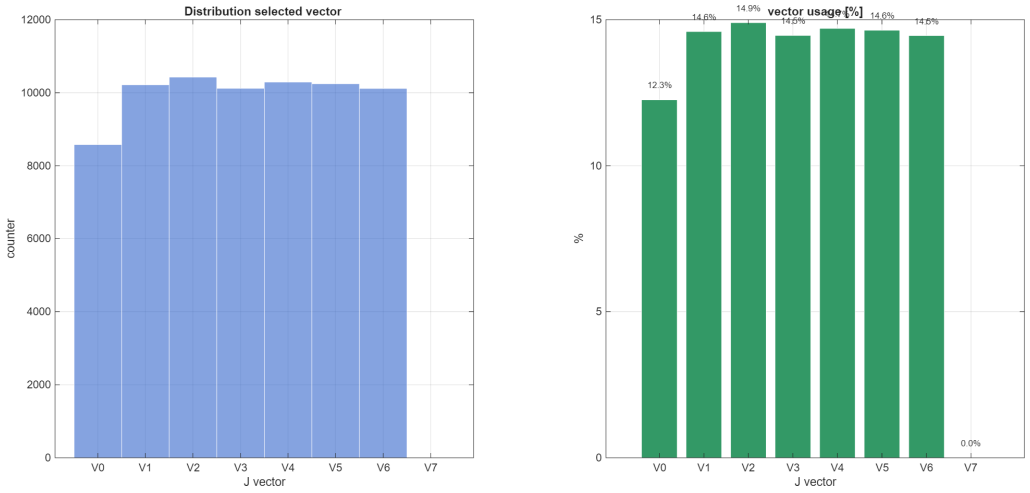


Figure 42: Distribution J vector

5.3 Model-Free simulation

The MFPC control strategy is also implemented and executed, as in the previous cases. The Ultralocal model presented in 4.4 is implemented as shown in the flow chart below.

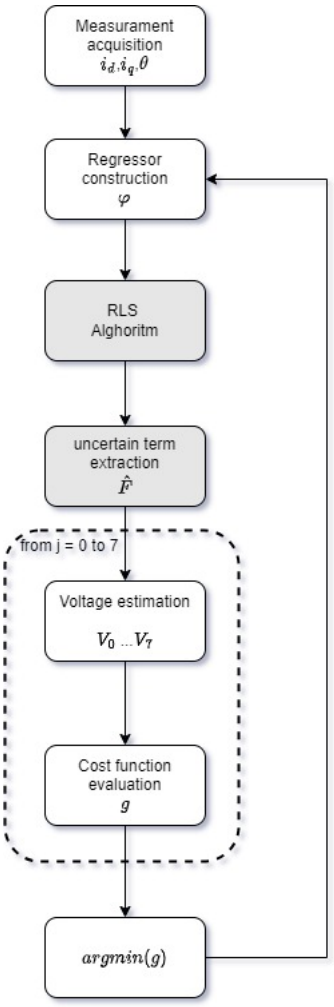


Figure 43: Ultralocal model

The recursive RLS parameter identification algorithm is embedded within the Ultra Local model, also described in detail in 4.4 and here presented in flow chart form.

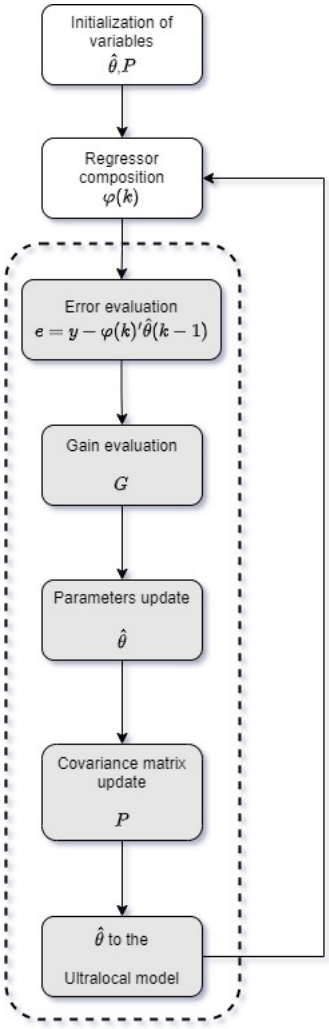


Figure 44: RLS algorithm

The two interconnected algorithms are inserted within a complex system already used in previous models, using the MTPA algorithms to generate current references in the *dq* plane, and an external speed loop that governs the motion of the system to be controlled, the synRM seen in detail in the 3.1 section.

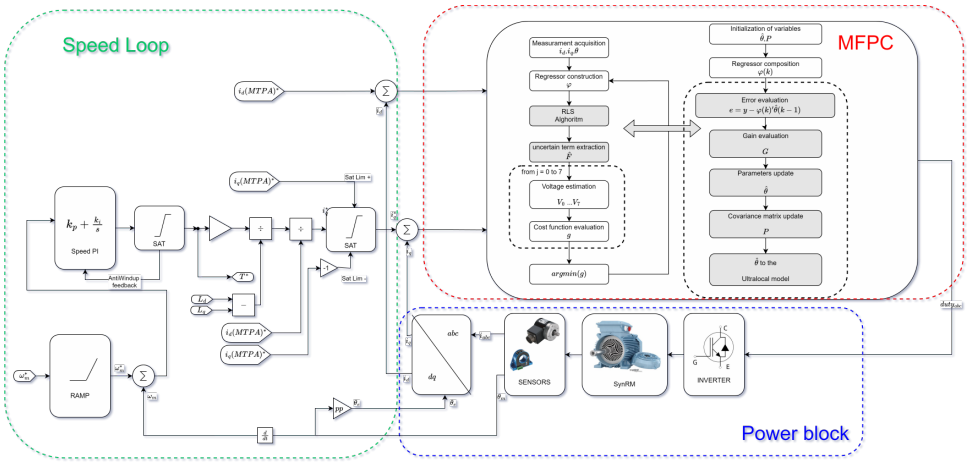


Figure 45: MFPCC control

In this case, we begin by showing the graph of the dq current 46, which, unlike previous simulations, compares the measured currents with the current predicted by the model-free algorithm. It is interesting to note how the traces on both the direct and quadrature axes are super imposable, confirming that the uncertain term $\hat{F}_{dq}$ is indeed capable of capturing the unmodeled dynamics.

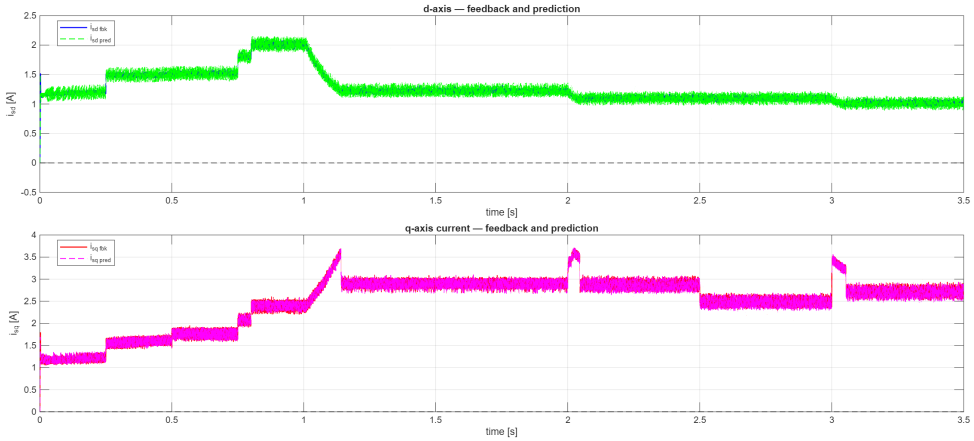


Figure 46: current feedback and current predicted

For completeness and comparison, Fig. 47 shows the speed tracking, which is free of overshoot and the steady-state error is zero in all segments.

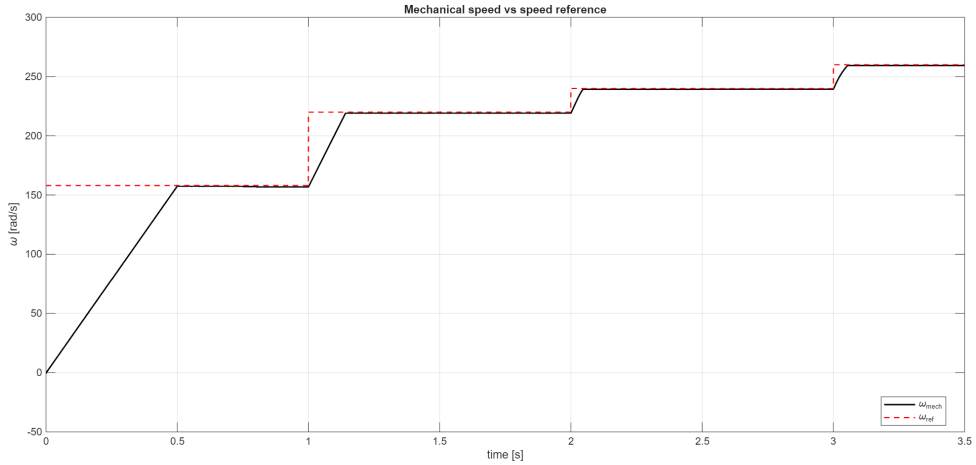


Figure 47: mechanical speed MFPC control

In the dq plane shown below, 48, highlights the respect of the trajectory generated by the MTPA algorithm common to all control strategies.The oscillation around the optimal point of the trajectory is common to the predictive algorithm based on the machine model discussed in the previous section 5.2.

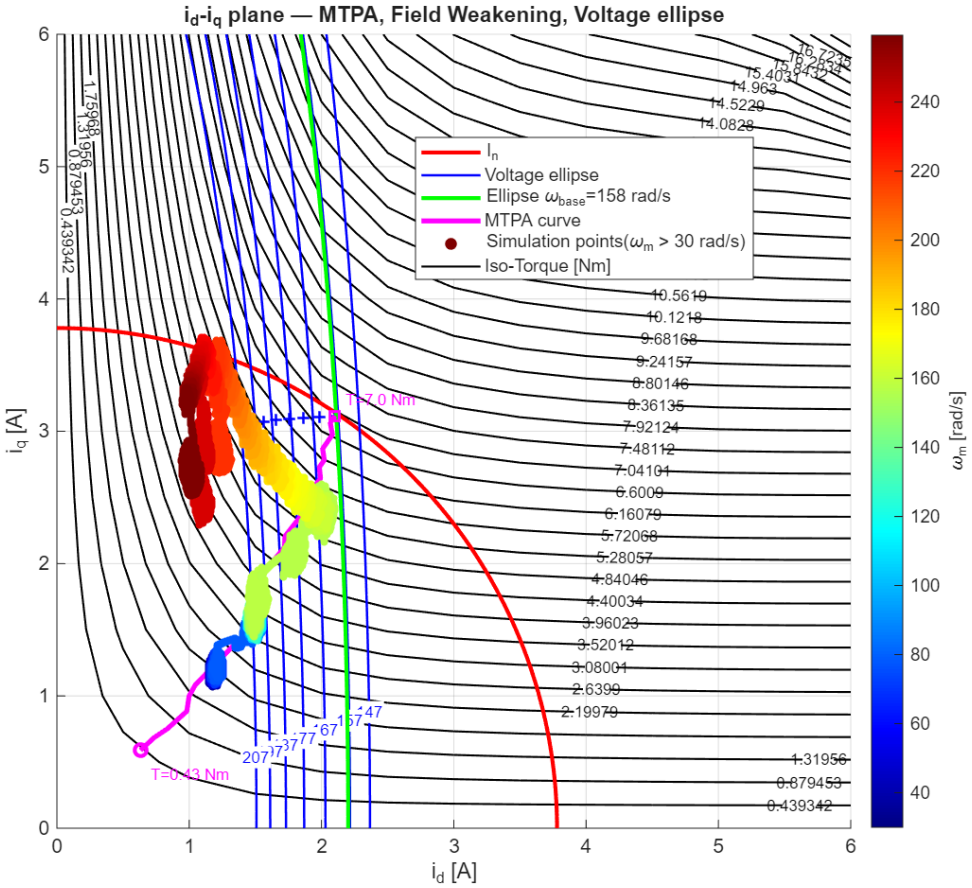


Figure 48: dq plane MFPC control

Essentially, the calculated inductances are equal to the inductances calculated in the PI strategy simulation Fig. 26, and in the MPC strategy 36. The inductances adopted in the model are fixed and equal to $\alpha_d = 1/0{,}51$ and $\alpha_q = 1/0{,}0824$, which differ significantly from what is shown in the figure. The reference tracking of the MFPC strategy implemented here is nevertheless sufficiently accurate, and this in no way contradicts the formulation, but rather reinforces it experimentally. The error in the parameters α_d and α_q is entirely absorbed by the term $\hat{F}_{dq}$.

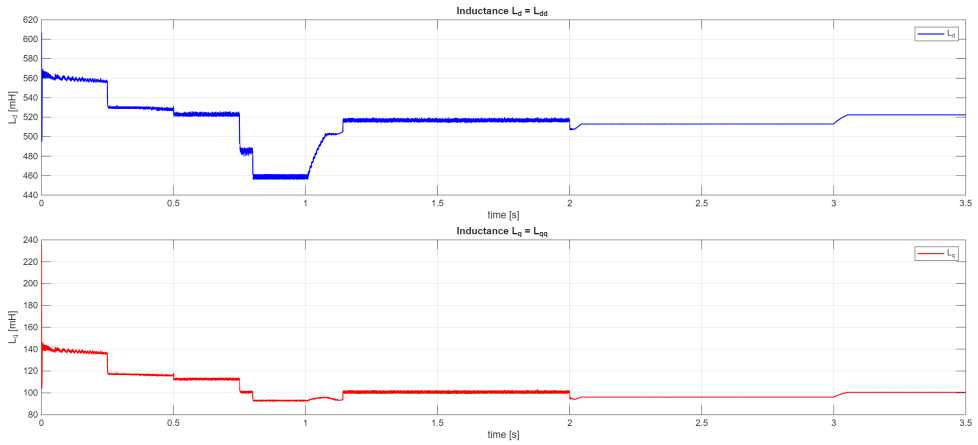


Figure 49: Interpolated L_d and L_q

The phase currents, in Fig. 50, remain within the permissible band of $\pm 3{,}8$ A for the entire duration of the test, with a sinusoidal waveform and switching ripple typical of finite command set control, in which the absence of a modulator results in a distributed spectrum rather than concentrated on multiples of the carrier; the phase voltages, in Fig. 51, show the characteristic behavior generated by the direct selection of the inverter vectors.

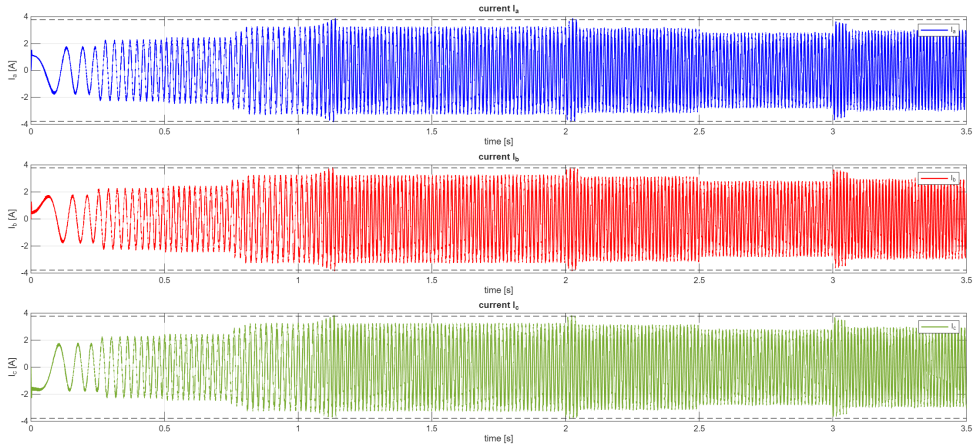


Figure 50: Three phase current in abc frame

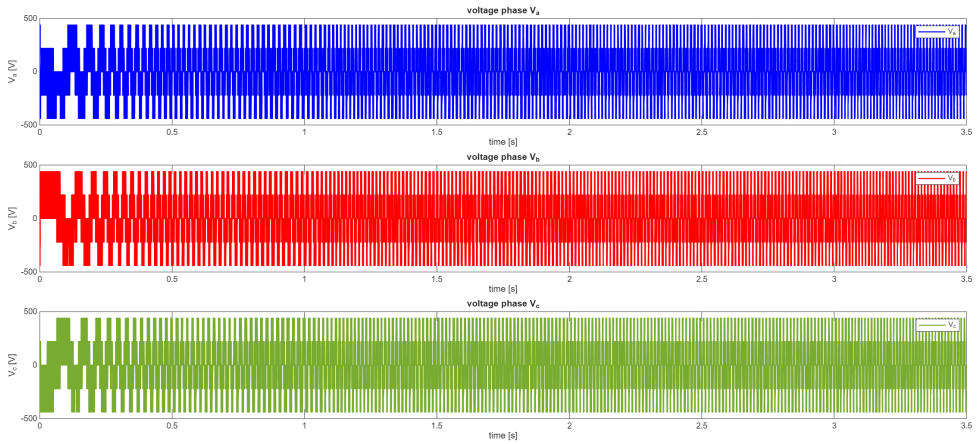


Figure 51: Three phase voltage in abc frame

The angle of the vector, evolves from 46° and 72° following the variation of the current references.

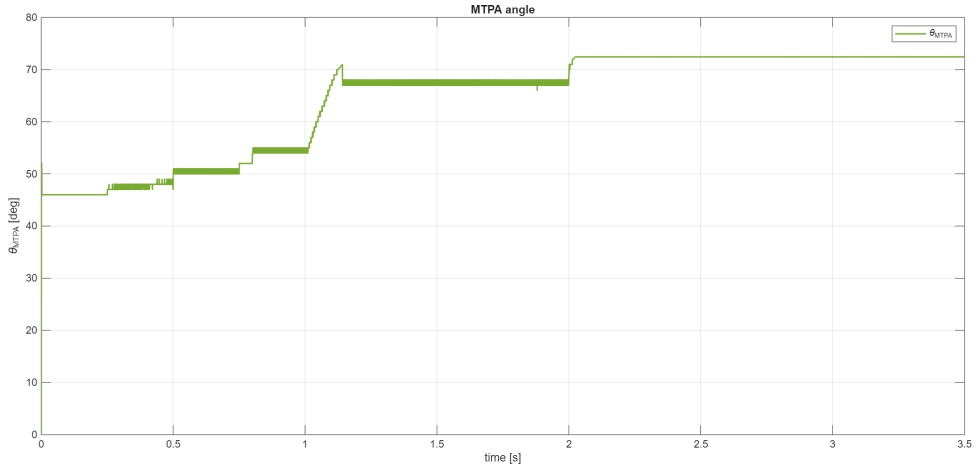


Figure 52: Current vector I_s angle

In Fig. 53 the torque tracking is shown, where the measured and estimated torque coherently track the reference generated by the speed loop.

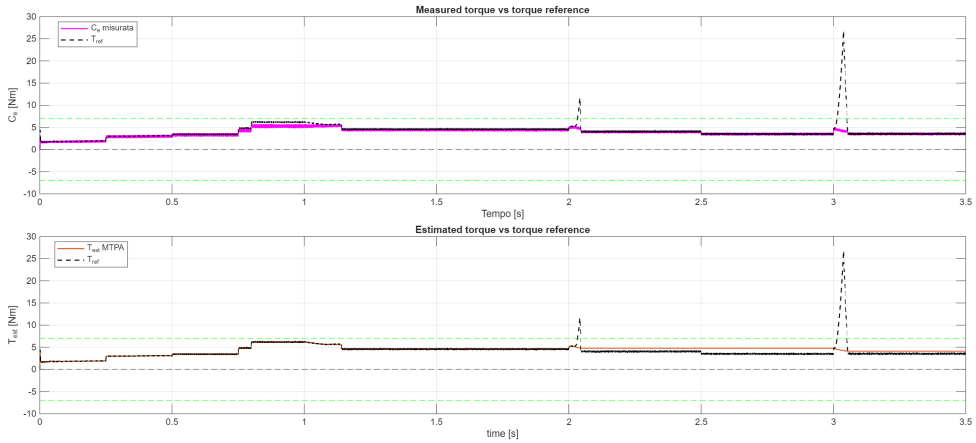


Figure 53: Torque reference vs Estimated Torque and measured Torque

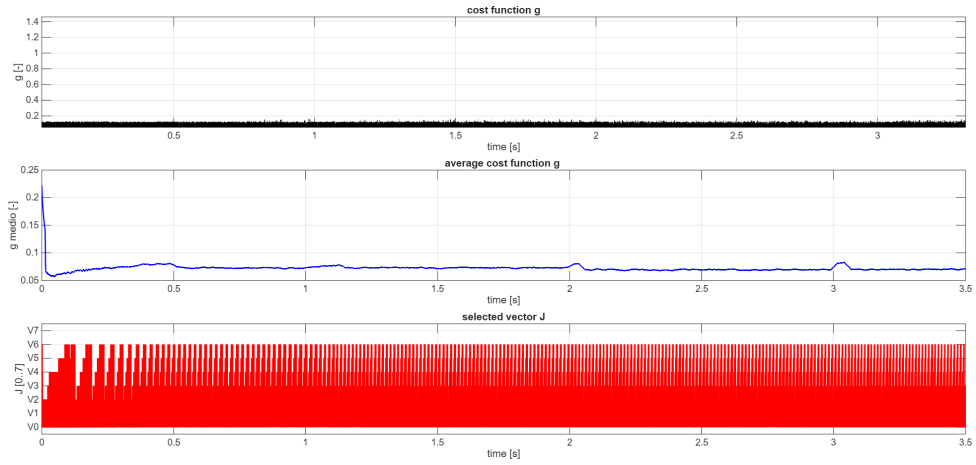


Figure 54: Cost function g and selected vector J

The figure 55shows that the selection of J vectors is uniform and occurs around 12,0%. The null vector, on the other hand, is used approximately twice as often; it is selected whenever the error is close to zero without further voltage application. Even in this case, the vector applying the voltage V_7 is never selected, as this strategy is affected by the same behavior already seen in the implementation of the MPC model 5.2.

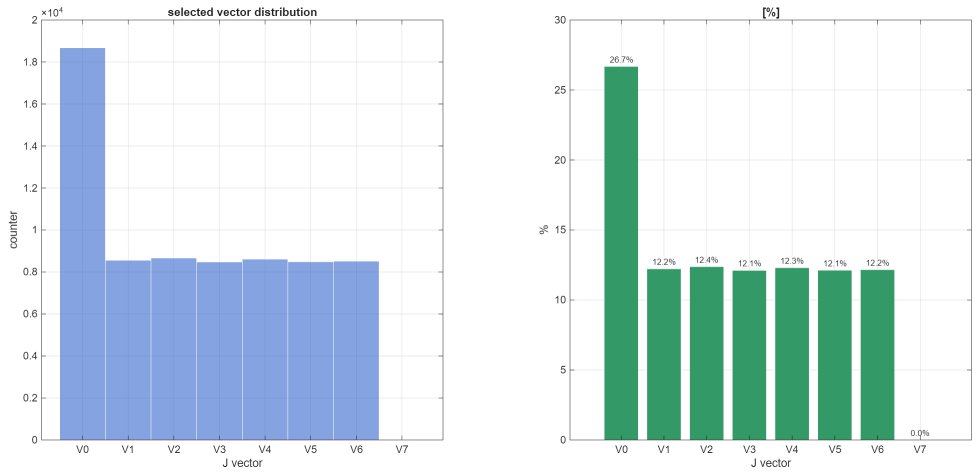


Figure 55: Distribution J vector

5.4 INDI simulation

As for the strategies discussed in the sections section 4.5, the control law (189)–(190) has been implemented in Simulink and tested with the SynRM motor model, under the same operating conditions, so that the results can be compared directly. The complete block diagram is shown in Fig. 56. The outer speed loop and the reference generation are unchanged with respect to the field-oriented scheme: the speed PI produces the torque demand, and the MTPA, field-weakening and MTPV strategies convert it into the current references $i_{d,\mathrm{ref}}$ and $i_{q,\mathrm{ref}}$. What changes is the current loop, which is composed of four blocks. The reference model implements (191) and generates the desired pseudo control from the tracking error, one instance per axis. The bandwidths $\omega_{c,d}$ and $\omega_{c,q}$ of the reference model are not chosen independently: they are derived from the design of the PI current controller, so that the two strategies are tuned with the same criterion. This is possible because INDI can be rewritten as a discrete PI controller, in which the inverse of the integral time, $T_I^{-1} = K_i/K_p$, sets the pole of the desired error dynamics $\dot{e} + \omega_c e = 0$ [40].

The PI gains are obtained by placing the closed-loop poles of each axis at the natural frequency $\omega_n = 2\pi f_i$ with damping factor ζ:

$$K_p = 2\zeta\,\omega_n L - R_s, \qquad K_i = \omega_n^2 L, \tag{210}$$

with $L = L_d$ or L_q for the two axes. The bandwidth of the reference model is then the zero of the equivalent PI:

$$\omega_{c,d} = \frac{K_{i,d}}{K_{p,d}}, \qquad \omega_{c,q} = \frac{K_{i,q}}{K_{p,q}}. \tag{211}$$

With $\zeta = 0.707$, $f_i = 4$ kHz, $L_d = 0.1595$ H, $L_q = 0.0824$ H and $R_s = 6.2\ \Omega$, one obtains $\omega_{c,d} \simeq 17.8 \times 10^3$ rad/s and $\omega_{c,q} \simeq 17.8 \times 10^3$ rad/s . The PI controller, designed with the same procedure at $f_i = 1$ kHz, has $K_i/K_p \simeq 4.5 \times 10^3$ rad/s, so the desired dynamics of INDI are about four times faster.

The on-board model evaluates $\dot{i}_{\mathrm{OBM}}$ from (184) at the measured operating point, and interpolates the incremental inductance matrix from the flux maps of Chapter 3.1. The augmentation branch computes the correction term of (188) from the measured currents, scaled by K_{aug} and filtered at f_{cut}, and adds it to the model estimate. The dynamic inversion block finally applies (189)–(190), taking the previously applied voltages from the unit delay placed in the feedback branch and the inductance terms from the on-board model. The resulting voltage references are passed to the space vector modulator operating at $f_{sw} = 20kHz$, as in the PI scheme case.

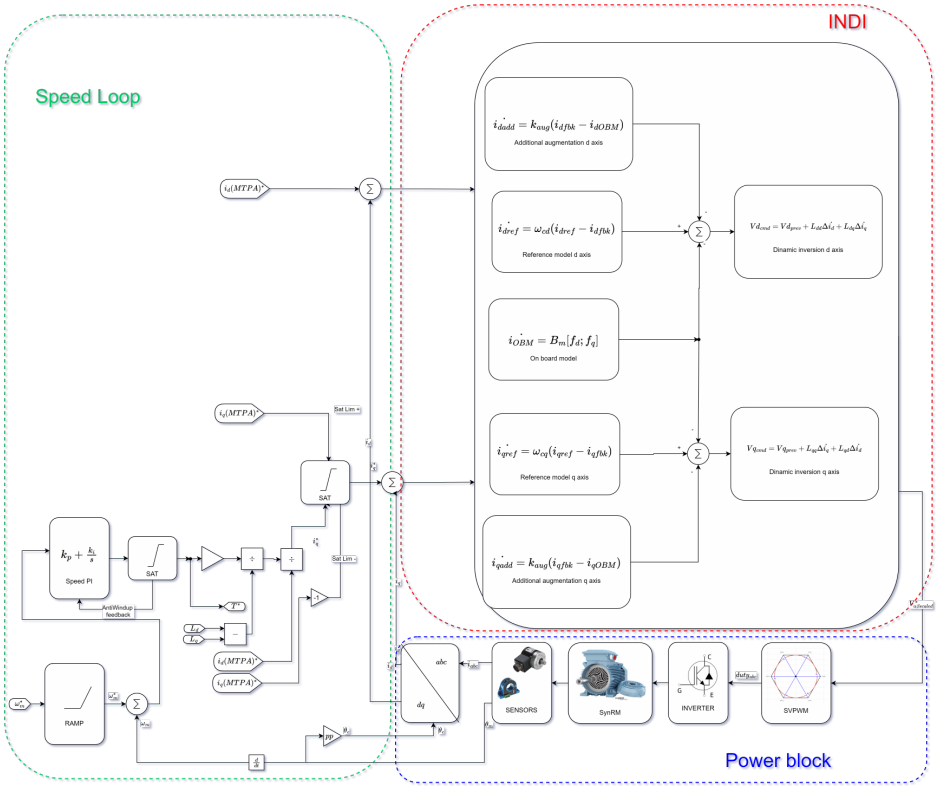


Figure 56: Complete block diagram of the INDI current control scheme.

The same test profile adopted for all others strategies has been applied, Fig. 57 shows the mechanical speed together with its reference, and Fig. 58 the corresponding d and q axis currents.

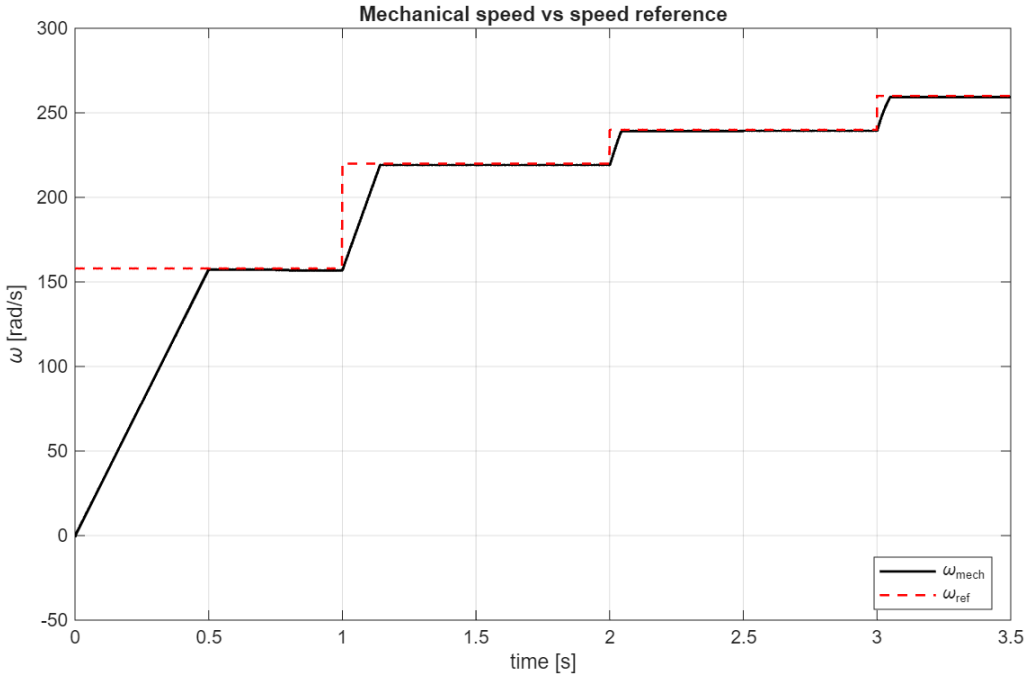


Figure 57: Speed reference and measured speed with the INDI controller.

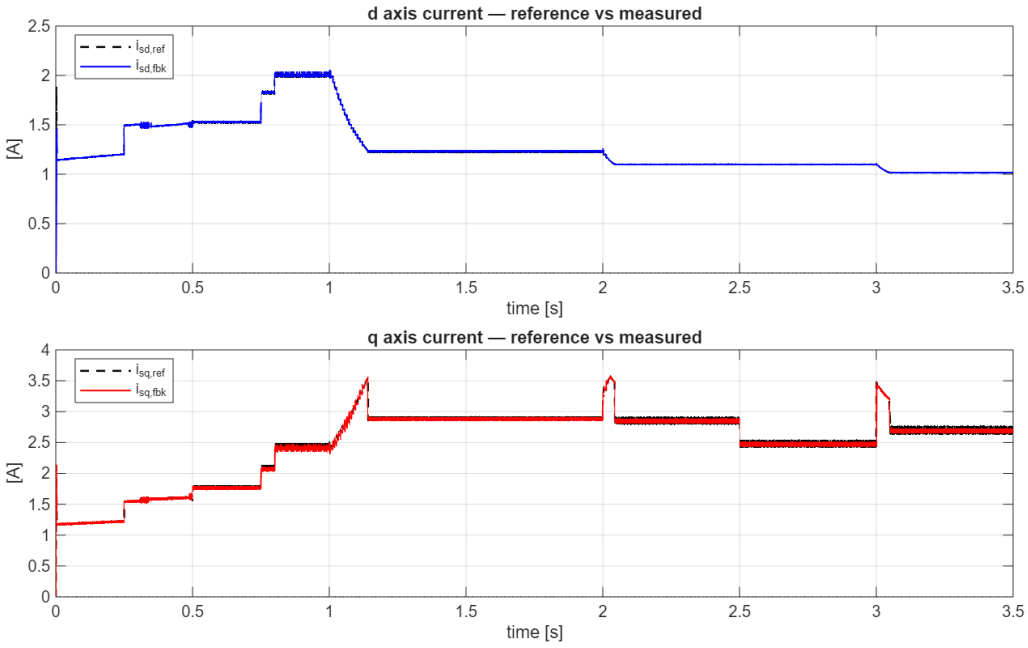


Figure 58: Direct and quadrature axis currents and their references.

The trajectory followed in the (i_d, i_q) plane is reported in Fig. 59, superimposed on the constant torque curves and on the current and voltage limit curves. It confirms that the operating point moves along the MTPA locus up to the base speed and then follows the field-weakening trajectory, as imposed by the reference generation stage.

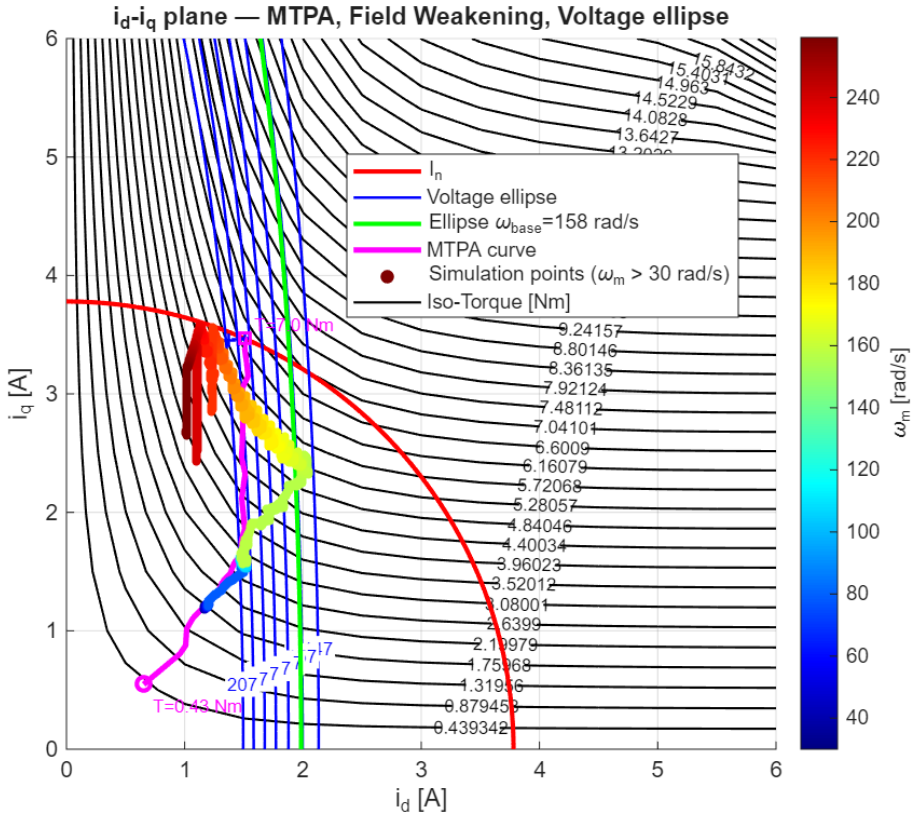


Figure 59: Operating trajectory in the (i_d, i_q) plane

Fig. 60 isolates the internal signals of the incremental law, which have no counterpart in the schemes examined so far: the desired pseudo control $\dot{i}_{\text{des}}$ produced by the reference model, the estimate $\dot{i}_{\text{OBM}}$ supplied by the on-board model, and the correction term contributed by the augmentation branch. The comparison makes the role of the blend (188) explicit. In steady state the model estimate follows the actual current derivative closely and the augmentation term remains small, so the loop behaves essentially as a model-based inversion. During the transients, and wherever the operating point moves into regions where the interpolated inductances are less accurate, the correction grows and compensates the residual model error, which is precisely the mechanism that makes the controller tolerant to parameter mismatch.

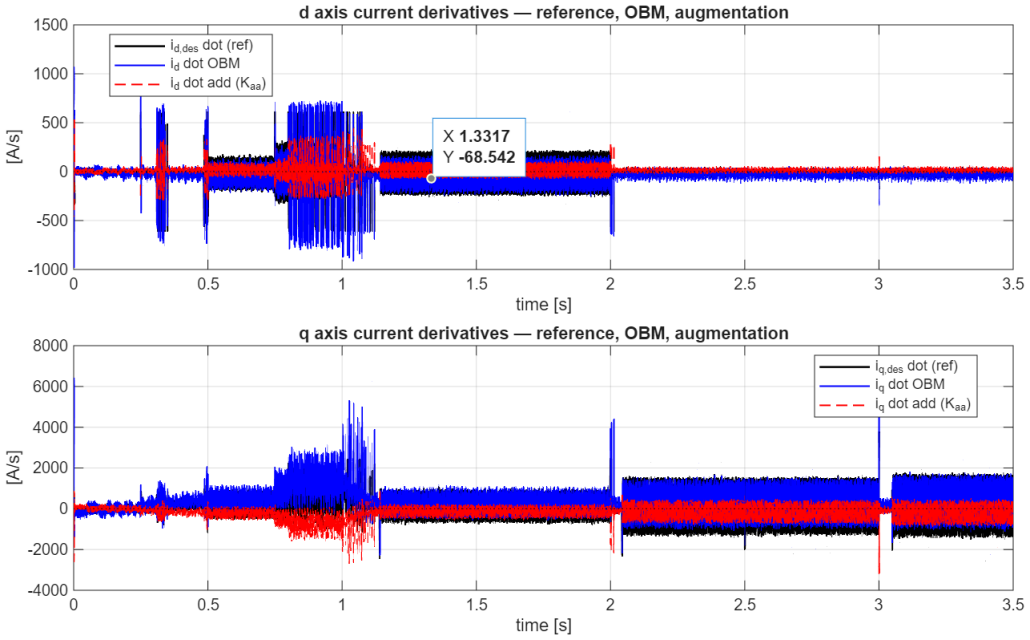


Figure 60: Desired pseudo control, on-board model estimate and augmentation correction on the d and q axis.

The electromagnetic torque is reported in Fig. 61, together with the reference imposed by the speed loop. Since the machine is controlled through its currents, the torque is not regulated directly: it follows from the current pair through the torque expression derived in Chapter 3.1, and its accuracy therefore reflects the accuracy with which the current loop tracks the references produced by the MTPA and field-weakening strategy.

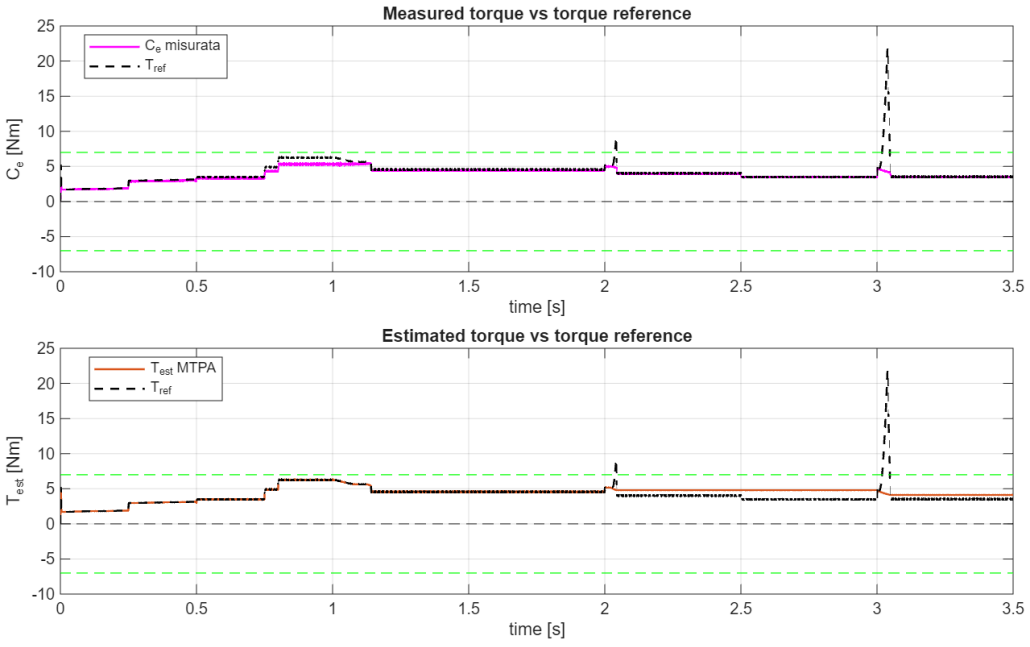


Figure 61: Reference and electromagnetic torque with the INDI controller.

6 Experimental

The control strategies discussed so far have been developed and compared in simulation. This chapter moves the comparison into hardware, the PI current controller of Chapter 4.2 and the hybrid INDI controller of Chapter 4.5 are implemented on the same control board and operate through the same power stage. Only the control law changes between the two sets of measurements, while sampling time, modulation, dead time, current sensing and DC-link arrangement remain unchanged. Any difference observed in the results can therefore be attributed to the control algorithm itself rather than to the experimental platform. The test bench consists of two machines mechanically coupled on a common shaft.

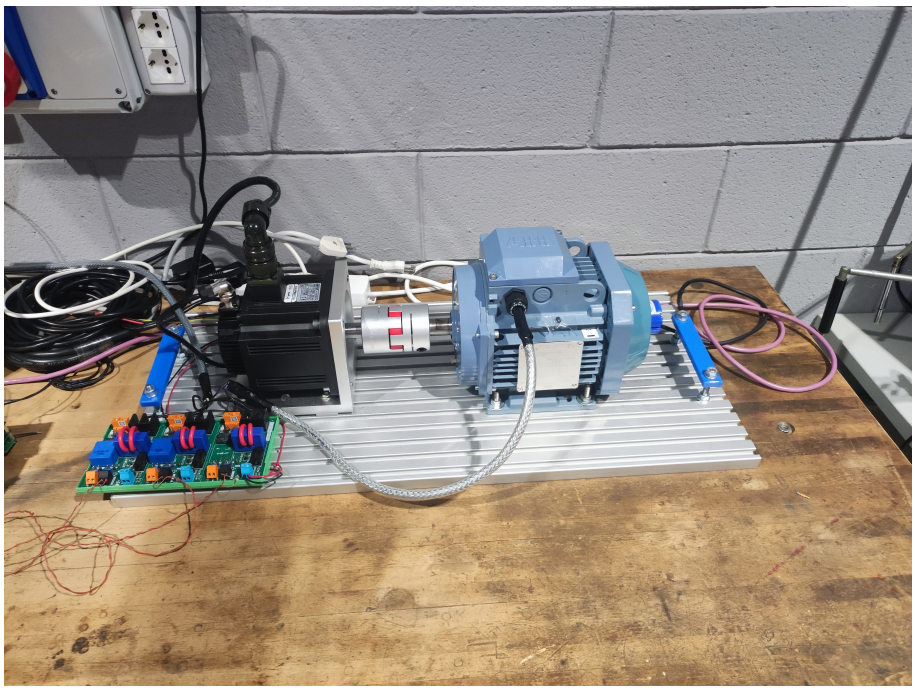


Figure 62: view of the test bench

The SynRM under test is operated as a brake, while a brushless machine acts as the prime mover and is regulated in speed. The brushless drive therefore imposes the mechanical operating point of the bench, and the SynRM develop the braking torque that loads the prime mover.

6.1 Test setup

The experimental test bench consists of two mechanically coupled motors: the SynRM under test (Table 4) and a PMSM motor acting as prime mover (Table 5).

The prime mover, an Estun EMG-10AFB22, is driven by an Estun ProNet servo drive operating in speed control mode, and therefore imposes the shaft speed of the bench. The SynRM is supplied by a custom two-level voltage source inverter controlled by the uCube control platform [41]. On the SynRM side only the current loop is closed: the d and q axis current references i_d^*, i_q^* are imposed directly from a Matlab script following the shape of the in Fig. 63, so that the machine operates as a brake against the speed-controlled prime mover.

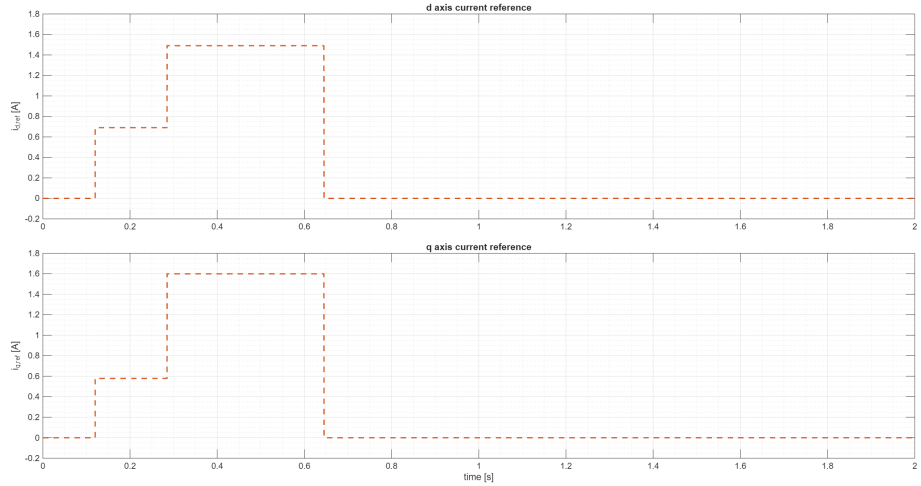


Figure 63: reference used in the experimental phase

The DC link of the inverter is supplied by an ITECH IT7900P regenerative grid simulator. operated as a DC source and set to $V_{dc} = 280$ V [64].



Figure 64: Regenerative Power supply unit

The uCube, developed at the power electronics laboratory of the University of Nottingham. The uCube is based on the off-the-shelf Microzed board from Avnet, a low-cost development board based on the Xilinx Zynq-7000 All Programmable SoC. The Zynq is a single device with dual-core ARM Cortex-A9 based Processing System (PS) and a Field Programmable Gate Array (FPGA) Programmable Logic (PL) [41]. The control algorithm runs as C code on one core, while the second core handles the communication with a host PC, where a MATLAB interface is used to set references and parameters and to download the acquired data. The FPGA handles the PWM modulators, with configurable switching frequency and dead time, the interfaces to the expansion boards, and a hardware trip that disables the PWM outputs within less than 1 μs when a measured quantity exceeds its threshold [41].

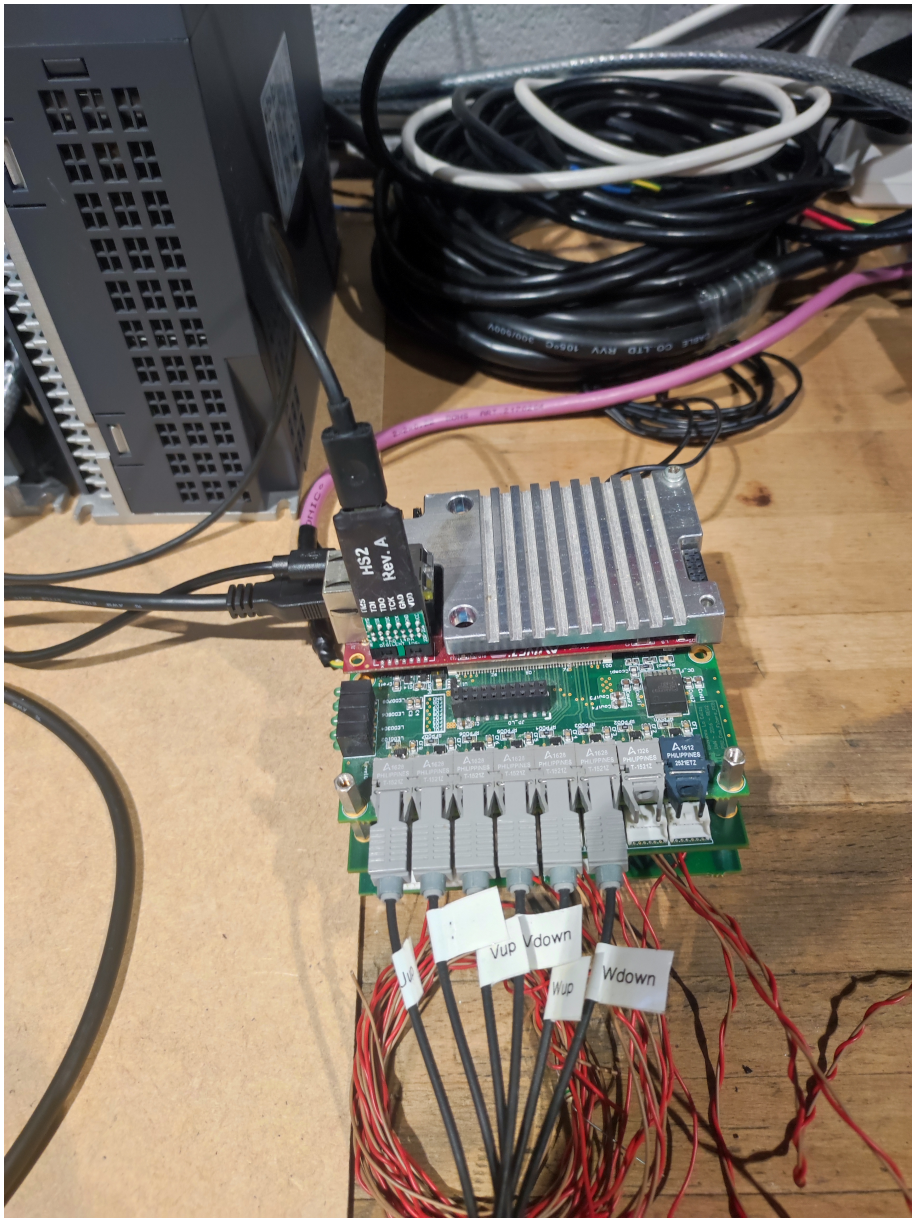


Figure 65: uCube control board

The currents of the SynRM are measured by a dedicated sensor board and acquired by the uCube. The rotor position is measured by a Tamagawa TS5700N8501 absolute encoder, with a resolution of 17 bit per revolution (131 072 counts/rev).

6.2 SynRM characteristics

Table 4: Rated data of the SynRM under test (ABB M3AL 90 LA 4) [42].

Quantity	Symbol	Value
Performance at nominal speed (400 V network)		
Rated output power	P_N	1.1 kW
Rated speed	n_N	1500 r/min
Electrical frequency	f_{el}	50 Hz
Number of pole pairs	p	2
Rated current	I_N	3.0 A
Rated torque	T_N	7.0 N m
Overload torque ratio	T_{OL}/T_N	1.5
Efficiency (full load)	η	81.4 %
Performance at maximum speed		
Output power	P	1.1 kW
Maximum speed	n_{max}	1800 r/min
Torque	T_2	5.8 N m
Overload torque ratio	T_{OL}/T_2	1.2
Mechanical data		
Rotor inertia	J	0.00202 kg m^2
Weight	m	13 kg
Frame size / mounting	–	90 / IM B3 (foot)
Protection / cooling	–	IP55 / IC 411
Insulation / temp. rise	–	Class F / Class F
Suggested drive	–	ACS850-04-03A0-5

6.3 PMSM characteristics

Table 5: Rated data of the prime mover (Estun EMG-10AFB22 PMSM servo motor) [43].

Quantity	Symbol	Value
Electrical and mechanical ratings		
Supply voltage	V_N	200 V AC
Rated output power	P_N	1.0 kW
Rated torque	T_N	4.78 N m
Instantaneous peak torque	T_{pk}	14.3 N m
Rated current	I_N	5.8 A_{rms}
Instantaneous max. current	I_{max}	17.4 A_{rms}
Rated speed	n_N	2000 r/min
Maximum speed	n_{max}	3000 r/min
Torque constant	k_T	0.82 Nm/A_{rms}
Rotor inertia	J	13.2×10^{-4} kg m^2
Feedback and construction		
Encoder	–	20-bit incremental (2^{20} counts/rev)
Insulation class	–	F
Enclosure / cooling	–	IP65 / totally enclosed, self-cooled
Shaft end	–	Straight, key and screw thread
Options	–	None (no brake, no oil seal)
Flange size	–	130 mm

6.4 PI control test result

The figure 66 shows the operating points required during the PI control test on the i_d/i_q plane. It also displays the current limit circle and the MTPA trajectories calculated from the apparent (green) and incremental (purple) inductance matrices. The two current reference steps drive the machine to the points (0.69 A, 0.58 A) and (1.49 A, 1.60 A). Both points lie on the MTPA curve, well within the current limit, in the

low-current region where the two MTPA trajectories nearly coincide. On the test bench the PI gains are again computed from (131) with $\zeta = 0.707$, but the natural frequencies are reduced to $f_{i,d} = 155$ Hz on the d axis and $f_{i,q} = 315$ Hz on the q axis. The 1 kHz design adopted in simulation section 5.1 proved too aggressive on the real drive: in the saturated region the incremental inductances are smaller than the apparent ones used in the design, so the actual loop is faster and less damped than expected, and the computation and modulation delay further reduces the phase margin.

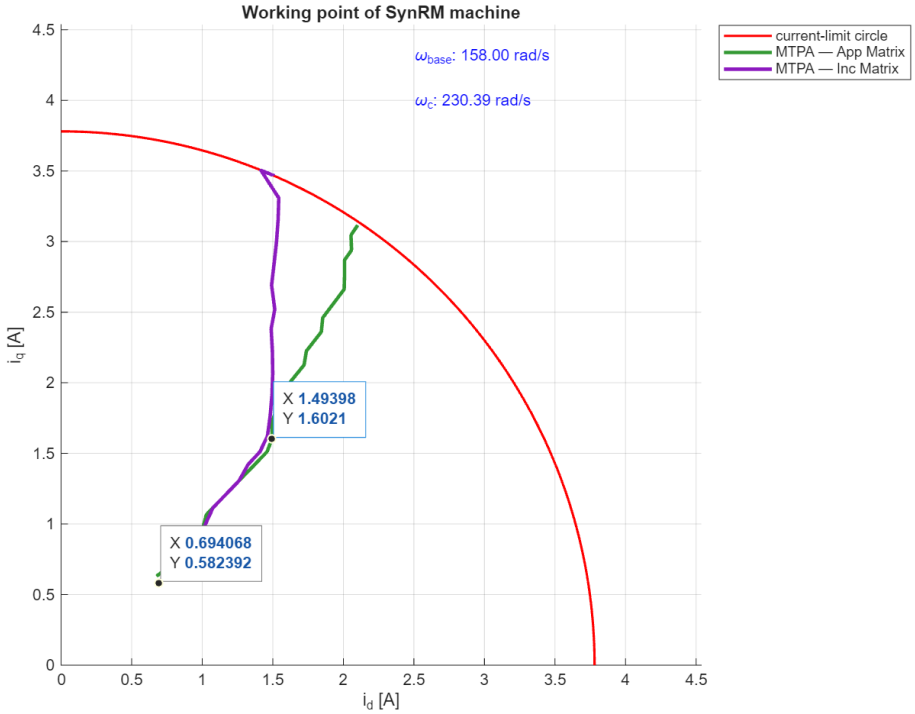


Figure 66: working point of the SynRM

During the test, the rotor speed is imposed by the PMSM motor and remains around 22 rad/s Fig. 67.

In the interval between 0.28 s and 0.65 s, when the higher current reference is applied, the speed oscillates between 15 and 30 rad/s.

The torque produced by the SynRM acts as a load disturbance on the drive motor's speed control loop, the tuning of this loop could be improved to effectively reject the disturbance, thereby maintaining a stable speed. The SynRM's torque ripple contributes to accentuating this phenomenon.

When the currents return to zero, the disturbance disappears, leaving only a slight periodic ripple.

The electrical angle exhibits a smooth sawtooth pattern between 0 and 2π with a constant slope, confirming the accuracy of the rotor position measurement throughout the test.

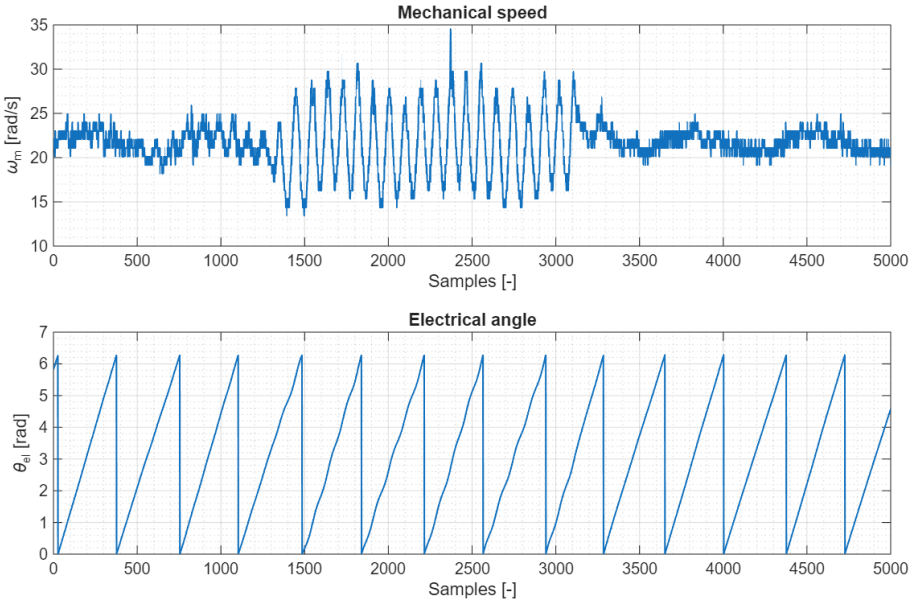


Figure 67: Electrical angle and mechanical speed of the SynRM

The measured d-axis current 68,follows the reference steps of 0.69 A and 1.49 A with a fast response. There is a small overshoot at the first step and a slight undershoot when the reference returns to zero at 0.65 s. In steady state the current shows a periodic ripple of a few tens of mA around the reference, with no appreciable steady-state error, as expected from the integral action of the PI regulator.

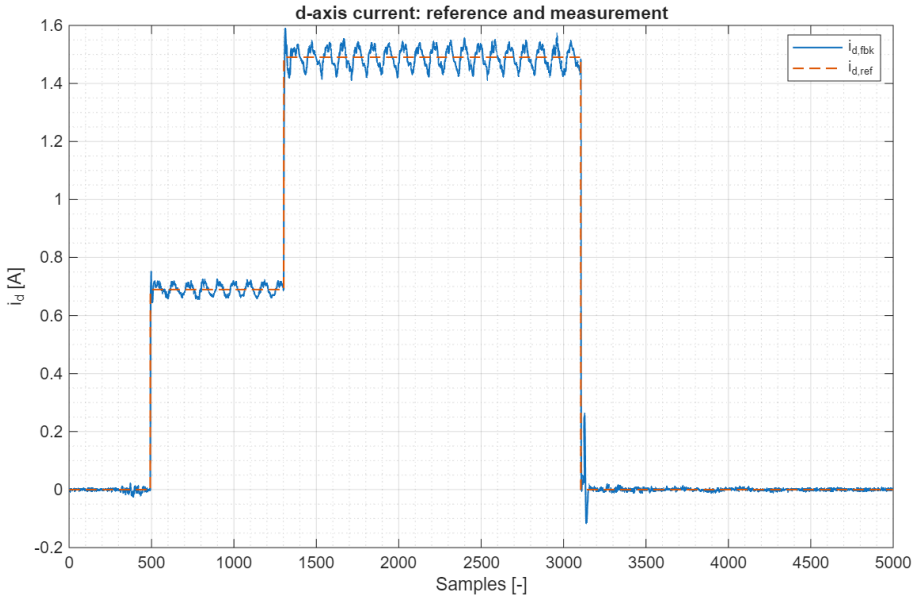


Figure 68: Tracking of the current reference on d axis

d-axis step from 0.69 A to 1.49 A. The measured current reaches the reference within about ten samples and peaks at 1.59 A, corresponding to a 12.4 % overshoot of the step amplitude. The subsequent undershoot brings the current down to 1.42 A, at the lower edge of the 5 % settling band, before the response settles 41 samples around 2.05 ms after the commutation 69.

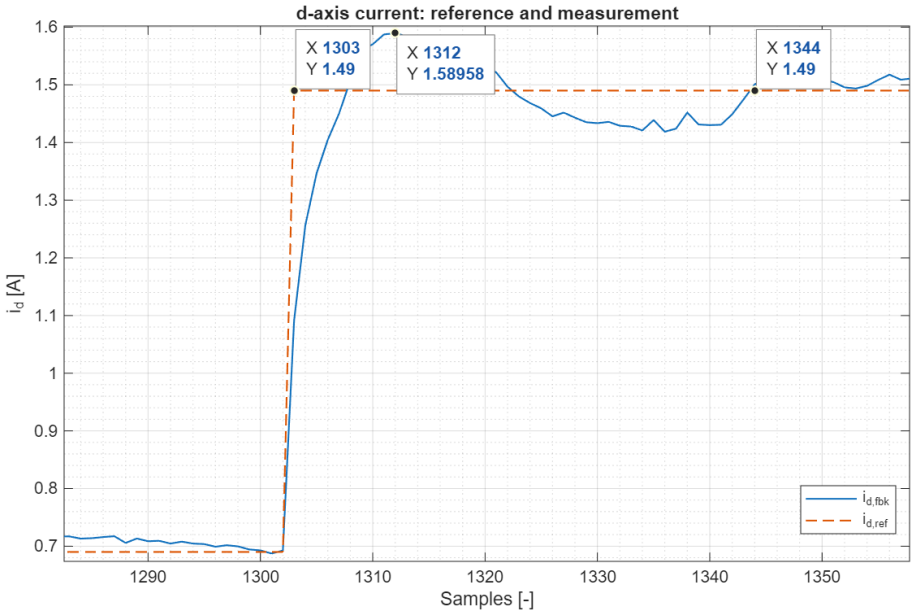


Figure 69: Tracking of the current reference on d axis zoom

The q-axis current 70 tracks the 0.58 A and 1.6 A references with a dynamic response similar to the d axis.

The ripple is slightly larger here, with periodic spikes up to about 1.7 A that can be linked to the rotor anisotropy and the resulting torque ripple.

After the references are removed, the current settles to zero with only small residual noise.

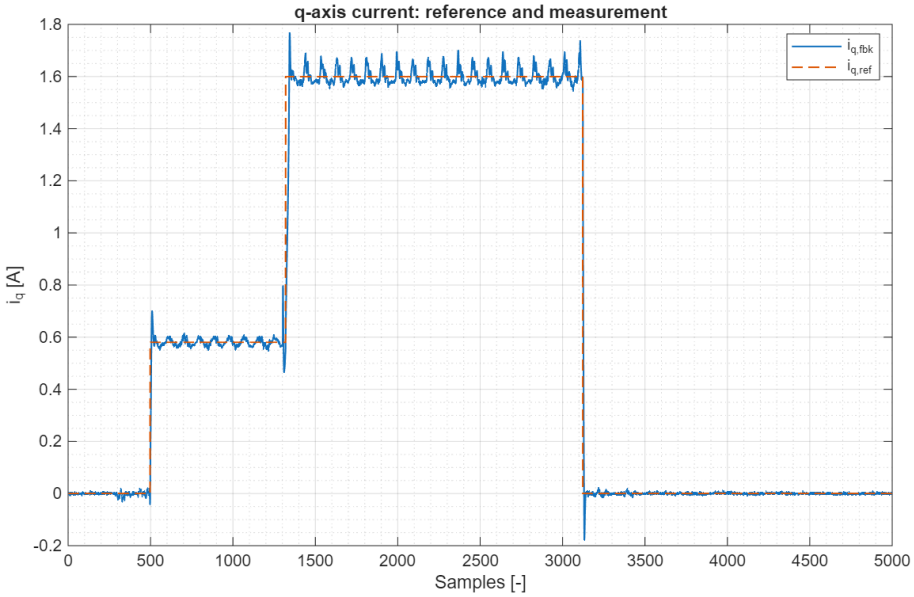


Figure 70: Tracking of the current reference on q axis

q-axis step from 0.58 A to 1.60 A. The rise is markedly slower than on the *d* axis

despite the wider design bandwidth, taking about 24 samples to reach the peak value of 1.77 A (16.5 % overshoot). The disturbance visible before the step, with the current dipping to 0.46 A, is caused by the preceding transition on the d-axis reference and illustrates the residual cross-coupling between the two axes 71.

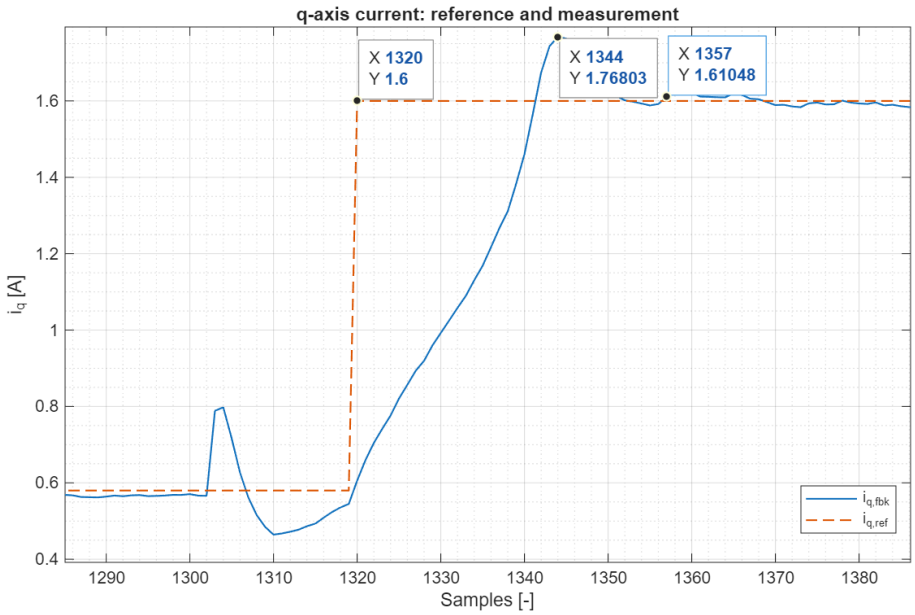


Figure 71: Tracking of the current reference on q axis zoom

The dynamic tracking performance of the PI current control is summarised in Table 6. The figures refer to the reference steps of Figure 63, acquired at 200 rpm with a sampling frequency of 20 kHz; overshoot is referred to the step amplitude and the settling time to a 5 % band around the final value.

Table 6: PI current control: measured step response of the d and q current loops.

Quantity	d axis	q axis
Initial current [A]	0.69	0.58
Final reference [A]	1.49	1.60
Step amplitude [A]	0.80	1.02
Peak value [A]	1.59	1.77
Overshoot [%]	12.4	16.5
Rise time (10–90%) [ms]	0.20	0.90
Settling time (5% band) [ms]	2.05	1.85

The phase currents 72 are balanced and sinusoidal, with a 120° phase shift. Their amplitude is approximately 0.9 A during the first stage and approximately 2.2 A during the second stage.

These values correspond to the magnitude of the current vectors in the dq reference frame, confirming the consistency between the Park transformation and the current measurement chain.

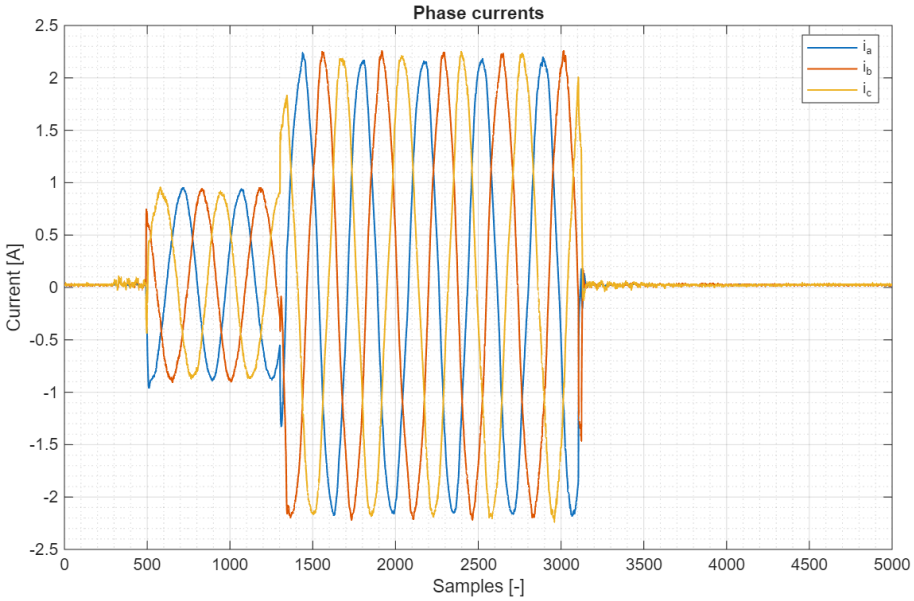


Figure 72: Measured three phase currents

6.5 INDI control test result

The results reported in this section were obtained with the INDI controller running on the same control board and power stage and same references used for the PI tests. The desired dynamics were set to $\omega_{c,d} = 2550$ rad/s (406 Hz) and $\omega_{c,q} = 5050$ rad/s (804 Hz), with an augmentation gain $K_{aug} = 1.0$ on the augmentation branch. The machine under test was operated as a brake while the prime mover held the shaft at 200 rpm the control and sampling frequency was 20 kHz, so that one sample on the horizontal axis corresponds to 50 μsecond.

Figure 73 shows the complete test sequence on the d axis. The reference is raised in two steps and then brought back to zero, so that the loop is exercised at two different levels of saturation of the machine. The measured current follows the reference at both levels with no steady-state error, confirming that the incremental law does not require an explicit integral action to reject the constant terms of the model.

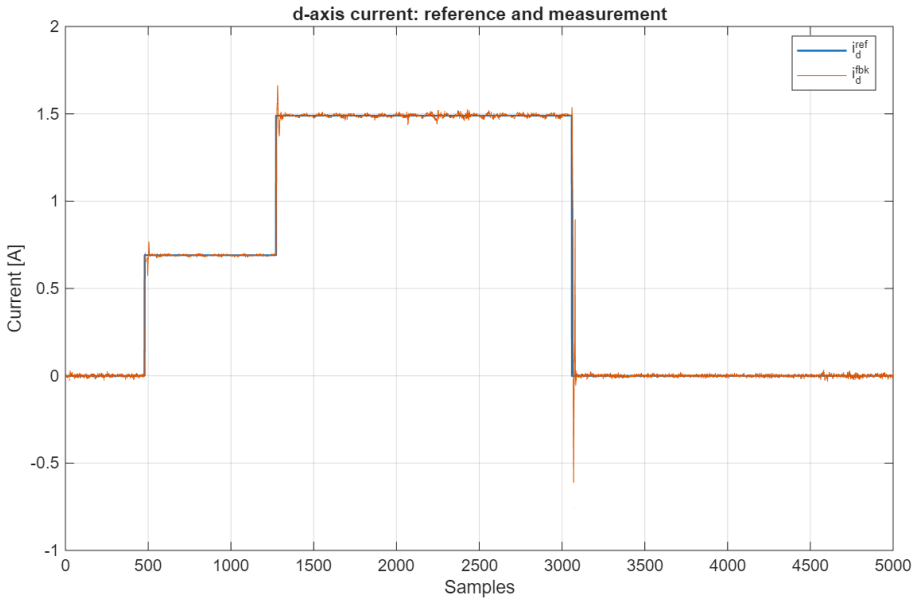


Figure 73: Tracking of the current reference on d axis

The zoomed view of Figure 74 resolves the transient on the second step, from 0.69 A to 1.49 A. The current leaves the initial level within two samples of the reference commutation and peaks at 1.66 A nine samples later, after which it recovers and enters the 5 % settling band. The undershoot that follows the peak brings the current down to

about 1.42 A, at the lower edge of the band, before the response settles.

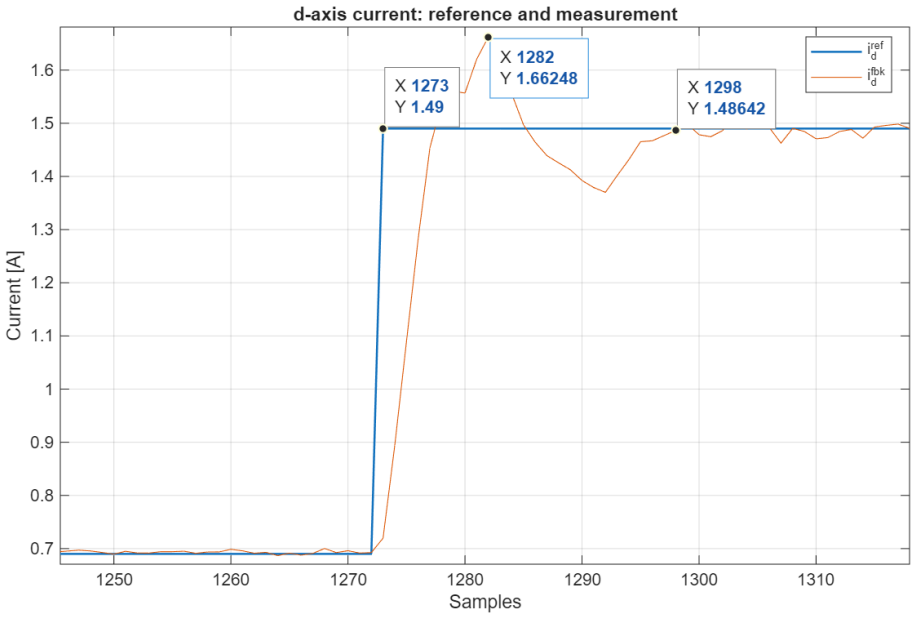


Figure 74: Tracking of the current reference on d axis zoom at the step

The q-axis response of Figure 75 follows the same sequence and shows the same qualitative behaviour. The ripple on this axis has comparable frequency and slightly larger amplitude than on the d axis, which is consistent with the lower inductance of the q axis: for a given voltage disturbance the resulting current deviation is larger where the inductance is smaller.

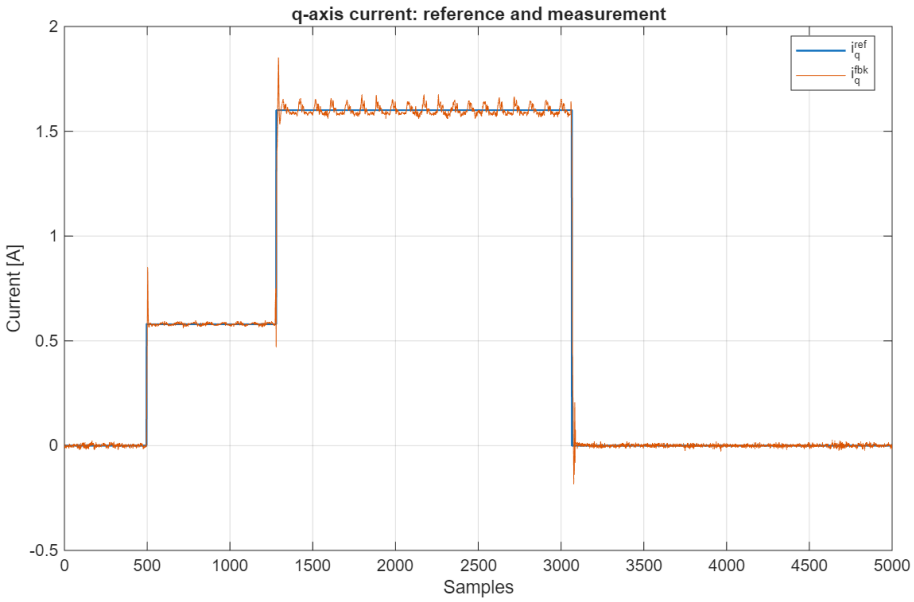


Figure 75: Tracking of the current reference on q axis

Figure 76 details the corresponding transient on the q axis, from 0.58 A to 1.60 A. The peak value of 1.85 A is reached thirteen samples after the commutation. It is worth noting that the rise is slower than on the d axis even though the q loop is tuned for a wider bandwidth and the machine presents a lower inductance on that axis; the same behaviour is observed with the PI controller.

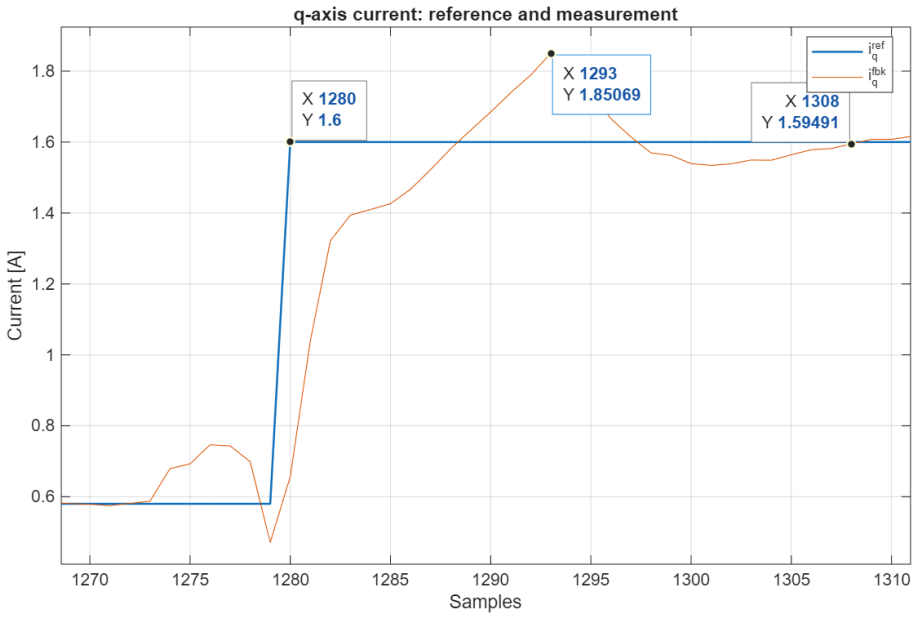


Figure 76: Tracking of the current reference on q axis zoom at the step

The figures extracted from the two transients are collected in Table 7. Overshoot is referred to the amplitude of the step, and the settling time to a 5 % band around the final value.

Table 7: INDI current control: measured step response of the d and q current loops.

Quantity	d axis	q axis
Initial current [A]	0.69	0.58
Final reference [A]	1.49	1.60
Step amplitude [A]	0.80	1.02
Peak value [A]	1.66	1.85
Overshoot [%]	21.6	24.6
Rise time (10–90%) [ms]	0.20	0.45
Settling time (5% band) [ms]	1.25	1.40

Since the inductance matrix acts as the control gain of the incremental law, with $\mathbf{B}^{-1} = \mathbf{L}$, it is essential to verify that the on-board model is effectively interpolating the identified maps rather than falling back on constant values. Figure 77 confirms that this is the case: the four inductances change at each transition of the current references and return to their unsaturated values once the references are removed. The d-axis term decreases from 0.62 H to 0.47 H between no load and the highest current level, whereas the q-axis term falls from 0.242 H to 0.082 H. This dependence of the gain on the operating point is precisely what a constant-parameter inversion cannot reproduce, and it is the reason why the maps are embedded in the on-board model.

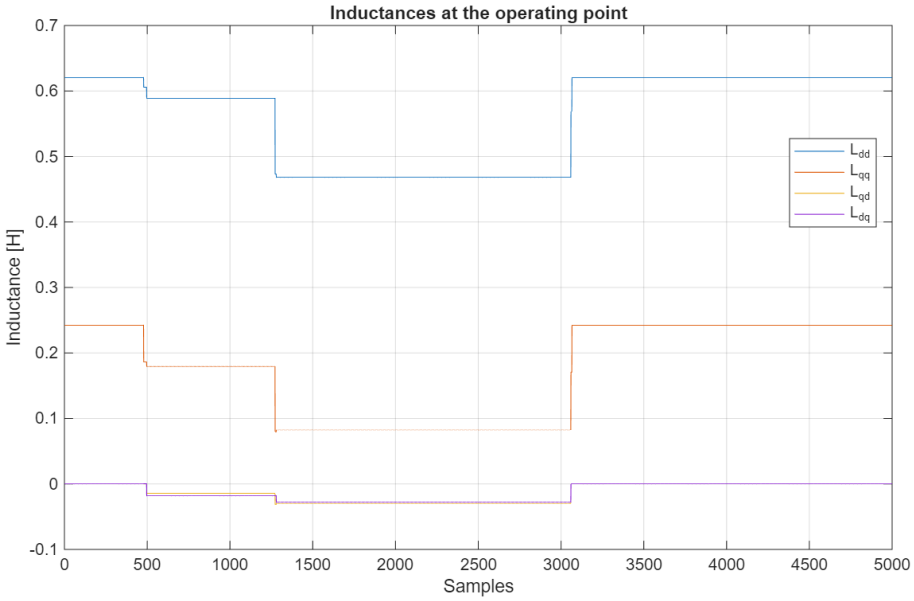


Figure 77: Inductances reconstructed by the on-board model

Figure 78 reports the same test observed in the stationary frame. The three phase currents remain balanced throughout the sequence and their envelope reproduces the two levels imposed on the *dq* references, which provides an independent check on the consistency of the transformations and on the correctness of the rotor position used by the control.

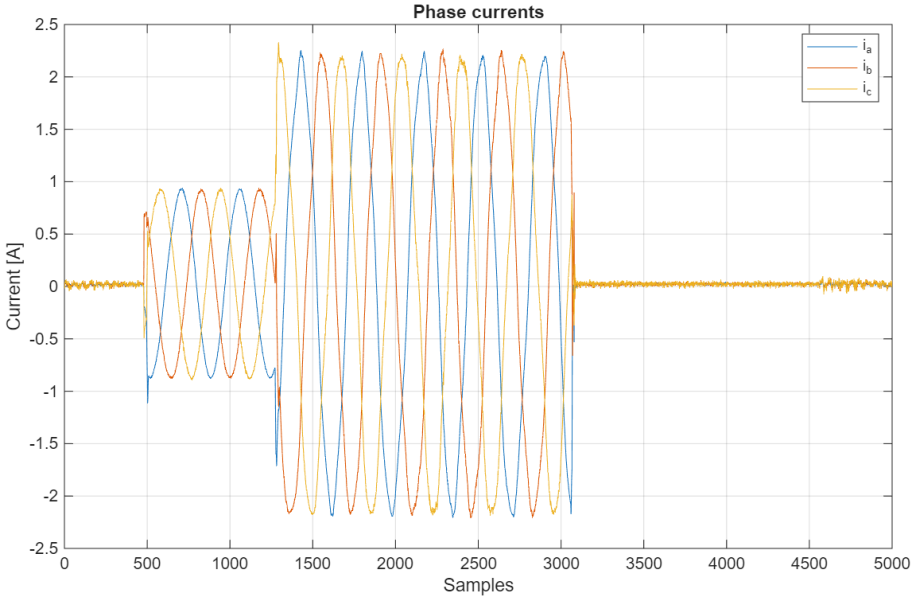


Figure 78: Measured three phase currents

7 Conclusions

The steady-state quality of the phase currents produced by the four current control strategies was assessed at maximum torque and rated speed. The evaluation window is $t \in [0.9, 1.0]$ s, which spans five periods of the electrical fundamental ($f_1 = 50$ Hz). The Total Harmonic Distortion was computed on phase a from the FFT of the signal, including harmonics up to the 40th order (2 kHz):

$$\mathrm{THD}_I = \frac{\sqrt{\Sigma_{n=2}^{40} I_n^2}}{I_1} \cdot 100\,\%. \tag{212}$$

The time-domain waveforms are shown in Fig. 79, their comparison with the theoretical sinusoid in Fig. 80, and the resulting THD values in Fig. 81 and Table 8.

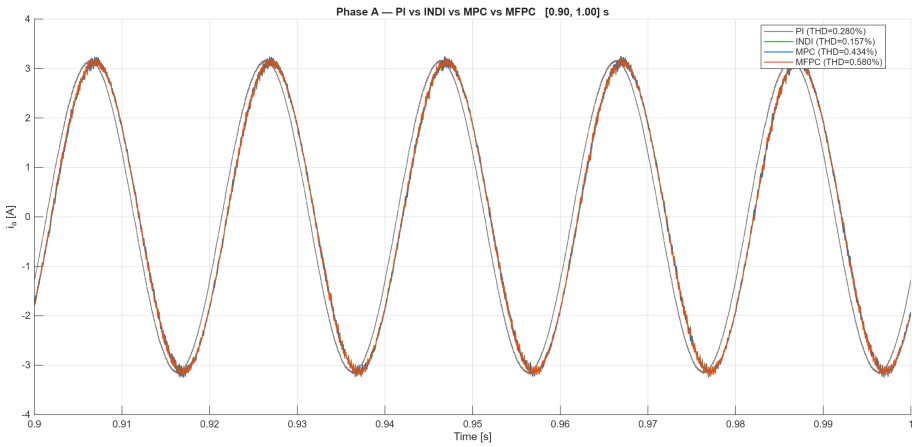


Figure 79: Phase-a current at maximum torque and rated speed, window $[0.9, 1.0]$ s: PI, INDI, MPC and MFPC. The INDI trace is largely superimposed on the MPC and MFPC traces.

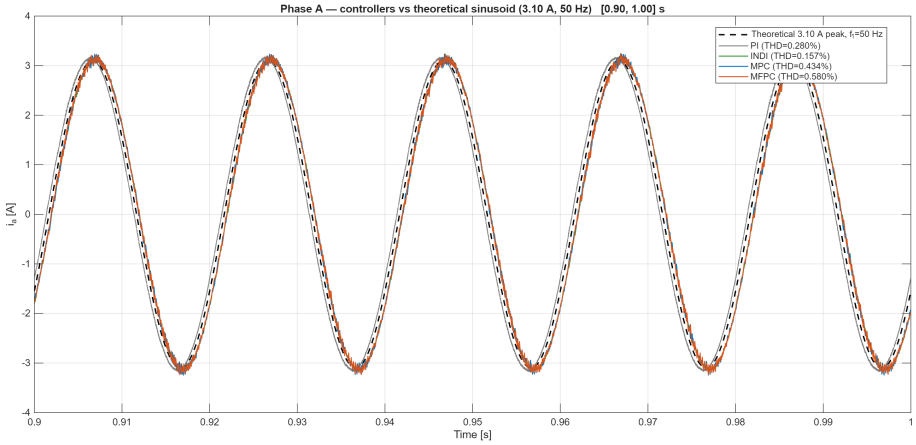


Figure 80: Phase-a current of the four controllers compared with the theoretical sinusoid (3.1 A peak, $f_1 = 50$ Hz), window $[0.9, 1.0]$ s. The phase of the theoretical sinusoid is aligned with the PI fundamental for visual reference.

Table 8: Phase-a current THD at maximum torque and rated speed, window $[0.9, 1.0]$ s, harmonics up to the 40th order.

Controller	THD [%]	Δ vs PI [%]	Modulation
PI	0.280	—	SVPWM, $f_{sw} = 20$ kHz
INDI	0.157	−43.9	SVPWM, $f_{sw} = 20$ kHz
MPC	0.434	+55.0	FCS, variable f_{sw}
MFPC	0.580	+107.1	FCS, variable f_{sw}

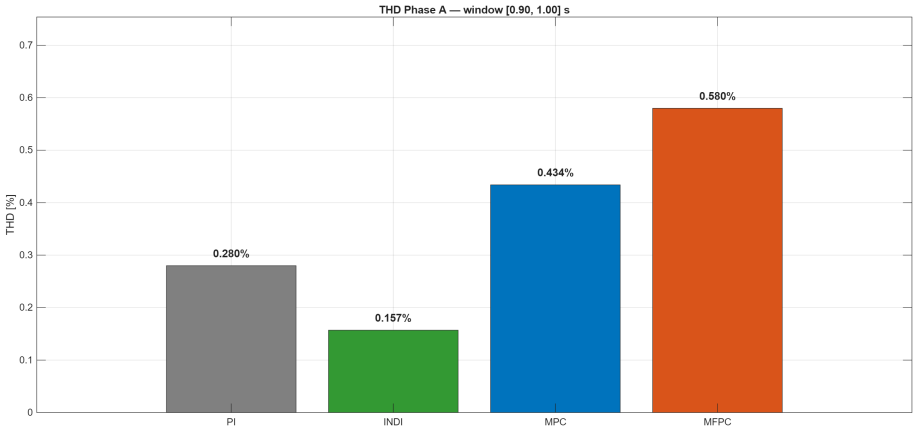


Figure 81: Phase-a current THD of the four controllers, window $[0.9, 1.0]$ s, harmonics up to the 40th order.

The first observation is that all four strategies deliver highly sinusoidal currents. The THD is well below 1 % in every case, and the fundamental amplitude matches the

expected peak value of 3.1 A. The differences discussed below therefore concern the degree of refinement of the current waveform, not its acceptability for the drive.

INDI achieves the lowest distortion of the whole comparison (0.157 %), a reduction of about 44 % with respect to the PI controller (0.280 %). This result is consistent with the structure of the two controllers. The PI relies on a feedforward decoupling network to compensate the coupling between the d and q axes. INDI instead inverts the incremental dynamics at every sampling step using the full inductance matrix supplied by the on-board model. Residual coupling and the saturation-dependent variation of the inductances are therefore compensated directly, rather than being left to the integral action. In addition, the first-order closed-loop dynamics of INDI allow a wider current bandwidth than the PI (up to 4 kHz on the d axis versus 1 kHz). Low-order disturbances are thus rejected more effectively.

Both predictive controllers show a higher THD than the modulated ones: 0.434 % for MPC and 0.580 % for MFPC. This is mainly a structural consequence of the finite-control-set approach. Without a modulator, a single voltage vector is applied over each sampling period, and the switching frequency is variable (about 5.4 kHz on average at $f_s = 20$ kHz). The resulting spectrum is spread over a wide frequency range, including the low-frequency band covered by the THD. With SVPWM, by contrast, the switching harmonics of PI and INDI are concentrated around multiples of 20 kHz, well outside that band. For the same reason, the high-frequency ripple visible on the MPC and MFPC waveforms in Fig. 79 is only partially captured by a THD limited to the 40th harmonic. The THD therefore tends to understate, rather than overstate, the difference in ripple between the two families.

MFPC shows a THD about 34 % higher than the model-based MPC. This result must be read in the light of the conditions of the test. In simulation, the model-based predictor uses the same machine parameters as the plant, so it operates under nominally matched conditions. This is the most favourable scenario for a model-based predictor: its prediction error is limited to the discretisation and to the unmodelled effects.

MFPC does not use the physical model. It replaces it with the ultra-local model, whose lumped term $\hat{F}$ is estimated online by RLS from measured current increments. This estimate inevitably contains measurement-driven fluctuations, which persist to some

extent even after the 1 kHz low-pass filter. They translate into a prediction error and, occasionally, into the selection of a sub-optimal voltage vector, which appears as additional ripple. The higher THD is thus the cost of discarding the model in a situation where the model is exact. It does not contradict the literature, where the advantage of model-free predictive control is established chiefly in terms of robustness to parameter mismatch and on experimental set-ups in which the real plant deviates from its nominal description.

Fig. 80 shows that the INDI, MPC and MFPC currents are practically superimposed, while the PI current exhibits a small, constant phase displacement with respect to them. Since the absolute phase of i_a in each simulation also depends on the electrical rotor angle and on the (i_d, i_q) operating point reached by each controller, this displacement should be interpreted with care. The tracking error in the dq frame remains the most reliable indicator of the dynamic performance of the current loops.

In terms of steady-state current quality at the rated operating point, the four strategies rank as INDI, PI, MPC and MFPC, with all THD values below 0.6 %. INDI combines the lowest distortion with the widest bandwidth, which makes it the most attractive option among the modulated controllers. The predictive controllers pay for their fast, modulator-free dynamics with a broader current spectrum. Between the two predictive controllers, the model-based one is favoured by the ideal knowledge of the machine parameters available in simulation. A robustness analysis with deliberately mismatched controller parameters, together with the experimental validation on the test bench, is required to assess whether the model-free approach recovers its expected advantage under realistic operating conditions.

The simulation results are complemented by an experimental comparison between the PI and INDI controllers on the test bench. Fig. 82 shows the phase-c current of the two controllers over an analysis window of 0.704 s, which spans five electrical periods, and Fig. 83 the corresponding THD.

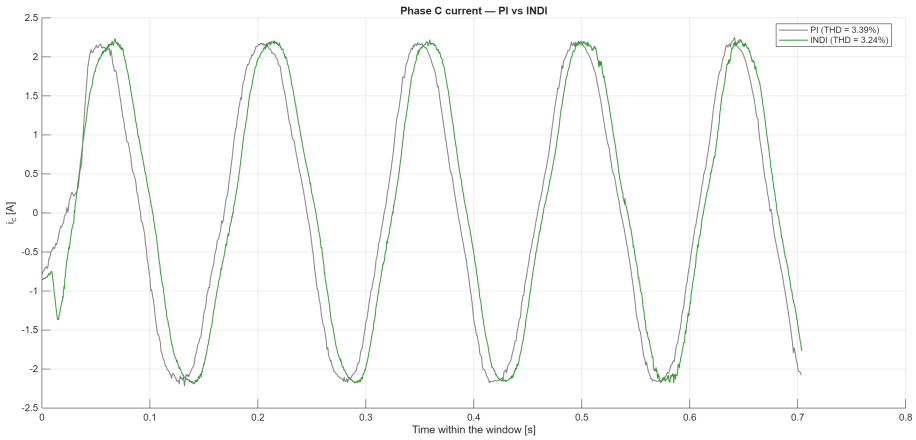


Figure 82: Experimental phase-*c* current of the PI and INDI controllers.

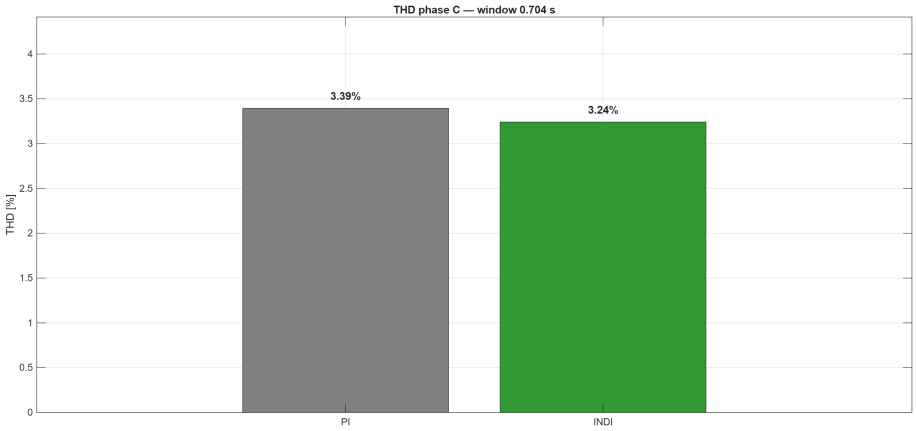


Figure 83: Experimental phase-*c* current THD of the PI and INDI controllers

In steady state the two controllers are practically indistinguishable. The currents have the same amplitude (about 2.2 A peak) and the measured THD is 3.39 % for the PI and 3.24 % for INDI. The difference of 0.15 percentage points (about 4 %) is small and, on a single acquisition, cannot be regarded as significant. This differs from the simulation, where INDI reduced the THD by about 44 % with respect to the PI. Two aspects must be considered. First, the experimental THD is more than one order of magnitude higher than the simulated one for both controllers. This suggests that it is set by effects that neither controller compensates and that are likely absent or reduced in simulation, such as current measurement noise and quantisation, and inverter dead time and nonlinearity, not considered in the simulations. Second, the operating point of the test bench differs from the rated one used in simulation (about 2.2 A peak and a fundamental frequency of roughly 7 Hz, against 3.1 A and 50 Hz), so the absolute THD values of the two sets of

results are not directly comparable. As in simulation, the constant displacement between the two traces in Fig. 82 depends on the rotor position at the instant of acquisition and should not be read as a difference in tracking performance.

The difference between the two controllers emerges instead in the dynamic response.

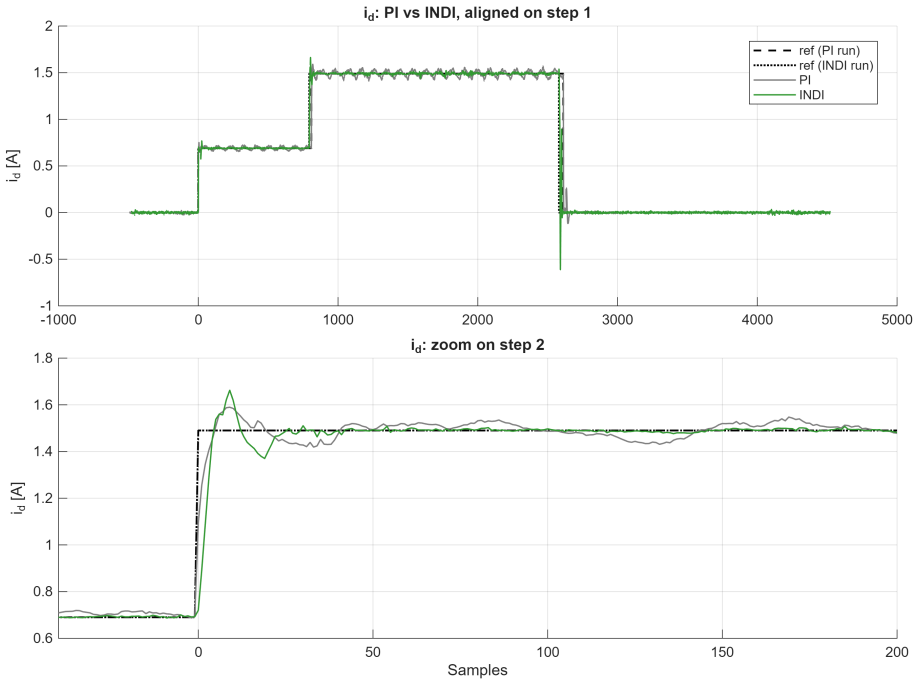


Figure 84: Experimental *d*-axis current of the PI and INDI controllers with their references. Each acquisition is aligned on its own reference step.

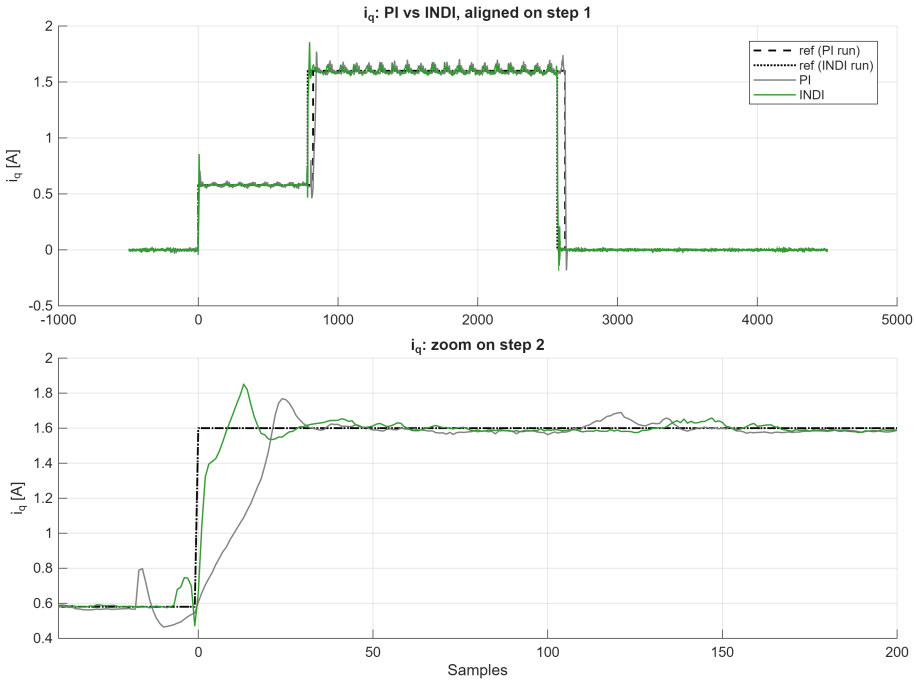


Figure 85: Experimental q-axis current of the PI and INDI controllers with their references. Each acquisition is aligned on its own reference step.

In the step response of Fig. 84 and 85, INDI reaches the reference faster than the PI. This is consistent with the design of the two loops: the closed-loop bandwidth of INDI is considerably wider up to 406 Hz on the d axis against 155 Hz for the PI, and 804 Hz on q axis against 315 Hz for PI, so the current follows a variation of the reference more rapidly. The advantage in bandwidth, which is masked in the steady-state THD by the non-idealities discussed above, is therefore clearly visible during transients.

References

[1] European Commission, Directorate-General for Internal Market, Industry, Entrepreneurship and SMEs, "Study on the Critical Raw Materials for the EU 2023 – Final Report," Publications Office of the European Union, Luxembourg, Technical Report, 2023, eT0723116ENN.

[2] M. Murataliyev, M. Degano, M. Di Nardo, N. Bianchi, and C. Gerada, "Synchronous reluctance machines: A comprehensive review and technology comparison," *Proceedings of the IEEE*, vol. 110, no. 3, pp. 382–399, Mar. 2022, manoscritto accettato disponibile ad accesso aperto. [Online]. Available: https://nottingham-repository.worktribe.com/output/7477537

[3] B. K. Bose, *Modern Power Electronics and AC Drives*. Upper Saddle River, NJ: Prentice Hall, 2002.

[4] P. C. Krause, O. Wasynczuk, S. D. Sudhoff, and S. D. Pekarek, *Analysis of Electric Machinery and Drive Systems*, 3rd ed. Hoboken, NJ: Wiley-IEEE Press, 2013.

[5] R. Krishnan, *Permanent Magnet Synchronous and Brushless DC Motor Drives*. Boca Raton, FL: CRC Press, 2010.

[6] J. R. Hendershot and T. J. E. Miller, *Design of Brushless Permanent-Magnet Machines*, 2nd ed. Venice, FL: Motor Design Books, 2010.

[7] P. Pillay and R. Krishnan, "Modeling, simulation, and analysis of permanent-magnet motor drives, part I: The permanent-magnet synchronous motor drive," *IEEE Transactions on Industry Applications*, vol. 25, no. 2, pp. 265–273, 1989.

[8] J. Pyrhönen, T. Jokinen, and V. Hrabovcová, *Design of Rotating Electrical Machines*, 2nd ed. Chichester, UK: Wiley, 2014.

[9] T. M. Jahns, G. B. Kliman, and T. W. Neumann, "Interior permanent-magnet synchronous motors for adjustable-speed drives," *IEEE Transactions on Industry Applications*, vol. IA-22, no. 4, pp. 738–747, 1986.

[10] S. Morimoto, Y. Takeda, T. Hirasa, and K. Taniguchi, “Expansion of operating limits for permanent magnet motor by current vector control considering inverter capacity,” *IEEE Transactions on Industry Applications*, vol. 26, no. 5, pp. 866–871, 1990.

[11] W. Leonhard, *Control of Electrical Drives*, 2nd ed. Berlin, Heidelberg: Springer, 1996.

[12] S. D. Umans, *Fitzgerald & Kingsley’s Electric Machinery*, 7th ed. New York: McGraw-Hill, 2014.

[13] R. H. Park, “Two-reaction theory of synchronous machines: Generalized method of analysis – part I,” *Transactions of the American Institute of Electrical Engineers*, vol. 48, no. 3, pp. 716–727, 1929.

[14] D. W. Novotny and T. A. Lipo, *Vector Control and Dynamics of AC Drives*. Oxford, UK: Oxford University Press, 1996.

[15] I. Boldea, *Reluctance Synchronous Machines and Drives*. Oxford, UK: Clarendon Press, 1996.

[16] A. Vagati, “The synchronous reluctance solution: A new alternative in AC drives,” in *Proceedings of IECON’94 – 20th Annual Conference of the IEEE Industrial Electronics Society*, vol. 1, 1994, pp. 1–13.

[17] R. E. Betz, R. Lagerquist, M. Jovanović, T. J. E. Miller, and R. H. Middleton, “Control of synchronous reluctance machines,” *IEEE Transactions on Industry Applications*, vol. 29, no. 6, pp. 1110–1122, 1993.

[18] F. Gemma, J. Riccio, A. Volpini, G. Tresca, and P. Zanchetta, “Model-free-predictive control of open-end winding synchronous reluctance motor drive,” in *Model-Free-Predictive Control of Open-End Winding Synchronous Reluctance Motor Drive*. IEEE, 2025.

[19] A. Vagati, M. Pastorelli, F. Scapino, and G. Franceschini, “Impact of cross saturation in synchronous reluctance motors of the transverse-laminated type,” *IEEE Transactions on Industry Applications*, vol. 36, no. 4, pp. 1039–1046, 2000.

[20] E. Armando, R. I. Bojoi, P. Guglielmi, G. Pellegrino, and M. Pastorelli, "Experimental identification of the magnetic model of synchronous machines," *IEEE Transactions on Industry Applications*, vol. 49, no. 5, pp. 2116–2125, 2013.

[21] Z. Qu, T. Tuovinen, and M. Hinkkanen, "Inclusion of magnetic saturation in dynamic models of synchronous reluctance motors," in *Proceedings of the International Conference on Electrical Machines (ICEM)*, Marseille, France, 2012, pp. 994–1000.

[22] L. Xu, X. Xu, T. A. Lipo, and D. W. Novotny, "Vector control of a synchronous reluctance motor including saturation and iron loss," *IEEE Transactions on Industry Applications*, vol. 27, no. 5, pp. 977–985, 1991.

[23] J. J. Grainger and W. D. Stevenson, *Power System Analysis*. New York: McGraw-Hill, 1994.

[24] C. Melchiorri, *Traiettorie per azionamenti elettrici*. Bologna: Società Editrice Esculapio, 2000, in Italian.

[25] B. Wu and M. Narimani, *High-Power Converters and AC Drives*, 2nd ed. Hoboken, NJ, USA: Wiley-IEEE Press, 2017.

[26] J. Holtz and S. Stadtfeld, "A predictive controller for the stator current vector of AC machines fed from a switched voltage source," in *Proc. International Power Electronics Conference (IPEC)*, Tokyo, Japan, 1983, pp. 1665–1675.

[27] G. C. Goodwin, M. M. Seron, and J. A. De Doná, *Constrained Control and Estimation: An Optimisation Perspective*, ser. Communications and Control Engineering. London: Springer-Verlag, 2005.

[28] J. Rodriguez and P. Cortes, *Predictive Control of Power Converters and Electrical Drives*, ser. Wiley-IEEE Press. Chichester, UK: John Wiley & Sons, 2012.

[29] M. Khalilzadeh, S. Vaez-Zadeh, J. Rodriguez, and R. Heydari, "Model-free predictive control of motor drives and power converters: A review," *IEEE Access*, vol. 9, pp. 105 733–105 747, 2021.

[30] F. Gemma, J.-B. Jacquier, G. Tresca, J. Rodríguez, and P. Zanchetta, "Model-free predictive controllers for voltage source inverter: A unified experimental benchmarking," *IEEE Open Journal of the Industrial Electronics Society*, 2026, in press.

[31] J. Sherman and W. J. Morrison, "Adjustment of an inverse matrix corresponding to a change in one element of a given matrix," *The Annals of Mathematical Statistics*, vol. 21, no. 1, pp. 124–127, 1950.

[32] D. Canin, "F-35 high angle of attack flight control development and flight test results," in *AIAA Aviation Forum*, 2019, aIAA-2019-3227.

[33] S. Nazar and Z. Rekasius, "Decoupling of a class of nonlinear systems," *IEEE Transactions on Automatic Control*, vol. 16, no. 3, pp. 257–260, 1971.

[34] A. Isidori, *Nonlinear Control Systems*, ser. Communications and Control Engineering. Berlin: Springer, 1995.

[35] K. J. Åström and T. Hägglund, *Advanced PID Control*. Research Triangle Park, NC, USA: ISA – The Instrumentation, Systems, and Automation Society, 2006.

[36] A. R. Munoz and T. A. Lipo, "On-line dead-time compensation technique for open-loop PWM-VSI drives," *IEEE Transactions on Power Electronics*, vol. 14, no. 4, pp. 683–689, 1999.

[37] L. Wang and L. Gan, "Integral FCS predictive current control of induction motor drive," in *IFAC Proceedings Volumes (19th IFAC World Congress)*, vol. 47, no. 3, 2014, pp. 11 956–11 961.

[38] J. Riccio, P. Karamanakos, S. Odhano, M. Tang, M. Di Nardo, and P. Zanchetta, "Direct model predictive control of synchronous reluctance motor drives," *IEEE Transactions on Industry Applications*, vol. 59, no. 1, pp. 1054–1063, 2023.

[39] K. J. Åström and L. Rundqwist, "Integrator windup and how to avoid it," in *Proceedings of the American Control Conference*, 1989, pp. 1693–1698.

[40] A. Steinert, S. Raab, S. Hafner, F. Holzapfel, and H. Hong, “From fundamentals to applications of incremental nonlinear dynamic inversion: A survey on INDI – part I,” *Chinese Journal of Aeronautics*, vol. 38, no. 11, p. 103553, 2025.

[41] A. Galassini, G. Lo Calzo, A. Formentini, C. Gerada, P. Zanchetta, and A. Costabeber, “uCube: Control platform for power electronics,” in *2017 IEEE Workshop on Electrical Machines Design, Control and Diagnosis (WEMDCD)*, Nottingham, UK, 2017, pp. 216–221.

[42] ABB, “High output synchronous reluctance (HO SynRM) aluminum motor range, 90–132: Optimized cost of ownership for pump and fan applications,” Product note, document 9AKK106001 EN, Rev. A, Jun. 2013, preliminary efficiency data.

[43] Estun Automation Co., Ltd., “ProNet ED3M all digital AC servo systems – product catalogue,” Nanjing, P.R. China, includes EMJ/EML/EMG servo motor specifications.

Acknowledgments

I would like to express my gratitude to Professor Zanchetta, my supervisor Filippo Gemma, and the PELab for giving me the opportunity to work in this group and making me feel truly a part of it. Someone once said that you never stop learning and growing, and my experience at PELab, together with the work I have done over the past few years with fellow students, is proof of that. Despite my age, being open to listening allowed me to meet fantastic people and learn a lot from them, and for that I will be eternally grateful. Among all my fellow students, a special thank you goes to Orgen, Yassine, Francesco, Simone, and Mahdi, who supported me the most during the difficult times, or at least witnessed some sign of them.I also want to extend heartfelt thanks to my lifelong friends, who have been with me through every stage of my growth, whether professional, academic, or personal. A special thank you goes to Marco, Daniele, and Francesca. I will always remember the times I was absent because of my studies. Yet, despite everything, there was always a message or a call asking whether I would be joining the next outing. Your constant presence has been truly incredible and a source of unwavering support. Speaking of unwavering support and presence, I want to express my loving gratitude to my partner, Michela. For a long time, she has truly been able to wait and set aside her own expectations in order to prioritize mine, even putting herself second to my studies. Although I often come across as rough or aloof, this effort has not gone unnoticed. I felt your support and love even when we were apart. Thank you for everything in the past, and I now hope to repay you for the sacrifices you have made, to the best of my ability. To conclude, I would like to thank my mother and father, who, like a constant shadow, have always supported and stood by my decisions. I sincerely hope I have repaid their infinite love, at least in small part, by giving them a few moments of parental pride, including this graduation. I have no words to thank them enough.

Stefano